

A Tutorial on Learning-Based Radio Map Construction: Data, Paradigms, and Physics-Awareness

Xiucheng Wang, Yuhao Pan, Nan Cheng

Abstract—The integration of artificial intelligence into next-generation wireless networks necessitates the accurate construction of radio maps (RMs) as a foundational prerequisite for electromagnetic digital twins. A RM provides the digital representation of the wireless propagation environment, mapping complex geographical and topological boundary conditions to critical spatial-spectral metrics that range from received signal strength to full channel state information matrices. This tutorial presents a comprehensive survey of learning-based RM construction, systematically addressing three intertwined dimensions: data, paradigms, and physics-awareness. From the data perspective, we review physical measurement campaigns, ray tracing simulation engines, and publicly available benchmark datasets, identifying their respective strengths and fundamental limitations. From the paradigm perspective, we establish a core taxonomy that categorizes RM construction into source-aware forward prediction and source-agnostic inverse reconstruction, and examine five principal neural architecture families spanning convolutional neural networks, vision transformers, graph neural networks, generative adversarial networks, and diffusion models. We further survey optics-inspired methods adapted from neural radiance fields and 3D Gaussian splatting for continuous wireless radiation field modeling. From the physics-awareness perspective, we introduce a three-level integration framework encompassing data-level feature engineering, loss-level partial differential equation regularization, and architecture-level structural isomorphism. Open challenges including foundation model development, physical hallucination detection, and amortized inference for real-time deployment are discussed to outline future research directions.

Index Terms—Radio map, neural network, physics-informed neural network, diffusion model, generative artificial intelligence.

I. INTRODUCTION

Next-generation wireless networks increasingly rely on artificial intelligence to manage complex, high-dimensional data distributions [1], [2]. These distributions include massive multiple-input multiple-output (MIMO) channel matrices, heterogeneous traffic patterns, and dynamic network topologies [3], [4]. To support the realization of electromagnetic digital twins, the accurate construction of radio maps (RMs) has become a fundamental prerequisite [5], [6]. An RM provides a digital

representation of the wireless propagation environment over a geographic region of interest. It maps geographical and topological boundary conditions to spatial-spectral metrics. These metrics range from received signal strength (RSS) and time of arrival (ToA) to full complex channel state information (CSI) matrices [7]. A high-fidelity RM therefore serves as the cornerstone for downstream tasks such as resource allocation, interference management, and predictive network planning [8], [9].

Traditionally, acquiring ground-truth radio environment data has relied on dedicated physical measurement campaigns [3]. Drive tests and walk tests capture the stochastic nature of real-world propagation channels [10]. However, these methods suffer from high operational costs and limited spatial coverage [11]. Indoor environments and three-dimensional vertical domains remain particularly difficult to survey [12]. The industry has adopted crowdsourcing paradigms such as the minimization of drive tests (MDT) to alleviate spatiotemporal sparsity [10], [11]. Nevertheless, commercial user equipment introduces significant measurement noise due to device heterogeneity and uncalibrated antenna configurations [13].

To bypass the constraints of physical data collection, computational electromagnetic methods including ray tracing (RT) and the dominant path model (DPM) have been widely employed [14], [15]. These computational electromagnetics methods serve as physical engines for synthesizing propagation data. However, the shooting and bouncing rays (SBR) algorithm faces severe scalability bottlenecks [14], [16]. Its computational complexity grows exponentially with the number of interaction orders. This renders ray-optical models too expensive for city-scale dynamic dataset generation [13], [17]. Recent differentiable RT frameworks such as Sionna [18] enable end-to-end gradient computation. They allow joint optimization of simulation parameters and neural network weights. Despite this progress, the millisecond-level latency required by real-time digital twins remains beyond the reach of pure simulation approaches [19].

To overcome these computational limitations, the field has shifted toward data-driven deep learning (DL) methodologies [13], [17], [20]. DL models function as differentiable surrogate models that implicitly encode wave propagation laws [21], [22]. They approximate electromagnetic responses in near real-time while maintaining fidelity to ground-truth physics. Based on this paradigm, this tutorial establishes a core taxonomy for RM construction. It categorizes the problem into two formulations: source-aware forward prediction and

This work was supported by the National Key Research and Development Program of China (2024YFB907500).

Xiucheng Wang, and Nan Cheng are with the State Key Laboratory of ISN and School of Telecommunications Engineering, Xidian University, Xi'an 710071, China (e-mail: xcwang_1@stu.xidian.edu.cn; dr.nan.cheng@ieee.org); (Corresponding author: Nan Cheng.).

Yuhao Pan is with the Division of Integrative Systems and Design, Hong Kong University of Science and Technology, Hong Kong, China (e-mail: ypanca@connect.ust.hk)

source-agnostic inverse reconstruction.

In source-aware RM construction, the neural network receives complete knowledge of the propagation environment and transmitter parameters [21]–[23]. The network acts as a high-speed surrogate for rigorous physical solvers. Source-agnostic RM construction addresses scenarios where transmitter configurations are latent or unavailable [24]–[26]. Measurements are spatially sparse in these settings. From a signal processing perspective, this formulation constitutes a severely ill-posed nonlinear inverse problem [11]. The network must recover the global field distribution from limited partial observations.

Driven by these diverse problem formulations, the underlying neural architectures have evolved significantly. Early methods relied on convolutional neural networks (CNNs) to abstract propagation into two-dimensional pixel mapping problems [21], [22], [27]. However, fixed and localized receptive fields restrict CNNs from capturing long-range spatial dependencies [13]. Macroscopic shadowing and diffraction around distant obstacles require global spatial reasoning.

Vision transformers (ViTs) address this limitation through self-attention mechanisms [23], [26], [28], [29]. They process environmental features globally and establish correlations between distant geographic structures and local signal attenuation. This capability is valuable for inverse problems where sparse observations must be contextualized within the full environment [26], [30]. The token-based input representation of ViTs naturally accommodates variable-sized sparse point sets. This avoids the information dilution caused by rasterizing sparse measurements onto dense grids [26].

Graph neural networks (GNNs) have also been adopted to model the non-Euclidean nature of radio propagation [31]–[34]. They represent spatial elements as nodes and physical interactions as edges. This formulation translates classical propagation models into learnable graph structure priors [31]. GNNs naturally handle heterogeneous network entities and non-uniform spatial sampling.

To address severe degradation under extreme spatial sparsity, the community has transitioned from discriminative point estimation to generative paradigms. Generative adversarial networks (GANs) reformulate RM construction as a conditional generation problem [35]–[40]. Diffusion models further decompose generation into a sequence of tractable denoising operations [41]–[49]. They offer stable training dynamics and high sample fidelity [50]. Their stochastic nature also enables uncertainty quantification through Monte Carlo sampling over multiple realizations [41].

To overcome resolution bottlenecks inherent in discrete grid representations, researchers have adapted optical neural rendering techniques to the radio frequency domain. Neural radiance fields (NeRF) and 3D Gaussian splatting (3DGS) enable the construction of continuous wireless radiation fields [6], [51]–[53]. These optics-inspired representations explicitly model the volumetric propagation process. They achieve high physical fidelity in complex-valued channel reconstruction. However, per-scene optimization requirements currently limit their applicability to dynamic environments [6].

Purely data-driven models remain inherently unconstrained in their latent spaces. This frequently leads to physical hallu-

cinations that violate foundational electromagnetic rules [42], [54]. Physics-informed methodologies address this challenge by embedding fundamental laws directly into the learning pipeline [54]–[58]. Maxwell’s equations and the Helmholtz equation can be incorporated into data representations, loss functions, and network architectures [42], [57], [59]. This tutorial introduces a three-level integration taxonomy for these approaches. The taxonomy encompasses data-level feature engineering, loss-level partial differential equation (PDE) regularization, and architecture-level structural isomorphism [42], [57], [59], [60].

A. Related Works

Although RM construction and wireless deep learning have attracted significant attention, existing surveys focus on different aspects. Doha and Abdelhadi [61] provide a comprehensive roadmap for integrating deep learning into wireless receivers. Their scope is confined to temporal and symbol-level processing at the receiver end. This focus is fundamentally distinct from the spatial, environment-scale field reconstruction addressed in this tutorial. Vasudevan and Yuksel [13] offer a broad overview of machine learning for radio propagation. Their coverage emphasizes traditional regression-based algorithms such as random forests and support vector machines. Zeng et al. [5] present a visionary tutorial on the channel knowledge map concept and its network-level applications. Regarding map construction, their discussion relies on classical spatial interpolation techniques like Kriging and tensor completion. Our tutorial, in contrast, treats RM construction as a complex inverse problem and explores advanced generative paradigms. Feng et al. [62] provide a solid categorization of RM estimation methods into model-driven, data-driven, and hybrid approaches. Their architectural coverage extends to ViTs and conditional GANs. However, the existing literature largely views RM construction as a deterministic interpolation or image-to-image translation task. Our tutorial advances beyond this view in three respects. First, we introduce probabilistic generative paradigms to handle extreme spatial sparsity and quantify uncertainty [41], [50]. Second, we systematically review and mathematically adapt optics-inspired neural rendering techniques to the complex-valued RF domain [6], [53]. Third, we propose a rigorous three-level taxonomy for physics-informed integration and formally define the concept of physical hallucinations [42]. A detailed comparison with existing surveys is presented in Table I.

B. Contributions

The main contributions of this tutorial are summarized as follows.

- 1) We present a comprehensive data ecosystem for RM construction. We systematically review physical measurement techniques [10], [11], RT simulation engines [14], [15], [18], and publicly available benchmark datasets [21], [22], [43]. We identify their respective strengths and limitations while providing practitioner-oriented guidance for dataset selection.

TABLE I: Comparison of This Tutorial with Existing Related Surveys

Feature or Dimension	Doha and Abdelhadi (2025) [61]	Zeng et al. (2024) [5]	Vasudevan and Yuksel (2024) [13]	Feng et al. (2025) [62]	Our Tutorial (This Work)
Primary Focus	Deep learning in physical-layer receiver modules	Concept and network-level utilization of channel knowledge maps	General machine learning for path loss and propagation	Classification of RM estimation methods	Advanced deep learning paradigms and physics-aware construction
Problem Formulation	Symbol detection, decoding, and equalization	Spatial interpolation and database querying	Regression and classification	Spatial interpolation and image mapping	Forward prediction versus inverse reconstruction
Architecture Depth	MLP, CNN, RNN, and basic autoencoders	Shallow autoencoders and UNet	Basic MLP, CNN, and decision trees	Intermediate CNN, ViT, and conditional GANs	Deep CNN, ViT, GNN, GAN, and diffusion models
Optics-Inspired RF Modeling	Not covered	Not covered	Not covered	Not covered	Extensive coverage of RF-NeRF and RF-3DGS
Physics Integration	Not applicable	Not covered	Not covered	Basic concatenation of empirical models	Rigorous 3-level taxonomy of data, loss, and architecture
Extreme Sparsity	Not applicable	Kriging and matrix completion	Traditional machine learning interpolation	CNN and GAN inpainting	Diffusion models, generative priors, and point-set ViTs
Key Novelty	DNN-to-module mapping for receivers	Formalizing environment-aware communications	Machine learning for drive test minimization	Categorization by dependency on model knowledge	Formalizing physical hallucinations and continuous RF fields

- 2) We establish a unified architectural taxonomy organized by the forward-inverse problem dichotomy. This taxonomy spans CNNs [21], [22], ViTs [23], [26], [28], GNNs [31]–[33], GANs [35]–[37], diffusion models [41]–[43], [63], and optics-inspired neural rendering methods [6], [51]–[53], [64], [65]. Cross-architecture comparisons clarify the trade-offs among inference latency, data efficiency, and spatial modeling capability.
- 3) We introduce a physics-informed integration framework that categorizes embedding strategies by their depth of physical coupling [42], [55], [56], [59], [60]. This framework provides actionable recipes for practitioners to incorporate electromagnetic knowledge incrementally. Open challenges including foundation model development, physical hallucination detection, and amortized inference for real-time deployment are discussed throughout.

II. PRELIMINARIES

This section introduces the mathematical foundations required for subsequent discussions. We first define the radio map and its key properties. We then review three generative

and rendering frameworks that serve as building blocks for RM construction: diffusion models, NeRF, and 3DGS.

A. Definition and Characterization of Radio Map

A radio map is a spatially continuous representation of the electromagnetic (EM) field distribution within a geographic region of interest [5], [7]. Unlike isolated signal measurements at discrete locations, an RM encodes the full spatial pattern as a structured, queryable representation. This enables inference, planning, and optimization tasks in wireless systems [8], [11].

1) *Electromagnetic Foundation:* The spatial distribution of the EM field is governed by Maxwell’s equations [66], [67]. In the frequency domain, these reduce to the scalar Helmholtz equation for the complex field amplitude $u(\mathbf{r})$ at position \mathbf{r} :

$$\nabla^2 u(\mathbf{r}) + k^2(\mathbf{r}) u(\mathbf{r}) = -f(\mathbf{r}), \quad (1)$$

where $k(\mathbf{r})$ is the spatially varying wavenumber determined by local permittivity and conductivity, and $f(\mathbf{r})$ is the source excitation term. This equation governs free-space spreading, specular reflection, diffraction, and material penetration loss [67]. An RM is therefore a discretized solution of the boundary-value problem defined by (1) over the spatial domain Ω .

TABLE II: Systematic Comparison of Radio Map, Channel Knowledge Map, and Radio Environment Map [5], [7], [11]

Attribute	Radio Map	Channel Knowledge Map	Radio Environment Map
Core quantity	EM field state: power, angle, delay	Tx–Rx impulse response	Multi-layer knowledge base: spectrum, interference, policy
Physical basis	Helmholtz/Maxwell solution; field-theoretic [54]	System-theoretic: link input–output response [5]	Network-level abstraction; not tied to a single PDE
Mathematical formulation	$P(\mathbf{r}) = u(\mathbf{r}) ^2$ from Helmholtz	$h(\mathbf{r}; \tau)$: channel impulse response	Aggregated database; no unified form
Tx dependency	Source-agnostic; supports unknown or multiple Tx via superposition	Tied to a specific Tx–Rx pair [5]	Configuration-dependent; may aggregate links
Superposition	Linear in power under incoherent conditions [21]	Linear in impulse response, but per-pair processing required	Not applicable; database-level concept
Data acquisition	From raw RSS via interpolation or field inversion [10]	Requires channel sounding and impulse-response extraction [3]	Aggregated from sensors, databases, operator records [11]
APS/PDP support	Native; multi-channel image or 4-D tensor [43]	Accessible via post-processing algorithms	Not a primary representation
Relation to PINNs	Directly governed by (1); PDE residual is well-defined [54], [56]	PDE constraint less natural in transfer-function domain	No direct PDE formulation
Typical application	Coverage prediction, beam management, localization [8], [21]	Site-specific channel database, precoder design [5]	Cognitive radio, dynamic spectrum access [11]

This PDE-rooted nature carries an important implication. The spatial values in an RM are not statistically independent samples. They are strongly correlated through the differential constraints of the underlying physics [54]. Any physically consistent RM construction method must respect these constraints. This observation motivates physics-informed neural networks (PINNs) [54]–[56], which incorporate the residual of (1) as a regularization term in the training loss. This ensures consistency with the wave equation even where measured data are absent.

2) *Multi-Dimensional Representation*: A complete EM field characterization requires power, angular, and delay information [5]. Depending on the application, an RM can be organized into a hierarchy of increasing dimensionality.

At the most compact level, the power-domain RM captures the spatially distributed RSS at each grid point. It is expressible as a single-channel image $\mathbf{P} \in \mathbb{R}^{H \times W}$ [21], [22]. This form aligns naturally with standard CNN input conventions.

At the second level, the angular and delay domain RM encodes the angular power spectrum (APS) and the power delay profile (PDP) as multi-channel images [43]. Each channel corresponds to a specific angular bin or delay tap. This captures the second-order spatial statistics of the multipath channel.

At the highest level, the four-dimensional RM represents a full delay-angle-power tensor $\mathbf{T} \in \mathbb{R}^{H \times W \times N_\tau \times N_\theta}$ [7], [43].

It jointly encodes power as a function of delay τ and angle θ at every location. This enables direction of arrival (DoA), direction of departure (DoD), and joint spectral maps.

3) *Distinction from Related Concepts*: Two concepts frequently appear alongside the RM: the channel knowledge map (CKM) [5] and the radio environment map (REM) [11]. Each rests on a different abstraction. Table II compares them along nine key attributes.

The CKM is a spatial distribution of impulse responses $h(\mathbf{r}; \tau)$ [5]. Each response characterizes the input–output behavior between a fixed transmitter and a receiver at \mathbf{r} . The power-domain RM corresponds to the steady-state field energy $P(\mathbf{r}) = |u(\mathbf{r})|^2$, where $u(\mathbf{r})$ solves (1). When multiple transmitters are present, the aggregate field satisfies:

$$P(\mathbf{r}) = \left| \sum_{m=1}^M u_m(\mathbf{r}) \right|^2 \approx \sum_{m=1}^M |u_m(\mathbf{r})|^2 = \sum_{m=1}^M P_m(\mathbf{r}), \quad (2)$$

where the approximation holds under incoherent superposition [21]. This assumption is valid for signals on distinct carriers or with uncorrelated phases. Equation (2) shows that the multi-source RM equals the sum of per-source power maps. This property simplifies both measurement and reconstruction.

The REM is a system-level knowledge repository [11].

TABLE III: Intrinsic Properties of the Radio Map

Property	Description
Spatial continuity	$u(\mathbf{r})$ solves the elliptic equation (1); smooth except at material interfaces; strong spatial correlation [54]
Linear superposition	Under incoherent conditions, the power-domain RM satisfies (2); modular per-source construction [21]
Environment coupling	$k^2(\mathbf{r})$ encodes geometry and materials; building layouts are informative in data-sparse regions [21], [22]
Direct measurability	Power-domain RM can be estimated from raw RSS without channel sounding hardware [10], [11]
Hierarchical extensibility	Scales from single-channel power map to 4-D delay-angle-power tensor [7], [43]

It encompasses spectrum occupancy, regulatory constraints, interference metrics, and user-behavior data. The RM defined here is a proper subset of the REM, constituting its physical field layer.

4) *Intrinsic Properties*: Several intrinsic properties of the RM, inherited from the wave equation, are relevant for subsequent discussions. Table III summarizes these five properties.

B. Diffusion Model

RM construction under extreme spatial sparsity demands generative models that produce physically plausible field distributions [41], [45]. Diffusion models provide a principled alternative to GANs and variational autoencoders (VAEs) [50], [68]. They decompose generation into a sequence of tractable denoising steps, yielding stable training and high sample fidelity.

1) *Discrete-Time Formulation*: The denoising diffusion probabilistic model (DDPM) [50] consists of two opposing Markov chains over T timesteps. The forward process corrupts a sample $\mathbf{x}_0 \sim q(\mathbf{x}_0)$ by injecting Gaussian noise:

$$q(\mathbf{x}_t|\mathbf{x}_{t-1}) = \mathcal{N}\left(\mathbf{x}_t; \sqrt{1 - \beta_t} \mathbf{x}_{t-1}, \beta_t \mathbf{I}\right), \quad (3)$$

where $\{\beta_t \in (0, 1)\}_{t=1}^T$ is the variance schedule. By defining $\alpha_t = 1 - \beta_t$ and $\bar{\alpha}_t = \prod_{i=1}^t \alpha_i$, direct sampling at arbitrary t is possible:

$$\mathbf{x}_t = \sqrt{\bar{\alpha}_t} \mathbf{x}_0 + \sqrt{1 - \bar{\alpha}_t} \boldsymbol{\epsilon}, \quad \boldsymbol{\epsilon} \sim \mathcal{N}(\mathbf{0}, \mathbf{I}). \quad (4)$$

The reverse process recovers \mathbf{x}_0 from noise $\mathbf{x}_T \sim \mathcal{N}(\mathbf{0}, \mathbf{I})$. A neural network approximates this as:

$$p_\theta(\mathbf{x}_{t-1}|\mathbf{x}_t) = \mathcal{N}(\mathbf{x}_{t-1}; \boldsymbol{\mu}_\theta(\mathbf{x}_t, t), \boldsymbol{\Sigma}_\theta(\mathbf{x}_t, t)). \quad (5)$$

Matching this to the forward posterior via variational optimization, the training objective simplifies to noise prediction [50]:

$$\mathcal{L}_{\text{DDPM}}(\theta) = \mathbb{E}_{t, \mathbf{x}_0, \boldsymbol{\epsilon}} \left[\|\boldsymbol{\epsilon} - \boldsymbol{\epsilon}_\theta(\mathbf{x}_t, t)\|^2 \right]. \quad (6)$$

2) *Continuous-Time SDE Generalization*: The discrete steps can be generalized to a continuous-time SDE framework [69]. As $T \rightarrow \infty$, the forward chain converges to the Itô SDE:

$$d\mathbf{x} = \mathbf{f}(\mathbf{x}, t)dt + g(t)d\mathbf{w}, \quad (7)$$

where $\mathbf{f}(\mathbf{x}, t)$ is the drift coefficient and $g(t)$ controls noise magnitude. Anderson's theorem [70] guarantees a reverse-time SDE:

$$d\mathbf{x} = [\mathbf{f}(\mathbf{x}, t) - g(t)^2 \nabla_{\mathbf{x}} \log p_t(\mathbf{x})] dt + g(t)d\bar{\mathbf{w}}, \quad (8)$$

where $\nabla_{\mathbf{x}} \log p_t(\mathbf{x})$ is the score function. A score network $s_\theta(\mathbf{x}, t)$ approximates this gradient via denoising score matching [71].

3) *Relevance to Wireless Channel Modeling*: The continuous-time formulation offers two advantages for wireless applications. First, adaptive ODE/SDE solvers with variable step sizes can accelerate inference [69]. Second, it connects diffusion to stochastic optimal control, enabling physics-informed integration [42]. In practice, many wireless RM methods adopt the discrete DDPM for its simplicity and stable convergence [41], [43], [44], [48].

C. Neural Radiance Fields

NeRF represents 3D scenes as continuous volumetric functions parameterized by neural networks [72]. The scene is modeled as a 5D mapping from spatial location $\mathbf{x} = (x, y, z)$ and viewing direction $\mathbf{d} = (\theta, \phi)$ to volume density σ and emitted radiance $\mathbf{c} = (r, g, b)$ via an MLP: $F_\Theta : (\mathbf{x}, \mathbf{d}) \rightarrow (\mathbf{c}, \sigma)$.

1) *Volume Rendering*: To synthesize 2D images, NeRF uses differentiable volume rendering. For ray $\mathbf{r}(t) = \mathbf{o} + t\mathbf{d}$, the expected color is:

$$C(\mathbf{r}) = \int_{t_n}^{t_f} T(t) \sigma(\mathbf{r}(t)) \mathbf{c}(\mathbf{r}(t), \mathbf{d}) dt, \quad (9)$$

where $T(t) = \exp(-\int_{t_n}^t \sigma(\mathbf{r}(s)) ds)$ is the accumulated transmittance. This integral is approximated via stratified sampling over N bins:

$$\hat{C}(\mathbf{r}) = \sum_{i=1}^N T_i (1 - \exp(-\sigma_i \delta_i)) \mathbf{c}_i. \quad (10)$$

A moderate N suffices for smooth optical variations. In the RF domain, longer wavelengths produce phase-sensitive multipath interference. This requires finer spatial resolution along each ray [6], [55].

2) *Positional Encoding*: To address the spectral bias of deep networks, NeRF projects coordinates into a higher-dimensional space using Fourier features. The encoding for $p \in [-1, 1]$ is:

$$\gamma(p) = (\sin(2^k \pi p), \cos(2^k \pi p))_{k=0}^{L-1}, \quad (11)$$

where L is the number of frequency bands. In the RF domain, the highest frequency $2^{L-1} \pi$ must resolve variations on the

order of $\lambda/2$ [51]. For the upper sub-6 GHz band where $\lambda \approx 5\text{--}10$ cm, the required L is smaller than in optical NeRF. The network is optimized using L_2 loss: $\mathcal{L} = \sum_{\mathbf{r} \in \mathcal{R}} \|\hat{\mathbf{C}}(\mathbf{r}) - C_{\text{gt}}(\mathbf{r})\|_2^2$.

3) *Limitations for RF Adaptation*: The optical NeRF formulation operates on real-valued RGB intensities under ray-optics assumptions. Wireless RF signals are inherently complex-valued, involving both amplitude and phase. RF propagation at centimeter and millimeter wavelengths is dominated by multipath interference and diffraction [55], [67]. These physical disparities require substantial mathematical redesign, which is detailed in Section VII-A.

D. 3D Gaussian Splatting

While NeRF achieves high fidelity, its MLP-based ray-marching imposes substantial overhead. 3DGS introduces an efficient explicit alternative [82]. It models the scene with an ensemble of anisotropic 3D Gaussians. Each primitive has center $\boldsymbol{\mu} \in \mathbb{R}^3$ and covariance $\boldsymbol{\Sigma} \in \mathbb{R}^{3 \times 3}$.

1) *Covariance Parameterization*: To ensure $\boldsymbol{\Sigma}$ remains positive semi-definite, 3DGS decomposes it as $\boldsymbol{\Sigma} = \mathbf{R}\mathbf{S}\mathbf{S}^T\mathbf{R}^T$ [82]. Here \mathbf{S} is a diagonal scaling matrix and \mathbf{R} is derived from a normalized quaternion $\mathbf{q} = [q_r, q_i, q_j, q_k]^T$ via the standard rotation formula.

2) *Directional Appearance*: View-dependent appearance is parameterized with spherical harmonics (SH) [82]: $\mathbf{c}(\mathbf{d}) = \sum_{l=0}^{L_{\text{max}}} \sum_{m=-l}^l \mathbf{k}_l^m Y_l^m(\mathbf{d})$. SH functions capture smooth optical illumination well. However, they poorly represent RF angular energy distributions [52], [53]. Coherent multipath at centimeter wavelengths produces sharp angular fluctuations. RF signals are also complex-valued, whereas standard SH encodes real-valued intensities. These issues motivate complex-valued Fourier-Legendre expansions for wireless 3DGS adaptation, as discussed in Section VII-B.

3) *Rendering*: The covariance is projected onto the image plane as $\boldsymbol{\Sigma}' = \mathbf{J}\mathbf{W}\boldsymbol{\Sigma}\mathbf{W}^T\mathbf{J}^T$, where \mathbf{W} is the world-to-camera transform and \mathbf{J} is the projection Jacobian. Pixel color is computed via front-to-back alpha compositing:

$$C(\mathbf{x}') = \sum_{i \in \mathcal{N}} \mathbf{c}_i \alpha_i \prod_{j=1}^{i-1} (1 - \alpha_j), \quad (12)$$

where α_i derives from the Gaussian footprint and an optimizable opacity. Adaptive density control clones or prunes Gaussians during training [82].

III. PROBLEM FORMULATION AND TAXONOMY

A. Mathematical Abstractions and Modeling

The physical propagation environment is defined within a continuous region of interest (ROI) $\mathcal{D} \subset \mathbb{R}^3$. For computational processing, this space is discretized into a grid $\mathcal{G} = \{g_1, g_2, \dots, g_N\}$, where N is the spatial resolution [5], [21]. The environment tensor is then constructed as $\mathbf{E} \in \mathbb{R}^{H \times W \times C_E}$.

The channel dimension C_E concatenates distinct physical descriptors:

$$C_E = C_{\text{geo}} + C_{\text{mat}} + C_{\text{sem}}. \quad (13)$$

Here, C_{geo} encodes spatial geometry such as obstacle locations and heights. C_{mat} defines electromagnetic material properties, including relative permittivity ϵ_r and conductivity σ . C_{sem} provides semantic indices that distinguish structures such as concrete walls, glass windows, and foliage [73], [79]. For a typical urban setup, one may set $C_{\text{geo}} = 1$, $C_{\text{mat}} = 2$, and $C_{\text{sem}} = 1$, yielding a 4-channel input tensor.

The choice of geometric dimensionality within C_{geo} depends on the deployment scenario [5], [41]. For simple indoor layouts or flat outdoor environments, the geometry is simplified as a 2D binary occupancy map $\mathbf{M}_{\text{occ}} \in \{0, 1\}^{H \times W}$ [21], [22]. For sub-6 GHz urban micro-cells where rooftop diffraction is important, a 2.5D normalized height map $\mathbf{M}_{\text{height}} \in [0, 1]^{H \times W}$ is needed [74]. Each pixel value encodes the normalized building height at that location. Full 3D voxel grids must be used for multi-floor indoor scenarios, urban canyons, or unmanned aerial vehicle (UAV)-to-ground links [24], [43]. These cases involve true 3D scattering and vertical volumetric interactions. The structural and material properties collectively serve as digital boundary conditions for the electromagnetic wave equation [58], [59].

Table IV provides a taxonomy that maps deployment scenarios to environment representations, transmitter encoding strategies, condition embedding mechanisms, and generalization boundaries. This table serves as a practitioner-oriented reference and is discussed in the following subsection.

B. Input Representation and Condition Embedding

The design of input representations and condition embedding is among the most important architectural decisions in RM construction [5], [13]. It directly determines the physical dimensions over which a trained model can generalize. This subsection provides a systematic guide on these design choices.

1) *Environment Representation*: The environment tensor \mathbf{E} can be encoded at varying levels of physical fidelity. Each level presents a trade-off between representational richness and generalization scope.

The simplest encoding is a 2D binary occupancy map $\mathbf{M}_{\text{occ}} \in \{0, 1\}^{H \times W}$, where each pixel marks obstacle presence. This representation is adopted in RadioUNet [21] and PMNet [22]. In these methods, the input has two channels: a building layout map and a transmitter location map. Binary encoding is lightweight and sufficient for single-floor indoor or flat suburban settings [27]. However, it discards all height information. A model trained on binary maps cannot distinguish a one-story house from a high-rise building.

To retain vertical geometry at low cost, 2.5D normalized height maps encode building height as a continuous value within $[0, 1]$ [6], [55]. For instance, the normalization $v_{\text{env}} = (h_{\text{env}} + 0.1)/3.1$ maps heights to pixel intensities [74]. Even zero-height structures remain distinguishable from open space. This encoding enables height-dependent effects such as rooftop diffraction and elevation-dependent shadowing [41]. However, the height axis is collapsed to a single scalar per pixel. Vertically overlapping structures such as bridges or multi-floor interiors cannot be captured.

At the highest fidelity, full 3D voxel grids $\mathbf{E} \in \mathbb{R}^{H \times W \times D \times C_E}$ preserve the complete volumetric geometry [24],

TABLE IV: Taxonomy of input representations, condition embedding strategies, and generalization boundaries for radio map construction. The rightmost column specifies the physical dimensions over which the trained model *cannot* generalize without retraining.

Deployment Scenario	Env. Representation (C_{geo})	Tx Position Encoding	Condition Embedding	Representative Methods	Generalization Boundary
Single-floor indoor (offices, corridors)	2D binary occupancy map $\mathbf{M}_{occ} \in \{0, 1\}^{H \times W}$	Binary mask channel $\mathbf{S}_{bin} \in \{0, 1\}^{H \times W}$	Input-level channel concatenation	RadioUNet [21], PMNet [22]	No height or 3D layout generalization
Sub-6 GHz urban micro/macro-cell	2.5D normalized height map $\mathbf{M}_{height} \in [0, 1]^{H \times W}$	Binary mask or Gaussian heatmap	Input-level channel concatenation	[55], [12], [6]	No material property generalization (ϵ_r, σ)
Indoor with materials and directional antennas	2D multi-channel tensor (reflectance, transmittance, FSPL)	Binary mask + antenna pattern channel	Input-level channel concatenation	SIP2Net [73], [27]	No cross-frequency generalization
3D indoor (multi-floor, furniture)	2D height-encoded pixel values $v_{env} = (h + 0.1)/3.1$	Binary mask channel; Tx height \rightarrow pixel value	Input concat; output channels as Rx heights	[74], [75]	Rx height fixed at training; no arbitrary 3D queries
UAV / air-to-ground (3D volumetric)	3D voxel grid or point cloud $\in \mathbb{R}^{H \times W \times D}$	Coordinate vector (x, y, z, f, P_t)	MLP embedding or Transformer cross-attention	CAED [76], [43]	Fixed voxel resolution; high memory for large scenes
Dynamic environments (moving vehicles)	Decoupled static + dynamic obstacle matrices ($\mathbf{H}_s, \mathbf{H}_d$)	Binary mask + Gaussian heatmap	Cross-attention (separate prompts)	RadioDiff [41], RadioDiff-Flux [63]	Heuristic decoupling; no scatterer-level detail
Beam-aware CKM (continuous beamforming)	2.5D building map + Tx position map \mathbf{T}	Binary mask channel for Tx location	Adaptive layer norm. (adaLN) for beam w	[77], [78]	Zero-shot generalization to unseen beam vectors
Multi-band / cross-freq. radio mapping	Height map + ITU material tensors ($\epsilon_r(f), \sigma(f)$)	Binary mask + freq. as scalar input	Physics-derived feature tensors (FSPL, gain)	[58], [79]	Explicit frequency input enables cross-band transfer
Universal / foundation model paradigm	3D building density + height topology	Sparse measurements + frequency + Rx height	Memory-based prompt learning (key-value pool)	[80], [81]	Prompt-based adaptation to new scenarios

[43]. These are essential for UAV-to-ground and multi-floor indoor modeling. However, they impose large memory and computational costs. The fixed voxel resolution also constrains spatial precision. An alternative approach maps the 3D output into multiple 2D channels, where each channel corresponds to a discrete receiver height [74], [75]. This achieves 3D coverage prediction within a standard 2D convolutional framework.

Beyond geometry, electromagnetic material properties extend generalization scope [58], [73]. When the tensor encodes frequency-dependent permittivity $\epsilon_r(f)$ and conductivity $\sigma(f)$ as additional channels, the network learns material-specific attenuation [79]. Models that omit materials are confined to the frequency band and material distribution of the training data.

2) *Transmitter Position Encoding*: The transmitter location \mathbf{S} can be represented through several strategies. The most common approach uses a binary spatial mask $\mathbf{S}_{bin} \in \{0, 1\}^{H \times W}$ [21], [22]. A single activated pixel marks the transmitter position. This mask is concatenated with \mathbf{E} along the channel dimension to form $[\mathbf{E}; \mathbf{S}_{bin}]$. While simple, binary masks quantize the transmitter to discrete grid locations.

To enable continuous positioning, several works parameterize the transmitter as a 2D Gaussian heatmap [41]:

$$\mathbf{P}(j, k) = \exp\left(-\frac{(j-a)^2 + (k-b)^2}{2\sigma_s^2}\right), \quad (14)$$

where (a, b) are continuous transmitter coordinates and σ_s controls the spatial spread. This soft representation allows differentiable backpropagation through the location. It is essential for joint RM generation and transmitter localization [83], [84]. The Gaussian heatmap also encodes spatial uncertainty, and its peak sharpens as the model converges.

For additional transmitter parameters such as transmit power P_t , carrier frequency f_c , or antenna downtilt θ_{tilt} , these scalars can be embedded via multi-layer perceptron (MLP) mappings [23], [85]. Including such parameters as explicit inputs is essential for cross-configuration generalization. A model with frequency as input can generalize to new bands; a model trained

at a fixed frequency cannot.

3) *Condition Embedding Mechanisms*: The mechanism by which conditions are injected into the architecture determines how effectively the model leverages them. Three strategies are employed in the literature.

Input-level channel concatenation is the simplest approach. All condition tensors are stacked along the channel dimension and fed as a unified input [21], [22]. For example, RadioUNet concatenates the building map and transmitter mask into a 2-channel tensor. SIP2Net [73] extends this to a 5-channel tensor with reflectance, transmittance, distance, free-space path loss (FSPL), and antenna pattern maps. This strategy is simple and requires no additional components. However, it treats all channels homogeneously, without selective modulation based on specific physical parameters.

Cross-attention conditioning provides a more expressive alternative [26], [29]. The environment or transmitter features are encoded separately and injected via cross-attention layers. The network's intermediate features serve as queries, and the condition embeddings serve as keys and values. RadioDiff [41] uses cross-attention to inject static and dynamic obstacle features as separate prompts. This mechanism accommodates conditions of different resolutions or modalities. It also allows spatially varying attention that aligns structures with local signal behavior. The computational cost scales with the number of attention layers and sequence length.

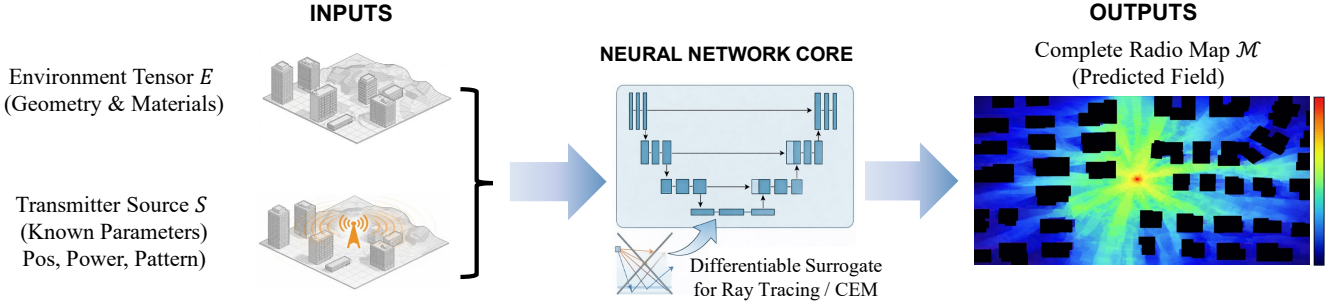
Adaptive layer normalization (adaLN) offers a parameter-efficient alternative for scalar or low-dimensional conditions [42]. It dynamically generates scale and shift parameters from the condition embedding \mathbf{c}_{emb} :

$$\text{adaLN}(\mathbf{f}, \mathbf{c}_{emb}) = (1 + \gamma) \odot \mathcal{N}(\mathbf{f}) + \beta, \quad (15)$$

$$[\gamma, \beta] = \text{MLP}(\mathbf{c}_{emb}). \quad (16)$$

The scale factor γ adjusts feature amplitudes to match the beam's spatial power distribution. The shift factor β modulates the baseline signal level. This mechanism suits conditions that exert a global influence on the output, such as carrier frequency or transmit power [77], [86]. For spatially varying conditions

PART A: SOURCE-AWARE FORWARD PREDICTION (Deterministically Modeling Propagation)



PART B: SOURCE-AGNOSTIC INVERSE RECONSTRUCTION (Ill-Posed Sparse to Dense Interpolation)

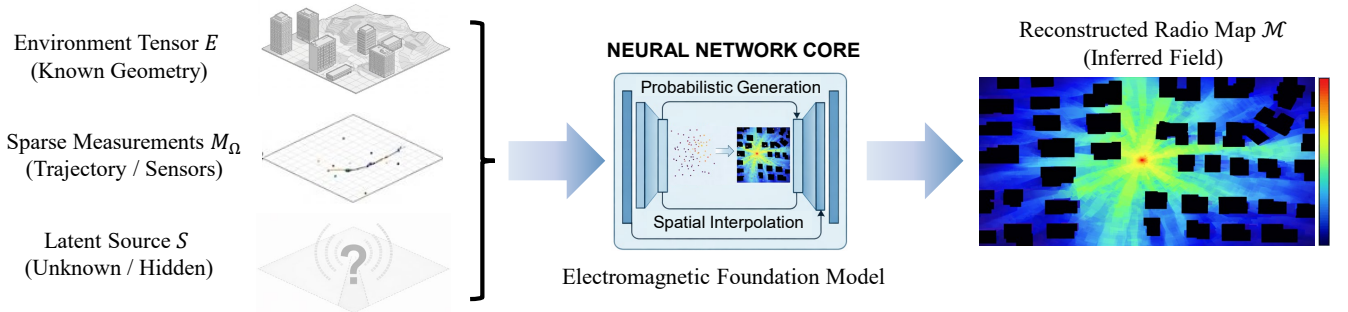


Fig. 1: Two primary paradigms of neural RM construction. Part A illustrates source-aware modeling, where neural networks act as deterministic surrogates for ray tracing using known environment and transmitter inputs. Part B illustrates source-agnostic reconstruction, which represents an ill-posed inverse problem that leverages probabilistic generation to interpolate complete radio fields from sparse, incomplete measurements.

like building geometry, adaLN must be complemented by spatial conditioning.

In practice, state-of-the-art frameworks combine multiple strategies [80], [81]. For instance, one may use input concatenation for the spatial environment map, a convolutional encoder for spatial features, and adaLN for continuous beam vectors.

4) *Generalization Boundaries Determined by Input Design:* A key insight from the above discussion is that generalization is bounded by what is explicitly represented in the input [5], [13]. A model cannot generalize over a physical dimension absent from its input.

If the environment is a binary occupancy map, the model cannot distinguish buildings of different heights. If the transmitter location is hard-coded rather than parameterized, the model cannot handle unseen positions. If the carrier frequency is implicit in training data, the model is confined to that single band [58], [79].

This observation leads to a principled design methodology. Practitioners should first identify all physical dimensions requiring generalization, such as geometry, materials, transmitter configuration, frequency, and antenna pattern. Each dimension must be explicitly represented in the input tensor and injected through an appropriate embedding mechanism. Table IV systematizes this design space and identifies the generalization boundary for each common configuration.

C. The Forward Problem: Source-Aware Radio Mapping

Fig. 1 contrasts the two primary paradigms of neural RM construction: source-aware forward prediction and source-

agnostic inverse reconstruction. Source-aware radio mapping is a forward prediction problem. The objective is to predict global electromagnetic coverage given the propagation environment \mathbf{E} and transmitter parameters \mathbf{S} [21], [41].

Deep neural networks in this setting approximate rigorous computational electromagnetic solvers [58], [59]. They serve as surrogate models for ray tracing engines or full-wave Maxwell's equation solvers. However, constructing an accurate forward mapping is challenging. The mapping from \mathbf{E} to the signal distribution is a highly sensitive nonlinear function [79]. Minor changes in wall thickness or obstacle displacement can cause large variations due to phase shifts and multipath interference.

The problem becomes more complex with multiple transmitters. The aggregated field at location \mathbf{r} from K transmitters must follow one of two regimes. The first is incoherent power addition:

$$\mathbf{M}(\mathbf{r}) = \sum_{k=1}^K P_k |H_k(\mathbf{r})|^2, \quad (17)$$

where P_k is the transmit power and H_k is the complex channel response of the k -th transmitter. The second regime is coherent superposition:

$$\mathbf{M}(\mathbf{r}) = \left| \sum_{k=1}^K \sqrt{P_k} H_k(\mathbf{r}) e^{j\phi_k} \right|^2, \quad (18)$$

which accounts for the initial carrier phases ϕ_k and resulting interference.

The choice of regime depends on the physical coherence con-

ditions [87], [88]. Incoherent addition applies when transmitters operate independently, as in conventional orthogonal frequency division multiple access (OFDMA) inter-cell interference [89], [90]. Each base station transmits asynchronously, and cross-cell signals combine on a power basis. Coherent superposition applies when transmitters share a common phase reference [91]. Examples include distributed MIMO with joint transmission and reconfigurable intelligent surface (RIS)-assisted links. Ignoring phase coherence in such scenarios underestimates the signal-to-noise ratio in constructive regions and overestimates it in destructive zones. This distinction requires architectures that handle global context and complex signal interactions across the spatial domain [23], [26].

D. The Inverse Problem: Source-Agnostic Radio Mapping

Source-agnostic radio mapping is an inverse reconstruction problem. The transmitter parameters \mathbf{S} are latent or unavailable [24], [25]. The goal is to reconstruct the complete RM \mathbf{M} from the environment tensor \mathbf{E} and sparse measurements $\mathbf{M}_\Omega = \{(x_i, y_i, v_i)\}_{i=1}^m$, where $m \ll N$.

This task is an ill-posed non-linear inverse problem [92], [93]. The observed measurements \mathbf{y} can be formulated as:

$$\mathbf{y} = \mathcal{A}(\mathbf{P}_\Omega \odot \mathbf{M}) + \mathbf{n}, \quad (19)$$

where \mathbf{n} is additive measurement noise. Here, \mathbf{P}_Ω is a linear binary sampling mask applied via the Hadamard product \odot to select m locations. $\mathcal{A}(\cdot)$ is the non-linear degradation function of receiver hardware, including sensitivity thresholds, dynamic range saturation, and quantization [93].

Reconstructing \mathbf{M} from \mathbf{y} is ill-posed because the sampling operator is singular and the solution is non-unique [24], [92]. Multiple source-environment combinations could yield identical sparse observations. The network must incorporate strong structural priors to regularize this inversion [58], [59]. Two canonical priors are widely used. The first is the sparsity of dominant multipath components in the angular domain [3]. Only a limited number of scattering clusters contribute significantly at any location. The second is the low-rank structure of the spatial channel matrix [94]. It is important to note that a single-frequency power map from one transmitter does not inherently exhibit low-rank structure. Low-rank structure arises under specific conditions: for narrowband massive MIMO channels, it results from the limited angular spread relative to the array aperture; for spatially distributed RMs, it can emerge when the map is organized as a spatial-frequency tensor across multiple sub-bands where all frequency slices share common propagation paths [95]. Practitioners should verify the applicability of low-rank assumptions for their specific RM modality. The learning model must exploit these priors, embedded within \mathbf{E} , to infer the latent source \mathbf{S} [45], [83]. It must also reconstruct physically consistent signal variations in deep shadowing zones where no measurements exist [26], [29].

E. Environmental Constraints and Domains

The design of learning-based RM frameworks is constrained by the propagation domain [5], [13]. Indoor scenarios are

confined environments dominated by wall penetration losses and dense 3D multipath reflections [27], [73]. They require high-precision representations such as 3D point clouds or building information modeling (BIM) data. Specialized architectures like GNNs or 3D CNNs are needed to encode non-Euclidean structural adjacencies in multi-room layouts [31], [32].

Outdoor scenarios operate at macroscopic scale [21], [41]. They are driven by line-of-sight (LoS) blockages, large-scale shadowing, and rooftop diffraction. Represented mainly by 2.5D digital surface models (DSMs), outdoor RM modeling suffers from measurement sparsity over large areas [96], [97]. Architectures with global receptive fields, such as Transformers, are needed to capture long-distance blockage correlations [23], [26], [29].

F. Target RM and Mapping Function

The target RM is a tensor $\mathbf{M} \in \mathbb{R}^{H \times W \times C_M}$. The channel dimension C_M encodes specific metrics of the wireless channel state [5], [91]. For example, $C_M = 3$ may comprise a RSS channel in dBm, a time of arrival (ToA) channel in nanoseconds, and a signal-to-interference-plus-noise ratio (SINR) channel in dB.

The mapping function parameterized by weights θ is defined differently for each problem type. For the source-aware forward task, the network acts as a differentiable surrogate solver [21], [41]:

$$\mathbf{M} = \mathcal{F}_\theta(\mathbf{E}, \mathbf{S}_{\text{known}}). \quad (20)$$

For the source-agnostic inverse task, the network acts as a spatial interpolator and latent source estimator [24], [25]:

$$\mathbf{M} = \mathcal{R}_\theta(\mathbf{E}, \mathbf{M}_\Omega). \quad (21)$$

G. Discussion on Sampling Paradox

A paradox arises in the source-agnostic inverse problem regarding sampling efficiency. Consider isotropic radiation under the Friis equation: $P_r(\mathbf{r}_i) = P_t G_t G_r \left(\frac{\lambda}{4\pi \|\mathbf{r}_i - \mathbf{r}_{tx}\|} \right)^2$. Under free-space propagation in the 2D plane with known antenna height, three non-collinear LoS measurements suffice to recover the transmitter location \mathbf{r}_{tx} and power P_t via trilateration [67]. However, this three-point sufficiency is only a thought experiment. In practice, multipath fading corrupts LoS measurements with spatial fluctuations of 5–15 dB [98]. This causes substantial errors in trilateration. In urban environments, diffraction, non-line-of-sight (NLoS) blockages, and frequency-selective fading invalidate the geometric inversion entirely [3], [41]. The key insight is that well-placed LoS samples carry redundant geometric information. The true reconstruction challenge lies in NLoS zones where simple distance-power relationships fail. Despite this, many existing works use uniform or random sampling [24], [25]. These strategies oversample predictable LoS regions while undersampling complex NLoS zones. Future strategies should adopt physics-aware adaptive sampling [99], [100]. Sensor placement can be guided by heuristics such as anchoring at diffraction corners, shadow boundaries, and high-entropy zones [79]. Alternatively, active

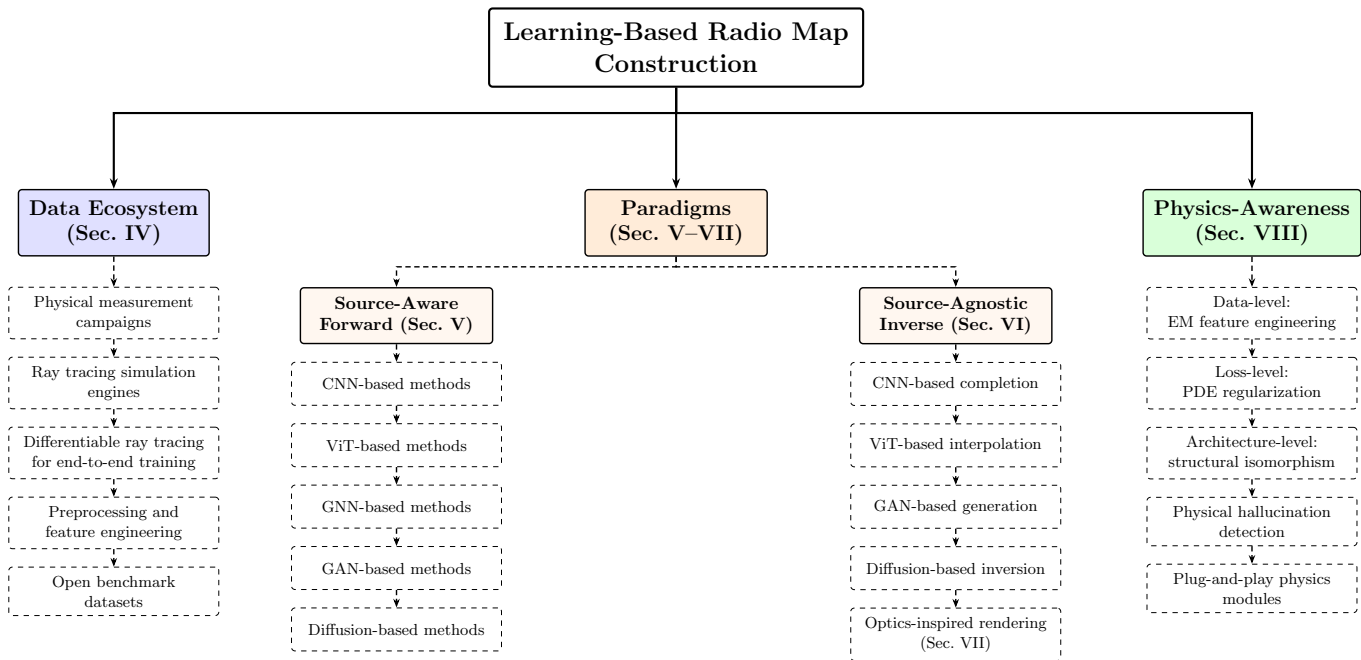


Fig. 2: The overall structure of this tutorial, organized along three intertwined dimensions: data ecosystem, learning paradigms, and physics-awareness.

learning frameworks can use predictive uncertainty maps to select high-variance NLoS locations [92]. Such strategies would improve sample efficiency by concentrating measurements where the physical field is least predictable from geometric priors alone.

IV. DATA ACQUISITION AND OPEN DATASETS

As outlined in Fig. 2, this tutorial addresses RM construction along three intertwined dimensions: data, paradigms, and physics-awareness. Beginning with the data dimension, high-quality datasets are essential for data-driven RM construction [5], [13]. This section reviews three data acquisition paradigms: physical measurement, ray tracing simulation, and differentiable simulation. It then discusses preprocessing strategies and catalogs publicly available benchmarks. The section concludes with dataset limitations and selection guidance. Fig. 3 illustrates the complete workflow from physical measurements and ray tracing simulations to standardized benchmark datasets.

A. Real-World Measurement Techniques

Physical measurement campaigns provide the ground truth for validating RM algorithms [11], [101]. While simulations offer scalability, measurements capture the stochastic nature of real channels. Complex multipath scattering and hardware impairments are often oversimplified in ray-optical models [4].

Traditional methodologies rely on dedicated drive tests (DT) and walk tests (WT) to collect geolocated signal quality indicators [10]. To extract the local average RSS, measurements adhere to Lee’s sampling criterion [102]. This requires averaging samples over approximately 40λ , where λ is the

carrier wavelength. The local average power P_{local} at location \mathbf{x} is:

$$P_{local}(\mathbf{x}) = \frac{1}{2L} \int_{x-L}^{x+L} P_{inst}(y) dy, \quad (22)$$

with L as the averaging window length. At sub-6 GHz frequencies where $\lambda \approx 5\text{--}10$ cm, this window spans approximately 2–4 m [103]. Spatially adjacent samples within this window are correlated and do not contribute independent information.

To address the sparsity of dedicated campaigns, crowdsourcing from commercial user equipment (UE) has been adopted [8], [11]. This is standardized by 3GPP as minimization of drive tests (MDT). MDT data enables high-temporal-resolution RMs but introduces device heterogeneity. The measured signal strength from a specific UE is modeled as $P_{meas} = P_{true} + \eta_{sf} + \eta_{device}$, where η_{device} denotes device-specific noise and antenna gain variation [104]. Statistical normalization per device model or collaborative filtering anchored by reference nodes is required to calibrate reports. Aerial sampling with unmanned aerial vehicles (UAVs) has extended RM construction into 3D volumetric space [99], [105]. UAV measurements often employ active learning for autonomous path planning. The objective is to maximize information gain \mathcal{I} along a trajectory \mathcal{T} subject to energy constraints. Under a Gaussian process (GP) model [106], the information gain is the reduction in predictive posterior entropy:

$$\mathcal{I}(\mathcal{T}) = H[\mathbf{M}_{\bar{\Omega}}|\mathbf{M}_{\Omega}] - H[\mathbf{M}_{\bar{\Omega}}|\mathbf{M}_{\Omega}, \mathbf{M}_{\mathcal{T}}], \quad (23)$$

where \mathbf{M}_{Ω} represents existing measurements, $\mathbf{M}_{\mathcal{T}}$ denotes candidate trajectory measurements, and $\mathbf{M}_{\bar{\Omega}}$ comprises unobserved field values. For a GP with kernel $k(\cdot, \cdot)$, this simplifies to $\mathcal{I}(\mathcal{T}) = \frac{1}{2} \log \det(\mathbf{I} + \sigma_n^{-2} \mathbf{K}_{\mathcal{T}, \mathcal{T}|\Omega})$ [92]. Maximizing this

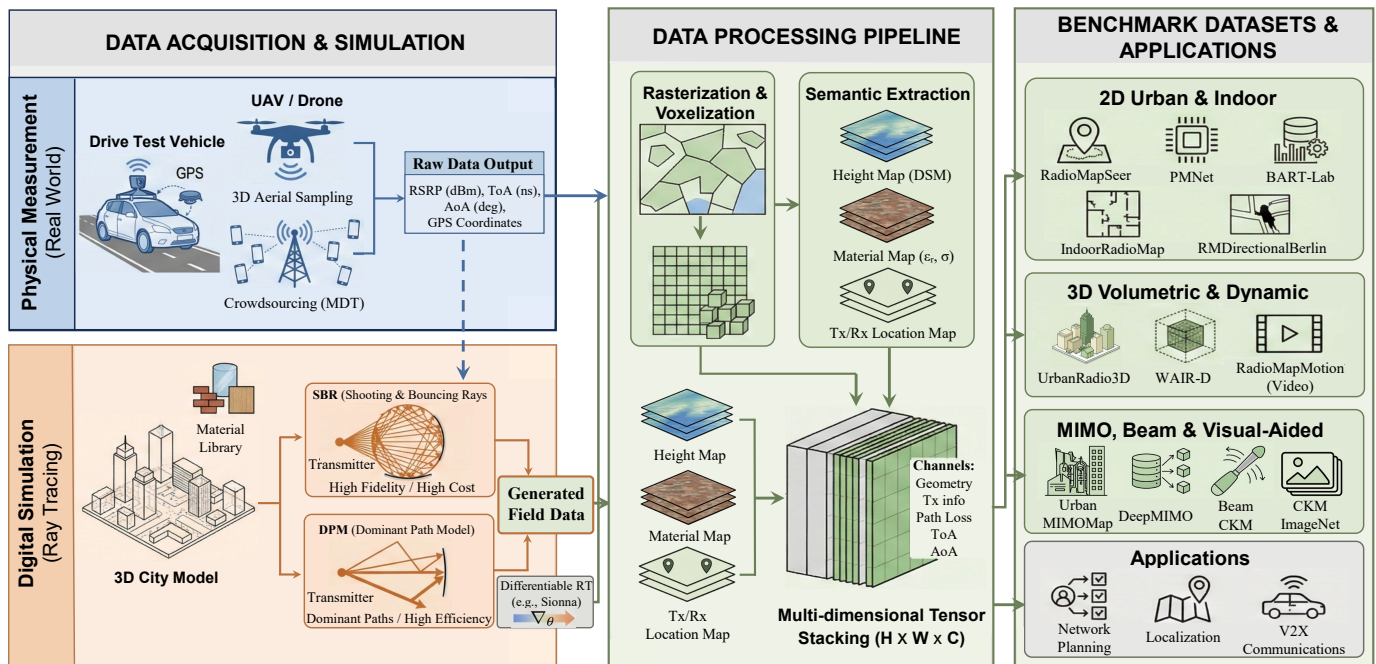


Fig. 3: Illustration of the RM data collection workflow. A comprehensive workflow bridging physical measurements and ray tracing simulations to generate standardized multi-dimensional benchmark datasets.

quantity directs the UAV to regions with highest predictive uncertainty, concentrating measurements in shadowing and non-line-of-sight (NLoS) zones [100].

B. Ray Tracing for Data Generation

Synthetic data generation relies on computational electromagnetics (CEM). Three algorithmic families are predominant: the shooting and bouncing rays (SBR) algorithm, the dominant path model (DPM), and differentiable ray tracing [14], [15], [18].

1) *Classical Forward Ray Tracing*: SBR launches millions of ray tubes from the transmitter [16]. The total received field \mathbf{E}_{total} is calculated by coherent superposition of all ray tubes intersecting the receiver volume:

$$\mathbf{E}_{total} = \sum_{n=1}^{N_{ray}} \mathbf{E}_n \cdot \prod_{i=1}^{K_n} \Gamma_i(\theta_i) \cdot \prod_{j=1}^{M_n} T_j(\psi_j) \cdot \frac{e^{-jk d_n}}{d_n}, \quad (24)$$

where \mathbf{E}_n is the initial field, $k = 2\pi/\lambda$ is the wavenumber, and d_n is the path length. Γ_i and T_j denote the Fresnel reflection and transmission coefficients, respectively. SBR captures multipath fading with high fidelity but scales as $\mathcal{O}(N_{rays} \times N_{obj}^{K_{max}})$, where N_{obj} is the polygon count and K_{max} the maximum interaction order [107]. This makes city-scale dataset generation expensive.

2) *Dominant Path Model*: The DPM builds on intelligent ray tracing (IRT) with pre-computed visibility trees [15]. It exploits the observation that over 95% of received energy comes from a sparse set of dominant paths [108]. These typically include the line-of-sight (LoS) path, first- and second-order reflections,

and main diffractions. The total path loss is:

$$PL_{total} = 20 \log_{10} \left(\frac{4\pi d}{\lambda} \right) + \sum_{i=1}^{N_{ref}} L_{ref,i} + \sum_{j=1}^{N_{diff}} L_{diff,j} + \sum_{k=1}^{N_{pen}} L_{pen,k}. \quad (25)$$

DPM reduces complexity to approximately $\mathcal{O}(N_{Rx} \times N_{obj})$ [14]. This efficiency is critical for generating large-scale training datasets. The trade-off is clear: SBR provides high fidelity with phase information at extreme computational cost, while DPM sacrifices high-order interactions for orders-of-magnitude faster generation [21].

3) *Differentiable Ray Tracing*: Differentiable ray tracing frameworks, exemplified by Sionna [18], implement the entire propagation computation graph using automatic differentiation. This enables end-to-end gradient computation with respect to scene parameters such as material properties and transmitter configurations [109]. The significance for RM construction is twofold. First, it provides a physics-grounded data generation engine that integrates into gradient-based training loops. Second, it supports inverse problems where environmental parameters are recovered from observations [18]. Several datasets in Table V, notably BeamCKM [110], employ Sionna with 10^9 rays following ITU-R standards. Practitioners are encouraged to evaluate such frameworks when constructing custom datasets, especially for domain adaptation from simulation to measurements.

C. Data Preprocessing and Representation

Raw spatial data must be transformed into standardized tensor representations via rasterization [5]. Vector-based CAD

TABLE V: Comparative summary of public datasets for RM construction. “Source” indicates ray tracing simulation (Sim.) or physical measurement (Meas.). † denotes parametric generation scripts rather than fixed maps.

Dataset	Dim.	Modality	Freq.	Source	Size	Key Features
2D Urban & Indoor Path Loss						
1 RadioMapSeer [21]	2D	Path loss	5.9 GHz	Sim. (DPM/IRT)	56,080 maps	Dual-engine; 701 maps × 80 Tx; 1 m res.; foundational benchmark
2 PMNet [22]	2D	PL + height	Multi	Sim. (WI)	~2,000 maps	Cross-city transfer learning
3 BART-Lab [31]	2D	PL (multi-band)	1.75–5.75 GHz	Sim. (Feko/WP)	2,100 maps	5 frequency bands; coarse and fine subsets
4 IndoorRadioMap [111]	2D	PL	Multi	Sim. (Ranplan)	25 envs.	0.25 m res.; material-encoded RGB; directional antennas
5 DeepREM [25]	2D	PL	2.4/LTE GHz	Sim. (WI)	8,400 maps	Rosslyn micro-scale; inverse benchmark
6 RMDirectionalBerlin [112]	2D	PL + RGBIR	Sub-6 GHz	Sim. (RT)	74,000 maps	9.3 TB; sector antennas; vegetation separation
3D Volumetric & Continuous						
7 UrbanRadio3D [43]	3D	PL, ToA, DoA	5.9 GHz	Sim. (WP)	11.2M pts	1 m vertical res.; 20 height layers; UAV support
8 RadioMap3DSeer [113]	3D	Path loss	3.5 GHz	Sim. (IRT)	56,080 maps	3D extension of RadioMapSeer
9 NeRF ² Benchmarks [51]	3D	Implicit field	Multi	Meas.	Multi-scene	BLE, MIMO CSI, RFID; real measurements
10 WAIR-D [114]	3D	Ray params	Multi	Sim. (RT)	10,000 envs	40 cities; sub-6 GHz to THz; foundation model
MIMO, Beam-Aware & Precoding						
11 UrbanMIMOMap [86]	2D	4 × 4 CSI	3.5 GHz	Sim. (RT)	3,000 maps	Full complex \mathbf{H} ; 0.5 m res.
12 BeamCKM [110]	2D	Beam RSRP	3 GHz	Sim. (Stionna)	10,000 maps	10 ⁹ rays; DFT codebook; 256 × 256 pixel
13 DeepMIMO [†] [115]	Config.	Channel matrix	mmWave	Sim. (WI)	Parametric	Arbitrary arrays; 28/60 GHz; script-based
Temporal & Dynamic						
14 RadioMapMotion [116]	2D+Time	Sequential frames	V2X	Sim. (RT)	1,500 seq.	Vehicle trajectories; video prediction
Cross-Modal & Vision-Aided						
15 CKMImageNet [5]	2D/3D	Visual + channel	Multi	Sim.	5,000 pairs	Satellite imagery paired with AoA, AoD, delay

or GIS maps are discretized into binary occupancy grids. Beyond simple occupancy, feature engineering embeds physical priors into the learning model [73], [79].

Electromagnetic waves undergo significant diffraction at sharp discontinuities [117]. Extracting geometric features as input channels reduces the network’s learning burden. Edge intensity maps \mathbf{F}_{edge} are computed using Sobel or Laplacian kernels, highlighting building walls where reflection losses concentrate. Diffraction is particularly dominant at structural corners. The uniform theory of diffraction (UTD) [117] establishes that corner geometries produce larger diffraction coefficients than smooth surfaces. Corner feature maps \mathbf{F}_{corner} , extracted via Harris or Shi-Tomasi detectors, provide the network with access to critical scattering sites [59], [79].

These geometric features are combined with material property maps encoding relative permittivity ϵ_r and conductivity σ [58]. Material values are typically assigned from ITU-R P.2040 recommendations. These deterministic assignments carry inherent uncertainties compared to physical reality, contributing to the simulation-to-reality gap [107]. The composite environment tensor $\mathbf{E} \in \mathbb{R}^{H \times W \times C_{in}}$ formed by concatenating these channels defines the boundary conditions for the learning model.

The number of input channels C_{in} represents a design trade-off. Including more physics-derived features, such as free-space path loss (FSPL) maps, distance fields, and antenna gain projections, reduces the network’s representational burden [73]. However, each additional channel increases preprocessing cost and may introduce approximation errors. Section III-B provides detailed guidance on how input design determines generalization boundaries.

D. Dataset Analysis and Benchmarks

Numerous publicly available datasets address specific challenges in 6G environment-aware communications [4], [5]. We organize them by primary data modality. Table V provides a comparative summary.

1) *2D Urban and Indoor Path Loss Datasets*: **RadioMapSeer** [21] is the foundational benchmark for 2D path loss prediction. It comprises 701 city maps with 80 transmitter positions per map, yielding a total of 56,080 radio maps simulated using both DPM and IRT engines at 5.9 GHz with 1 m resolution. As the most widely used benchmark, most methods in Sections V and VI report results on this dataset. Its main limitation is the absence of vertical information and multipath parameters.

PMNet Dataset [22] features RMs from real-world urban environments including USC and downtown Boston. Generated via Wireless InSite, it explicitly includes subsets with varying building densities for cross-city transfer learning evaluation.

BART-Lab Dataset [31] employs Feko and WinProp to simulate five frequency bands from 1.75 to 5.75 GHz within the same environment. A coarse subset with 2,000 maps enables rapid prototyping, while a fine subset with 100 maps supports high-fidelity reconstruction. This structure enables cross-band prediction research.

IndoorRadioMap [111] was released for the First Indoor Pathloss RM Prediction Challenge [118]. It includes 25 indoor environments with material properties encoded into RGB tensors at 0.25 m resolution. The simulation considers up to 8 reflections and 10 transmissions with directional antenna patterns.

DeepREM [25] focuses on the Rosslyn urban scenario at 2.4 GHz. It serves as a standard benchmark for sparse measurement interpolation algorithms including tensor completion and kriging [24].

RMDirectionalBerlin [112] bridges academic assumptions and industrial reality by modeling sectorized base stations. This 9.3 TB dataset includes 74,000 RMs with normalized digital surface models separating buildings from vegetation, alongside RGBIR aerial imagery.

2) *3D Volumetric and Continuous Datasets*: **UrbanRadio3D** [43] contains 11.2 million labeled points across 20 height layers from 1 m to 20 m. Generated at 5.9 GHz using WinProp, it provides time of arrival (ToA) and direction of

arrival (DoA) for every voxel. This makes it suitable for 3D network planning and UAV trajectory optimization [105].

NeRF² Benchmarks [51] represent a shift from discrete sampling to implicit continuous representation. Spanning BLE RSSI, MIMO CSI, and RFID spectra, they enable neural networks that encode the electromagnetic field as a continuous function. Notably, this is one of the few benchmarks grounded in physical measurements rather than simulation [119].

WAIR-D [114] provides 10,000 environments from 40 global cities, covering sub-6 GHz to terahertz frequencies. This breadth of environmental and spectral diversity supports foundation model training [81].

3) *MIMO, Beam-Aware, and Precoding Datasets*: **UrbanMIMOMap** [86] provides the full 4×4 complex channel state information (CSI) matrix \mathbf{H} at 0.5 m resolution. This enables direct computation of ergodic capacity and beamforming optimization [91].

BeamCKM [110] covers 100 urban maps with uniform linear array antennas at 3 GHz. Sionna generates data with 10^9 rays and ITU-R electromagnetic parameters. All DFT codebook codewords with $N_{BS} = 8$ are simulated, producing beam-specific channel knowledge maps at 256×256 pixel resolution with 40 dB dynamic range.

DeepMIMO [115] is a parametric generation framework rather than a fixed dataset. It generates channel matrices for arbitrary massive MIMO configurations at 28 and 60 GHz based on Wireless InSite scenarios. This flexibility makes it preferred for custom array geometries.

4) *Temporal and Dynamic Datasets*: **RadioMapMotion** [116] incorporates real-world vehicle trajectories to generate sequential RM frames. By formulating estimation as a video prediction task, it enables spatio-temporal architectures for predictive resource allocation in high-mobility scenarios [100], [120].

5) *Cross-Modal and Vision-Aided Datasets*: **CKMImageNet** [5] pairs multi-resolution satellite and aerial imagery with channel parameters including angle of arrival (AoA), angle of departure (AoD), and delay spread. This facilitates vision-aided beam prediction with zero or minimal pilot overhead [28], [121].

6) *Practitioner Guidance on Dataset Selection*: Given the diversity of benchmarks, the following guidelines are offered. For initial algorithm development, RadioMapSeer [21] remains the standard choice due to widespread adoption and published baselines. For cross-environment generalization, PMNet [22] and WAIR-D [114] provide structured train-test splits across distinct morphologies. For 3D volumetric or UAV research, UrbanRadio3D [43] is the most comprehensive option. For beam-aware or MIMO studies, BeamCKM [110] and UrbanMIMOMap [86] offer the necessary physical layer richness. Researchers concerned with the simulation-to-reality gap should prioritize NeRF² benchmarks [51], which are grounded in physical measurements.

E. Discussion on Dataset Limitations

Open-source datasets have accelerated RM research, but three fundamental limitations require awareness [4], [13].

1) *Simulation-Reality Gap*: The heavy reliance on synthetic solvers introduces a domain gap between training data and deployment [104], [107]. SBR-based datasets often exhibit stochastic noise from ray-tube undersampling rather than physical propagation. Networks trained on such data risk overfitting to algorithmic noise [122]. This motivates domain adaptation techniques and hybrid strategies combining simulated data with small quantities of real measurements [104], [123].

2) *Precision Loss and Resolution Limitations*: Encoding RMs as standard 8-bit images introduces quantization errors over dynamic ranges exceeding 100 dB. With 256 levels spanning 100 dB, the step size is approximately 0.4 dB. This may suffice for coarse coverage prediction but is inadequate for sub-dB precision [5]. More critically, coarse 1 m resolution is ill-conditioned for coherent systems at centimeter wavelengths. A single 1 m voxel spans multiple coherence intervals, aliasing phase information governing constructive and destructive interference. Such datasets are invalid for phase-sensitive MIMO modeling but acceptable for scalar RSS prediction [86]. Practitioners working on coherent channels should adopt sub-wavelength resolution or continuous representations such as NeRF² [51].

3) *Physical Deficiencies in Ray Tracing*: Ray tracing is a geometric optical approximation valid in the asymptotic limit [16]. It breaks down when scatterer dimensions approach the carrier wavelength, where full-wave diffraction dominates [66]. Applying statistical models to single-input single-output (SISO) results to approximate MIMO matrices lacks electromagnetic rigor [3]. The spatial correlation structure depends on scattering geometry rather than parametric models alone. Homogeneous material assumptions also ignore frequency-dispersive $\epsilon_r(f)$ and $\sigma(f)$ of real materials [107].

These limitations do not diminish the value of existing benchmarks for validating algorithms and ranking performance. However, they motivate next-generation infrastructures with calibrated measurements, higher precision, finer resolution, and frequency-dependent material models [4], [18].

V. LEARNING-BASED METHODS FOR SOURCE-AWARE RADIO MAPPING

This section reviews five neural architecture families for source-aware RM construction. Table VI provides a cross-architecture comparison to guide practitioners. No single architecture dominates across all dimensions [5], [13]. Each family occupies a distinct niche in the trade-off space among latency, data efficiency, spatial modeling, and output modality. Table VIII further catalogs reusable architectural modules that can be integrated into these families without fundamental redesign. Fig. 4 illustrates the architectural progression from local convolutional receptive fields to global generative inference.

A. CNN-Based Methods

CNN-based forward RM construction establishes an image-to-image translation paradigm [21], [22]. Complex propagation phenomena are abstracted into 2D spatial pixel mappings. Table VII summarizes representative CNN-based models. This subsection organizes the discussion around four recurring architectural challenges rather than individual models.

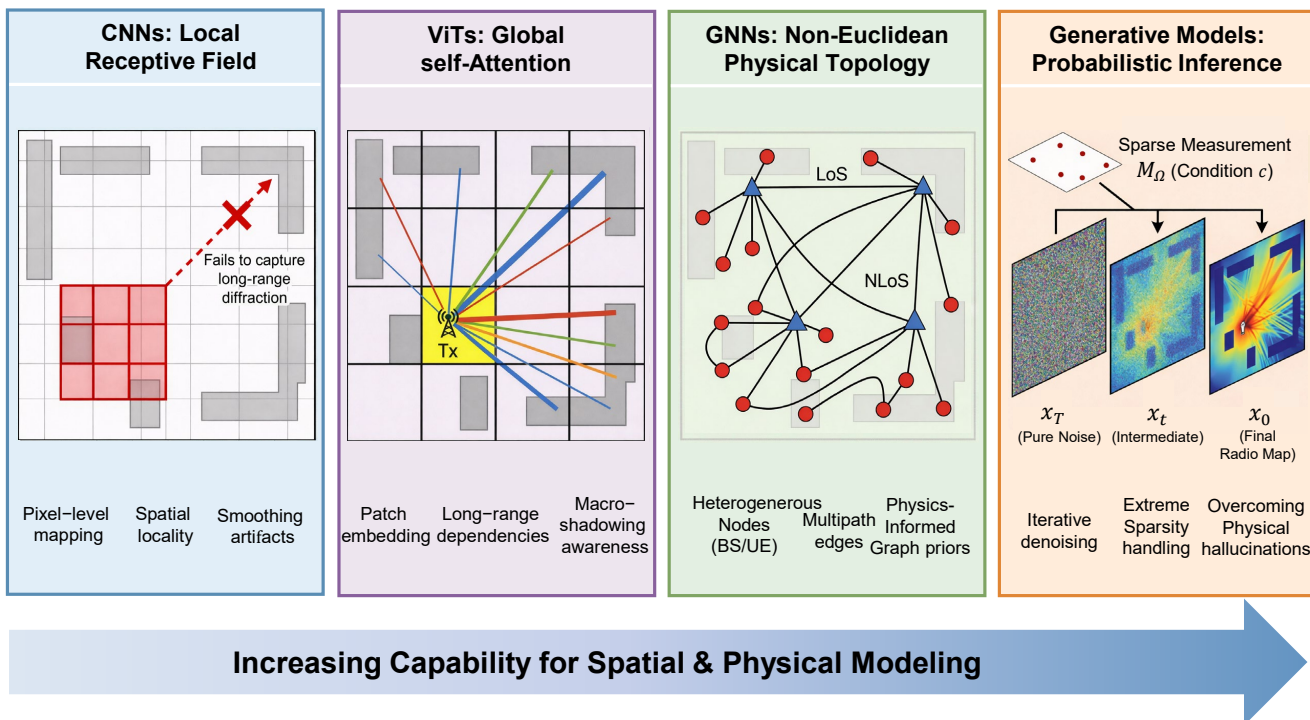


Fig. 4: The progression illustrates a paradigm shift towards increasing spatial and physical modeling capabilities. Early CNNs rely on local receptive fields but struggle with long-range diffraction. ViTs overcome this via global self-attention to capture macro-shadowing dependencies. GNNs embed physics-informed priors by modeling non-Euclidean multipath topologies. Recently, generative models reframe the task as probabilistic inference, enabling the reconstruction of high-fidelity radio maps from extreme sparsity. When combined with physics-informed constraints, these models can further mitigate physical hallucinations.

TABLE VI: Cross-architecture comparison for source-aware RM construction. “Sparse Input” indicates the native ability to handle spatially sparse measurements. Inference times are representative values on 256×256 maps with a single GPU.

Dimension	CNN	ViT	GNN	GAN	Diffusion (DDPM)	Diffusion (Turbo/Flow)	Best Suited Scenario
Output Type	Deterministic	Deterministic	Deterministic	Deterministic	Stochastic	Determ./Stochastic	—
Inference Latency	~ 5 ms	~ 10 –50 ms	~ 5 –20 ms	~ 5 –10 ms	~ 0.2 –19 s	~ 10 –63 ms	Real-time: CNN/GAN/Turbo
Memory (GPU)	< 1 GB	1–3 GB	< 1 GB	< 1 GB	1.5–3 GB	1.5–3 GB	Edge deploy: CNN/GNN
Training Data Need	High	Medium–High	Low–Medium	High (paired)	High	High	Data-scarce: GNN
Sparse Input	Poor	Strong	Strong	Medium	Strong	Strong	Sparse sensors: ViT/GNN
Uncertainty	\times	\times	\times	\times	Via MC sampling*	Via MC sampling*	UQ-critical: Diffusion
Physics Integration	Input-level	Input-level	Graph structure	Loss-level	Loss/Arch-level	Loss/Arch-level	Deep physics: GNN/Diffusion
Spatial Resolution	Grid-limited	Patch-limited	Flexible	Grid-limited	Grid-limited	Grid-limited	Continuous: GNN/NeRF

*Diffusion models produce stochastic samples; computing $\hat{\phi}_B \approx \frac{1}{J} \sum_{j=1}^J F(\gamma_j)$ yields unbiased estimates of nonlinear functionals; see Section V-E.

TABLE VII: Summary of representative CNN-based models for forward RM construction.

Model	Core Architecture	Input Modality & Dim.	Output Dim.	Test Dataset	Key Metric	Inf. Time
RadioUNet [21]	U-Net	$256 \times 256 \times 2$ (Map, Tx)	$256 \times 256 \times 1$	RadioMapSeer (DPM)	RMSE ≈ 1 dB (norm.)	5.6 ms
PPNet [124]	SegNet (regression)	$256 \times 256 \times 2$ (Height map, Tx)	$256 \times 256 \times 1$	RadioMapSeer (5.9 GHz)	RMSE: 0.0507 (norm.)	N/A
UNetDCN [6]	UNet + deformable conv.	$H \times W \times C$ (RGB, Dist, Angle)	$H \times W \times 1$	Aerial + nDSM	RMSE: 5.2–6.7 dB	N/A
PMNet [22]	ResNet + atrous conv. + SPP	$256 \times 256 \times 2$ (Bldg, Tx)	$256 \times 256 \times 1$	USC/Boston RT	RMSE $\sim 10^{-2}$ (gray)	N/A
SIP2Net [73]	U-Net + asym. conv. + ASPP	$256 \times 256 \times 5$ (multi-prior)	$256 \times 256 \times 1$	SPGC 2025 indoor	Wt. RMSE: 9.41 dB	N/A
R ² Net [75]	2D cascaded ResNet	$256 \times 256 \times 1$ (height enc.)	$256 \times 256 \times 16$	3DiRM3200 (3D)	RMSE: 0.040 (norm.)	N/A
RadioResUNet [74]	Cascaded ResUNet	$256 \times 256 \times 2$ (Layout, Tx)	$256 \times 256 \times 1$	2.4 GHz indoor RT	Error: 4.25–5.40 dB	N/A
Sat-Image PL [125]	Dual-branch (CNN+MLP)+SPP	$175 \times p \times 5$ (RGB, FSPL, Dist)	Scalar PL	5.9 GHz V2I (real)	RMSE: 5.05 dB	N/A
Geo2ComMap [126]	AG U-Net-TP	$H \times W \times 5$ (multi-metric)	$H \times W \times 1$	OSM+Sienna RT	Med. AE: 27.35 Mbps	N/A
LPCGMN [127]	Laplacian Pyramid + LRDC	High-res env. image	$H \times W \times 1$	DPM / DPMcars	NMSE: 0.0064	N/A
UAV Multimodal [128]	CNN + Transformer (parallel)	Image, Tx/Rx pos, freq.	Vectors (PL, DS, AoA)	AirSim + WinSite	PL R^2 : 0.997	N/A

1) *Encoder-Decoder Paradigm and Resolution Bottlenecks:* RadioUNet [21] introduced the U-Net encoder-decoder architecture to RM construction. It takes a two-channel input of the building map and transmitter position to predict path loss maps. RadioUNet also proposed transfer learning from coarse simulation to sparse measurements, reducing the need for large

empirical datasets [123].

A key tension in this paradigm is spatial resolution versus representational capacity. Pooling operations reduce resolution to increase the receptive field and extract abstract features [129]. However, downsampling discards fine-grained spatial information needed for shadow boundaries and diffraction

edges. Skip connections partially address this but cannot recover information destroyed by pooling itself.

PPNet [124] addresses this bottleneck through architectural design inherited from SegNet. The pooling layers store the indices of maximum activations during encoding and reuse them during decoding. This preserves fine-grained spatial information related to building geometry without additional parameters. A two-phase training strategy first learns binary building layouts, then fine-tunes with height-encoded inputs at a reduced learning rate. This curriculum stabilizes convergence and improves accuracy near building boundaries.

Tutorial takeaway: The encoder-decoder paradigm offers a reliable baseline for RM construction. When sharp shadow edges are critical, practitioners should preserve spatial indices as in PPNet [124] or use Laplacian pyramid decomposition as in LPCGMN [127].

2) *Receptive Field Expansion:* Standard 3×3 convolutions have a fixed receptive field that grows only linearly with depth. This locality is mismatched with wave propagation physics [21], [23]. A distant building can create a deep shadow zone hundreds of meters away. Capturing such long-range dependencies has motivated several innovations.

UNetDCN [6] integrates deformable convolutions that learn positional offsets for each sampling point. The receptive field expands non-uniformly to selectively attend to distant diffraction edges. A secondary capability is that the trained network can serve as a differentiable surrogate for antenna parameter optimization via backpropagation. However, gradient-based inversion through deep networks is susceptible to gradient explosion and local optima.

PMNet [22], [96] uses atrous convolutions and spatial pyramid pooling (SPP). Atrous convolutions increase the effective receptive field by inserting gaps between kernel elements [96]. The SPP module aggregates multi-scale features at the bottleneck. This captures building occlusion patterns at multiple spatial extents simultaneously. A transfer learning framework further enables generalization across city layouts.

SIP2Net [73] targets indoor scenarios with directional antennas. It combines asymmetric convolutions with atrous spatial pyramid pooling (ASPP) to reinforce linear wall edges [27]. A composite loss with a GAN adversarial term ensures both structural realism and numerical accuracy.

Tutorial takeaway: The receptive field should ideally span the longest dominant propagation path within the region of interest. Atrous convolutions provide a parameter-efficient expansion for regular grids [22]. Deformable convolutions are preferred when propagation-relevant structures have irregular spatial distributions [6].

3) *Dimensionality Reduction: Encoding 3D Physics in 2D Networks:* Full 3D volumetric convolutions incur substantial computational overhead [43]. Several methods encode 3D physics within 2D architectures through creative tensor design.

R²Net [75] maps obstacle heights to 2D pixel intensities via $v_{env} = (h_{env} + 0.1)/3.1$. Discrete receiver heights are mapped to output channels. The result is a $256 \times 256 \times 1$ input and a $256 \times 256 \times 16$ output, avoiding 3D convolutions entirely. RadioResUNet [74] uses a cascaded architecture with

height slicing. A combined Dice and binary cross-entropy loss preserves boundary conditions under strong shadowing.

For wide-area outdoor prediction with variable distances, a satellite-image-based model [125] uses an SPP layer to accept variable-sized inputs. Input dimensions are determined by the physical transmitter-receiver separation, achieving lossless alignment without image rescaling.

Tutorial takeaway: The essence of 3D-to-2D reduction is folding the vertical dimension into channels [74], [75]. This is effective when vertical variations are discrete and enumerable. It cannot capture continuous vertical interactions such as inter-floor wave guiding.

4) *Multi-Modal Fusion and Physical Prior Integration:* Multi-modal fusion of diverse input modalities enables more explainable models [73], [126].

Geo2ComMap [126] extends CNN capabilities to multi-metric throughput evaluation. It integrates attention gate mechanisms with geographic databases, reducing anomalous errors at building edges. In UAV air-to-ground scenarios, a multimodal fusion network [128] processes visual images through a residual CNN in parallel with a Transformer branch. This captures global dependencies of time-series channel data and addresses channel uncertainty from rapid 3D movement. LPCGMN [127] adopts a Laplacian pyramid reconstruction network. It retains residual information during downsampling and reconstructs the channel knowledge map as an image inpainting task.

Tutorial takeaway: Including physics-derived features such as FSPL maps, distance fields, and antenna gain projections as input channels consistently reduces learning difficulty [58], [73]. However, each feature channel adds preprocessing cost and may introduce its own approximation errors. This motivates the physics-informed approaches discussed in Section VIII.

B. ViT-Based Methods

To overcome the locality of convolutional receptive fields, the RM community has adopted ViT architectures [23], [26], [29]. Table IX summarizes representative methods.

RMTransformer [23] integrates a multi-scale MaxViT encoder with a convolutional decoder. Block attention captures localized boundary details, while grid attention models global structural dependencies. Multi-scale features are fused into the decoder via skip connections. On the USC dataset, RMTransformer achieves an RMSE of 0.0071, approximately 62% lower than RadioUNet [21] and 32% lower than PMNet [22].

When spatial observations are extremely sparse, the challenge intensifies. DAT-Unet [29] embeds deformable attention within a U-Net framework. It dynamically adjusts attention receptive fields by learning positional offsets. These offsets focus on structurally relevant regions such as building corners and known observation points. With only 50 sampling points, DAT-Unet reduces the RMSE by approximately 12% compared to RadioUNet [21].

Indoor propagation introduces further complexity. TransPathNet [130] uses a two-stage coarse-to-fine residual learning framework. A TransNeXt encoder predicts a coarse global map, which is then refined with physical priors in the second stage.

TABLE VIII: Plug-and-play architectural modules for RM construction. ‘‘Integration Point’’ indicates where the module is typically inserted. Gains are relative to the baseline without the module.

Module	Bottleneck Addressed	Integration Point	Representative Method	Reported Gain	Overhead
Deformable conv.	Fixed receptive field	Replace standard conv.	UNetDCN [6]	Distant diffraction capture	Moderate (~20% params)
Atrous conv.	Limited receptive field	Replace standard conv.	PMNet [22], SIP2Net [73]	Multi-scale shadowing	Negligible
SPP	Single-scale features	Bottleneck layer	PMNet [22]	Variable-size input	Negligible
Attention gate	Equal spatial weighting	Skip connections	Geo2ComMap [126]	Reduces edge errors	Small (<5% params)
Adaptive FFT	Smoothed high-freq. edges	U-Net decoder blocks	RadioDiff [41]	Sharp obstacle boundaries	Small
Laplacian pyramid	Detail loss in downsampling	Replace encoder-decoder	LPCGMN [127]	NMSE: 0.0064 (14.7%↓)	Negligible
Pooling index memory	Spatial info loss	Encoder pooling layers	PPNet [124]	Preserves edge resolution	Negligible
Cross-attention	Homogeneous conditions	Intermediate layers	RadioDiff [41]	Separate static/dynamic prompts	Moderate
adaLN	Scalar conditions	Normalization layers	[77]	Zero-shot beam generalization	Small
Rotary position emb.	No relative position info	Attention layers	[49]	Cross-BS spatial correlation	Negligible

TABLE IX: Summary of ViT-based methods for source-aware RM construction.

Model	Core Architecture	Input Dimensions	Output Dimensions	Test Dataset(s)	Key Metrics
RMTransformer [23]	MaxViT encoder + CNN decoder	$2 \times 256 \times 256$	$1 \times 256 \times 256$	USC dataset	RMSE: 0.0071
DAT-Unet [29]	Deformable attention + U-Net	$2 \times 256 \times 256$ (sparse pts)	$1 \times 256 \times 256$	RadioMapSeer, SpectrumNet	RMSE: 0.0183 (DPM, 50 pts)
TransPathNet [130]	TransNeXt + EMCAD decoder	$C \times 384 \times 384$ (multi-prior)	$1 \times 384 \times 384$	ICASSP 2025 challenge	RMSE: 10.397 dB
DINOv2-ViT [121]	Pre-trained DINOv2 + UPerNet	$C \times 518 \times 518$ (multi-prior)	$1 \times 518 \times 518$	ICASSP 2025 challenge	Wt. RMSE: 12.6 dB
OSSN [85]	ViT + pyramid decoder	Building map + prompt	$1 \times H \times W$	RadioMapSeer	Point ASCE: 0.0326
TxSTrans [28]	ViT + ResNet + IFPN	$256 \times 256 \times 1$ + prompt	$256 \times 256 \times 1$	RadioMapSeer/3DSeer	Sparse RMSE: 0.0508
UniRM [80]	UNet + self-attention + prompts	Sparse obs + 3D map + $f + h$	$W \times L$ (dense map)	Multi-scenario custom	RMSE: 3.42–13.68

DINOv2-ViT [121] leverages large-scale foundation model pre-training for cross-condition generalization. It employs a DINOv2 vision transformer as the encoder and a UPerNet convolutional decoder for reconstruction. The massive self-supervised pre-training of DINOv2 provides rich embeddings learned from diverse visual structures. Cross-condition evaluation across unseen buildings, frequencies, and antenna configurations demonstrates the robustness of this transfer learning approach.

RM construction ultimately serves downstream deployment tasks. OSSN [85] unifies RM estimation and base station site selection into an end-to-end Transformer framework. Cross-attention between building tokens and candidate location embeddings enables this unification. A recommendation module trained via knowledge distillation reduces site selection complexity from $O(NM)$ to $O(M)$ [85]. UniRM [80] presents a universal framework using memory-based prompt learning for multi-band, 3D RM construction [81].

Tutorial takeaway: ViTs offer the greatest advantage when inputs are spatially sparse and long-range blockage correlations exist [23], [26]. When inputs are dense and the environment is locally governed, the performance gap narrows. The foundation model paradigm represents a promising direction for cross-environment generalization [28].

C. GNN-Based Methods

GNNs are motivated by the non-Euclidean nature of radio propagation topology [31]–[33]. Spatial and spectral elements are represented as nodes, and their physical interactions as edges. This formulation naturally accommodates heterogeneous network entities and non-uniform sampling.

RadioGAT [31] addresses extreme spatial-spectral sparsity through a model-driven graph construction mechanism. It formulates a radio depth map that encodes obstruction proportions, distance fading, and frequency fading into a unified depth feature:

$$D_{b,n,m}^{(k)} = T_{b,n,m}(C - \alpha \log_{10} d_{b,n,m} - \beta \log_{10}(f_k)), \quad (26)$$

where b is the block index, n the grid index, and m the transmitter index. C absorbs frequency- and distance-independent terms, and $T_{b,n,m}$ is the non-building path proportion. A node-level masked training paradigm enables deployment under semi-supervised conditions without complete ground truth [31].

GNN-MDAR [131] addresses graph structural noise from propagation mechanism drifts across domains. It introduces a graph structure learner guided by a variational information bottleneck (VIB) objective:

$$Z = \arg \min_Z -I(F^C(Z), Y) + \beta I(Z, (X, A)), \quad (27)$$

where $F^C(Z)$ is the downstream regression prediction from the compressed representation Z . Y is the target RM label, and (X, A) are node features and the adjacency matrix. The first term maximizes predictive utility of Z . The second minimizes mutual information between Z and the raw graph structure, discarding domain-specific noise. The parameter β is gradually increased during training [131]. Starting with weak compression allows the model to first extract propagation-relevant features. Strong compression is applied only after useful structure has been stabilized.

WirelessNet [33] demonstrates that homogeneous graphs are inadequate for network-level modeling. It introduces a heterogeneous message passing framework with separate node types for user equipment and base stations. Distinct edge types represent communication and interference signals. The message function for edge type τ is:

$$m_j^\tau = x_{\tau,e^\tau} W^\tau \text{ReLU}(W_{pool}^\tau x_{BS,j} + b_{pool}^\tau). \quad (28)$$

Tutorial takeaway: GNNs are preferred when the propagation topology is non-Euclidean, when heterogeneous entity types must be modeled, or when sampling is non-uniform [31], [33]. Their main limitation is scalability: message passing over dense graphs with millions of nodes remains computationally challenging [32].

D. GAN-Based Methods

GANs reformulate RM construction as conditional generation [35], [37], [132]. They produce spatially coherent maps with sharp shadow boundaries that discriminative models often smooth away. Table X compares the principal GAN variants.

The standard conditional GAN objective maps incomplete condition u to a complete RM:

$$\min_G \max_D \mathbb{E}_{x \sim p_{\text{data}}} [\log D(x | u)] + \mathbb{E}_{z \sim p_z} [\log(1 - D(G(z | u)))] \quad (29)$$

1) *Paired Conditional Generation*: The baseline cGAN for television spectrum mapping [132] creates pseudo-ground-truth via Kriging interpolation. It uses a 16-layer U-Net generator with skip connections and a PatchGAN discriminator. RME-GAN [35] advances this with a two-phase strategy. The first phase uses a log-distance path loss model to produce a global template. A cosine similarity loss aligns the generator gradient with the physical template gradient:

$$L_{\text{Gradient}} = \sum_i \text{CS}(G(\tilde{y}(i)), G(z(i))). \quad (30)$$

The second phase applies geometry-wise downsampling and high-frequency Fourier constraints. The physical motivation is to reduce the adversarial search space [35]. Anchoring the generator to a physically plausible global field means the discriminator only evaluates local deviations.

FPTC-GANs [133] addresses temporal inconsistency between stable environments and real-time vehicular interference. An RMP-GAN predicts a base map from stable parameters. An RMC-GAN then applies real-time corrections guided by sparse measurements.

2) *Unpaired and Unconditional Generation*: CycleGAN [135] eliminates pixel-to-pixel correspondence using cycle-consistency and identity losses. Roger *et al.* [134] adapt this framework to V2X radio map reconstruction:

$$\mathcal{L}_{\text{cyc}}(G, F) = \mathbb{E}_x [\|F(G(x)) - x\|_1] + \mathbb{E}_y [\|G(F(y)) - y\|_1]. \quad (31)$$

RecuGAN [39] pushes further toward unconditional generation. It uses InfoGAN principles to synthesize coverage maps from noise and discrete latent codes with a Wasserstein objective and gradient penalty.

3) *Bridging to Physics-Aware Paradigms*: TiRE-GAN [36] bridges data-driven generation and physics-informed methods. It uses a radio depth map as a physics-embedded input channel. The generator objective includes a task-incentivized regularization term from a pre-trained outage detection network:

$$L = L_G + \alpha L_{\text{MSE}} + \beta L_R(z, \hat{z}), \quad (32)$$

where z and \hat{z} are downstream task network outputs. This feedback forces the generator to align shadowing boundaries with operational spectrum management requirements [36]. It foreshadows the deeper physics integration strategies surveyed in Section VIII.

E. Diffusion-Based Methods

Diffusion models establish a principled framework for capturing complex propagation distributions [41], [42], [63]. Table XI provides a summary organized by application tier.

1) *Foundational Methods and Sparse Scenarios*: RadioDiff [41] pioneers dynamic RM construction as a conditional generative task. It uses a decoupled diffusion model that separates forward noise into data attenuation and noise addition phases. The reverse process independently predicts drift and noise terms, reducing prediction variance and enhancing stability. An adaptive fast Fourier Transform (FFT) module captures high-frequency edge features from dynamic obstacles.

RM-Gen [44] models indoor path loss prediction as mask-agnostic image inpainting. RRDDM [136] handles sparse vehicle-trajectory measurements through a dual-head U-Net. It injects structural residuals and Gaussian noise simultaneously:

$$I_t = I_{t-1} + \alpha_t I^{\text{res}} + \beta_t \epsilon_{t-1}. \quad (33)$$

RadioTrace [137] relaxes the assumption of known transmitter locations entirely. It achieves joint RM generation and continuous transmitter coordinate estimation via a straight-through estimator and observation matching loss:

$$\mathcal{L} = \|\hat{\mathbf{x}}_0^t \odot \mathbf{M} - \mathbf{O}\|_F^2. \quad (34)$$

2) *Dimensional and Architectural Expansion*: CGDM [77] models ultra-grained channel fingerprint construction as image super-resolution, maximizing the evidence lower bound (ELBO) conditioned on coarse-grained data. BS-1-to-N [49] employs rotary position embedding and inter-CKM attention for cell-free network inference. RadioDiff-3D [43] transitions to fully 3D tensor generation using autoregressive height-wise generation. BeamCKMDiff [78] shifts to a diffusion Transformer backbone. Continuous beam vectors \mathbf{w} are injected via adaptive layer normalization for zero-shot generalization to unseen beam directions.

3) *Real-Time Acceleration*: Iterative denoising causes high inference latency, which is a bottleneck for real-time applications [19], [63]. Three acceleration paradigms form a trade-off chain.

RadioDiff-Turbo [19] applies structure-group parameter pruning and adjusts stochastic differential equation (SDE) integral bounds. This enables large sampling steps, reducing from 1000 to 10 steps. Inference latency reaches approximately 60 ms without network retraining.

RadioDiff-Flux [63] exploits the fact that temporally adjacent scenes share building topology. It bounds the Kullback-Leibler divergence between latent representations z_i and z_j at diffusion step t :

$$D_{KL}(p||q) = \frac{1}{2} \frac{(1-t)^2}{t} \|z_i - z_j\|^2. \quad (35)$$

Here z_i and z_j are variational autoencoder (VAE)-encoded latent states of two RMs sharing the same static environment. The scaling factor $(1-t)^2/t$ reveals an important structure. At large t near pure noise, it approaches zero, meaning latent distributions become indistinguishable. At small t near clean data, it diverges, reflecting maximum structural discriminability. This implies that early denoising steps recover shared

TABLE X: Comparison of GAN-based methods for RM construction. ‘‘Training Mode’’ indicates the data pairing requirement. Methods are ordered by relaxation of data requirements.

Method	Training Mode	Generator / Discriminator	Key Innovation	Phys. Prior	Best Suited Scenario
Baseline cGAN [132]	Paired (Kriging pseudo-GT)	16-layer U-Net / PatchGAN	Kriging bootstrap	✗	TV white space mapping
RME-GAN [35]	Paired	18-layer U-Net / 4-layer CNN	Physical template + micro-correction	✓	Non-uniform sampling
FPTC-GANs [133]	Paired	RMP-GAN + RMC-GAN (sequential)	First-predict-then-correct	✓	Dynamic vehicular interference
CycleGAN [134]	Unpaired	Dual ResNet-9 / PatchGAN	Cycle-consistency; no paired GT	✗	No paired GT available
RecuGAN [39]	Unconditional	InfoGAN + WGAN-GP	Noise → coverage; mutual info	✗	No data; mmWave beams
TIRE-GAN [36]	Paired + task-driven	ResNet gen. / PatchGAN disc.	Task-incentivized outage loss	✓	Spectrum management

TABLE XI: Summary of diffusion-based methods for RM construction.

Method	Target Problem	Core Methodology	Conditioning	Key Highlights
Foundation & Real-World Extreme Scenarios				
RadioDiff [41]	Dynamic RM	Decoupled DM; adaptive FFT in U-Net	Tx loc., obstacles	Isolates drift/noise; sharp edges
RM-Gen [44]	Indoor PL	Mask-agnostic inpainting	Sparse RSS (5%–15%)	No mask-specific retraining
RRDDM [136]	Vehicle trajectory RM	Dual-head U-Net; residual denoising	Trajectory RSS, PL prior	Structural residual + noise injection
RadioTrace [137]	Unknown Tx, restricted sampling	Straight-through estimator	Sparse RSS, building map	Training-free; joint Tx estimation
Dimensional & Network Expansion				
CGDM [77]	Ultra-grained channel fingerprint	Super-resolution; ELBO	Coarse-grained CF	4× SR; NMSE $\sim 10^{-4}$
BS-1-to-N [49]	Cross-BS CKM	Rotary PE; inter-CKM attention	Source BS CKM	Cell-free network inference
RadioDiff-3D [43]	3D volumetric RM	3D conv.; autoregressive height	3D map, Tx	PL + ToA + DoA output
BeamCKMDiff [78]	Beam-aware CKM	DiT; adaLN	Beam w, env.	Zero-shot continuous beam gen.
Real-Time Acceleration Paradigms				
RadioDiff-Turbo [19]	Latency bottleneck	SDE bound + pruning	Same as RadioDiff	1000→10 steps; 60 ms
RadioDiff-Flux [63]	Sequential scenes	Midpoint reuse; KL bound	Sequential env. matrices	3.5–58× speedup; <0.15% drop
RadioFlow [138]	Real-time RM	CNF; flow matching (ODE)	Static/dynamic context	NFE=1; 63 ms latency

building topology. Late steps refine scene-specific details such as transmitter location. Caching the intermediate state at a midpoint t^* bypasses redundant early-stage recovery [63]. This delivers 3.5–58× acceleration with less than 0.15% accuracy degradation.

RadioFlow [138] transitions from stochastic diffusion to continuous normalizing flows (CNF) via flow matching. It learns a deterministic vector field v_θ defined by an ordinary differential equation (ODE) $dx = v_\theta(t, x) dt$. Flow matching directly regresses the straight-line optimal transport velocity between noise and target data. This eliminates stochastic fluctuations during inference. Single-step generation is achieved with 63 ms latency and 8.3× parameter reduction.

4) *Probabilistic Output and Diffusion Priors*: A distinguishing feature of diffusion models is their ability to produce multiple stochastic samples from $p(\mathbf{M}|\mathbf{E}, \mathbf{S})$ [41], [92]. Generating J independent samples $\{\gamma_1, \dots, \gamma_J\}$ and computing Monte Carlo estimates:

$$\hat{\phi}_B \approx \frac{1}{J} \sum_{j=1}^J F(\gamma_j), \quad (36)$$

yields unbiased expectations of arbitrary nonlinear functionals F of the RM. This includes channel capacity and bit error rate. Such capability is unavailable from deterministic architectures that output a single point estimate [21], [22].

This stochastic sampling provides access to the aleatoric variability captured by the learned distribution. It does not constitute explicit epistemic uncertainty quantification over model parameters [92]. The practical benefit remains significant. When the RM serves as input to downstream decisions, Monte Carlo integration over samples provides more robust decisions than a single prediction [45]. As detailed in Section VI, pre-trained diffusion models also serve as powerful learned priors

for inverse reconstruction. The generative distribution provides regularization needed to resolve the ill-posedness of sparse-to-dense recovery [93], [139].

VI. LEARNING-BASED METHODS FOR SOURCE-AGNOSTIC RADIO MAPPING

Source-agnostic RM reconstruction is more challenging than forward prediction [24], [25]. The transmitter parameters are latent or unavailable. As the sampling rate decreases, the problem transitions from well-posed interpolation to a severely ill-posed inverse problem [26], [92]. Table XII provides a problem-driven decision guide organized by scenario characteristics.

A. CNN-Based Methods

CNNs provide the foundational framework for source-agnostic reconstruction, treating the task as sparse-to-dense spatial completion [24], [25]. Table XIII summarizes representative methods. The foundational masked reconstruction objective isolates the loss to observed indices Ω_t :

$$\min_w \frac{1}{T} \sum_{t=1}^T \|\mathbf{P}_{\Omega_t}(\tilde{\Psi}_t - p_w(\check{\Psi}_t))\|_F^2. \quad (37)$$

1) *Masked Completion Paradigm*: The earliest approaches use fully convolutional autoencoders with binary observation masks [24]. The mask distinguishes true low-power regions from unmeasured voids. Skip connections and dual-path routing prevent irreversible mixing of signal and environment channels during early convolutions [148]. DeepREM [25] pushes the sparsity limit to 5% with adversarial loss for distribution consistency. RobUNet [140] advances generalization to unseen building layouts through dual channel and pixel attention.

TABLE XII: Practitioner decision guide for source-agnostic RM reconstruction. As sparsity increases and prior knowledge diminishes, the paradigm transitions from deterministic completion to probabilistic generation.

Scenario	Sampling Rate	Tx Location	Env. Prior	Recommended Paradigm	Representative Methods
Dense grid, known Tx	>10%	Known	Building map	CNN masked completion	Masked AE [24], RobUNet [140]
Sparse random, known Tx	1–10%	Known	Building map	ViT / CNN+GAN	RadioFormer [26], DeepREM [25]
Ultra-sparse (<1%)	<1%	Known	Building map	ViT (equivariant) / Diffusion	STORM [141], [45]
Trajectory-based sparse	Sparse traj.	Known	Building map	Diffusion (residual)	RRDDM [136]
Unknown Tx, sparse obs.	1–10%	Unknown	Building map	Diffusion (joint Tx estimation)	RadioTrace [137]
No ground samples	0%	Known	Satellite imagery	GAN (satellite-driven)	SC-GAN [38]
Multi-band tensor	Sparse per-band	Known	Partial bands	CNN cross-band / Tensor	CF-CGN [95], ROASMP [142]
3D volumetric sparse	Sparse 3D	Known	3D model	Latent diffusion (PnP)	[143]
Quantized satellite obs.	Low-bit	Known	Coarse	Gradient-free diffusion	[139]

TABLE XIII: Summary of CNN-based methods for source-agnostic RM reconstruction.

Method	Core Architecture	Sparsity	Input Type	Key Innovation	Loss
<i>Masked Completion</i>					
Masked AE [24]	Conv. autoencoder	10–50%	Sparse grid	Binary mask for unmeasured voids	Masked Frobenius
DeepREM [25]	U-Net + Pix2Pix cGAN	$\geq 5\%$	Sparse random	Adversarial loss for distribution consistency	MSE + adversarial
RobUNet [140]	ResNet + dual attention	5–20%	Sparse grid (unseen layouts)	Channel & pixel attention for boundaries	MSE
<i>Vision Task Reformulation</i>					
SRResNet [144]	Super-resolution ResNet	$\sim 6\%$	Low-res grid	RM as super-resolution problem	Full-grid MSE
Template-Perturb. [145]	Exemplar inpainting	Large voids	Sparse + radio depth	Fill sequence follows Tx→Rx path	Physics-prioritized
CF-CGN [95]	Cycle-consistent GAN	Cross-band	Band $i \rightarrow j$	Variable-weight cycle-consistency	Cycle loss
<i>High-Dimensional Tensor Extension</i>					
CAED [76]	3D conv. autoencoder	1–95% 3D	3D voxel	Decoder dilation + structural pruning	3D Frobenius
Multitask SR [146]	Multi-channel SR	Variable	Multi-param. tensor	Homoscedastic uncertainty weighting	L_{MTL}
ROASMP [142]	CP decomp. + ADMM-RLS	Streaming 4D	Space×freq×time	Online robust tensor completion	ℓ_1 -reg. CP
<i>Practical Deployment</i>					
MoENet [122]	MoE + transfer learning	Data-scarce	Sparse + SimNet score	Uncertainty-aware expert fusion	Similarity-guided
NAS-REC [147]	Neural architecture search	Zero-shot	UAV outage data	No pre-training dataset required	Adaptive NAS

Tutorial takeaway: Masked completion works reliably at moderate sparsity above 5%. Its limitation is that the binary mask treats all unmeasured locations identically. There is no mechanism to distinguish geometrically predictable LoS voids from complex NLoS shadow zones.

2) *Vision Task Reformulation:* SRResNet [144] redefines RM reconstruction as super-resolution, recovering continuous maps from one-sixteenth sample density. The template-perturbation method [145] bridges exemplar-based inpainting with radio depth maps, aligning the filling sequence with transmitter-to-receiver signal paths. For cross-band extrapolation, CF-CGN [95] employs variable-weight cycle-consistent generative networks:

$$L_{cyc} = \mathbb{E}\|\Psi_{i,j}(\Psi_{j,i}(I_j)) - I_j\|_F^2 + \mathbb{E}\|\Psi_{j,i}(\Psi_{i,j}(I_i)) - I_i\|_F^2, \quad (38)$$

enforcing bijective cross-band mappings suitable for massive MIMO precoding.

3) *High-Dimensional Tensor Extension:* CAED [76] extends the baseline to a 3D Frobenius norm for voxel environments with decoder dilation and structural pruning. A multitask super-resolution framework [146] recovers path loss, delay spread, angular spread, and LoS status simultaneously. Homoscedastic uncertainty provides dynamic weight adaptation:

$$L_{MTL}(W, \sigma) = \sum_m \frac{L_m}{2\sigma_m^2} + \sum_m \log(\sigma_m). \quad (39)$$

ROASMP [142] formulates RM prediction as online robust 4D tensor completion spanning space, frequency, and time.

It uses temporal pre-filling with an attention-based forgetting factor, followed by CP decomposition with ℓ_1 -norm regularization to reject outliers. Online optimization via ADMM with recursive least squares enables dynamic tracking of low-rank subspaces across streaming measurements [142].

4) *Practical Deployment Challenges:* Real-world deployment introduces challenges beyond algorithms. A cross-AP inference paradigm [149] derives target access point RMs from neighboring AP maps via positional pre-convolution. MoENet [122] fuses transfer learning with uncertainty-aware mixture of experts using morphological features. NAS-REC [147] achieves zero-shot UAV outage map reconstruction without pre-training.

Tutorial takeaway: CNN-based inverse methods are the most mature and computationally efficient option, suitable for edge devices [24], [25]. Their limitation is the inability to produce diverse reconstructions or quantify uncertainty, which becomes critical below 5% sampling rates where the solution is non-unique.

B. ViT-Based Methods

ViTs offer a structural advantage for inverse problems: they natively process variable-sized sparse point sets as input tokens [26], [30]. CNNs must rasterize sparse measurements onto a dense grid, introducing zero-padding that wastes capacity [29].

The Transformer structure restoration (TSR) framework [150] employs alternating self-attention and axial attention modules. This reduces complexity from $O(n^2)$ to $O(n^{3/2})$. Standard L_2 loss averages multiple plausible patterns, yielding blurred reconstructions. TSR addresses this via a high-receptive

field (HRF) perceptual loss using a pre-trained segmentation network:

$$L_{hrf} = \mathbb{E} \left[(\phi_{hrf}(R) - \phi_{hrf}(\tilde{R}))^2 \right], \quad (40)$$

where ϕ_{hrf} is the structural feature extractor. The total loss balances accuracy with perceptual structure: $L_{\text{final}} = \lambda_{L2}L_2 + \lambda_{hrf}L_{hrf}$.

RadioFormer [26] decouples environmental priors from sparse observations through dual-stream self-attention. Building maps are processed as patch-level tokens. Sparse observations are encoded as pixel-level tokens by summing coordinate and value embeddings. The two streams interact via cross-stream cross-attention (CCA). Observation features F_O serve as queries, while building features F_B provide keys and values:

$$Q = W_Q F_O, \quad K = W_K F_B, \quad V = W_V F_B, \quad (41)$$

$$\text{CA}(Q, K, V) = \text{Softmax} \left(\frac{QK^\top}{\sqrt{d}} \right) V. \quad (42)$$

This reflects the physical intuition that each measurement queries surrounding geometry to infer local propagation [26].

STORM [141] defines the task as continuous point-set function regression, eliminating grid resolution bottlenecks. It processes variable-sized sample sets and embeds physical equivariance for translation and rotation. A weighted direction vector governed by the strongest signal measurements establishes a canonical pose:

$$v(r) = \sum_{n=1}^N \exp(\tilde{\gamma}_n)(r_n - r), \quad (43)$$

where $\tilde{\gamma}_n$ is the normalized RSS at the n -th location. Physical equivariance is hard-coded by aligning coordinates with this dominant propagation direction:

$$x_n = [\tilde{\gamma}_n, (U(r_n - r))^\top]^\top, \quad (44)$$

where U is the rotation matrix aligning with $v(r)$. If the entire environment and transmitter are translated or rotated, the RM transforms accordingly. By constructing features in a query-point-relative frame, STORM guarantees this equivariance structurally [141]. This eliminates the need for data augmentation to learn basic spatial symmetries. STORM extends to active sensing via causal self-attention for joint estimation and next-best-point selection.

Tutorial takeaway: ViTs offer the greatest advantage when measurements are extremely sparse and spatially irregular [26], [141]. Processing each measurement as an independent token avoids the information dilution of grid rasterization at sub-1% sampling rates. The STORM equivariance encoding is a broadly applicable design principle for any RM with translation or rotation symmetry.

C. GAN-Based Methods

Inverse GAN methods have shifted from point-by-point regression to cell-level global generation [37], [97]. The conditional GAN maps an environment x to an RSRP distribution y . Physical priors from empirical models are integrated through residual estimation: $y = S_{\text{true}} - \hat{S}_{\text{empirical}} \odot \text{Mask}$. This restricts the generator to learning high-frequency residual shadows [97].

ACT-GAN [37] extracts multi-scale contexts via aggregated contextual transformation blocks with varying dilation rates. Convolutional block attention modules enforce spatial attention on dense building edges. A composite loss synergizes MSE, perceptual, style, and adversarial terms [37].

SC-GAN [38] bypasses ground-level measurements by leveraging satellite imagery. The input is a dual-channel tensor of a building map and transmitter map. No intermediate RSS measurements are required. Commercial satellite imagery provides 0.3–1 m resolution, meeting typical RM grid requirements. However, satellite imagery lacks building height information, electromagnetic material properties, and temporal currency. These limitations confine SC-GAN to macroscopic coverage estimation where building footprint geometry dominates [38].

Tutorial takeaway: GAN-based inverse methods suit scenarios where paired ground truth is unavailable [38], [134]. Their limitation relative to diffusion models is mode collapse in deep shadow zones. The GAN may generate plausible but physically incorrect patterns with no uncertainty quantification.

D. Diffusion-Based Methods

Deterministic models output a single point estimate minimizing mean squared error [21], [22]. However, this is insufficient when downstream applications require nonlinear RM functionals [45], [92]. Consider an NLoS location where RSS fluctuates between -85 and -95 dBm. A deterministic model predicts -90 dBm. Channel capacity $C = B \log_2(1 + \text{SNR})$ is concave in linear-scale power. By Jensen's inequality, the point estimate systematically overestimates expected capacity [92]. This bias can reach several bits/s/Hz in low-SNR regimes. Diffusion models resolve this by generating J samples from $p(\gamma|\mathcal{M})$ and computing unbiased Monte Carlo estimates: $\hat{\phi}_B \approx \frac{1}{J} \sum_{j=1}^J F(\gamma_j)$ [45]. Fig. 5 visualizes the forward noising and reverse denoising processes in diffusion-based radio map reconstruction.

1) Bayesian Inverse Estimation and Learned Priors: RadioDiff-Inverse [93] frames reconstruction as Bayesian maximum a posteriori estimation $\hat{x}_{MAP} = \arg \max_x p(x)p(y|x)$. A pre-trained diffusion model provides the prior $p(x)$. The reverse generation is corrected via likelihood-weighted Monte Carlo sampling:

$$p_{\theta}^{\text{wgt}}(x_{t-1}^i | x_t, y_{t-1}) = \exp \left(-\frac{\|x_{t-1}^i - \mu_{\theta}\|^2}{2\sigma_t^2} + \frac{\|y_{t-1} - Ax_{t-1}^i\|^2}{2c_t^2\sigma_t^2} \right). \quad (45)$$

A notable property is training-free operation. It transfers a diffusion prior from natural images to the RF domain without wireless-specific fine-tuning [93]. Both domains share piecewise-smooth structures with sharp boundaries. Edge priors from natural images regularize shadow boundary reconstruction. However, three conditions degrade this transfer. First, RMs exhibit distance-dependent power decay with no natural image counterpart. Second, multipath fading patterns are physically meaningful but a natural image prior smooths them away. Third, the RM dynamic range exceeds 100 dB, far beyond 8-bit images. Natural image priors are effective for macro-scale shadowing but should not be relied upon for fine-grained

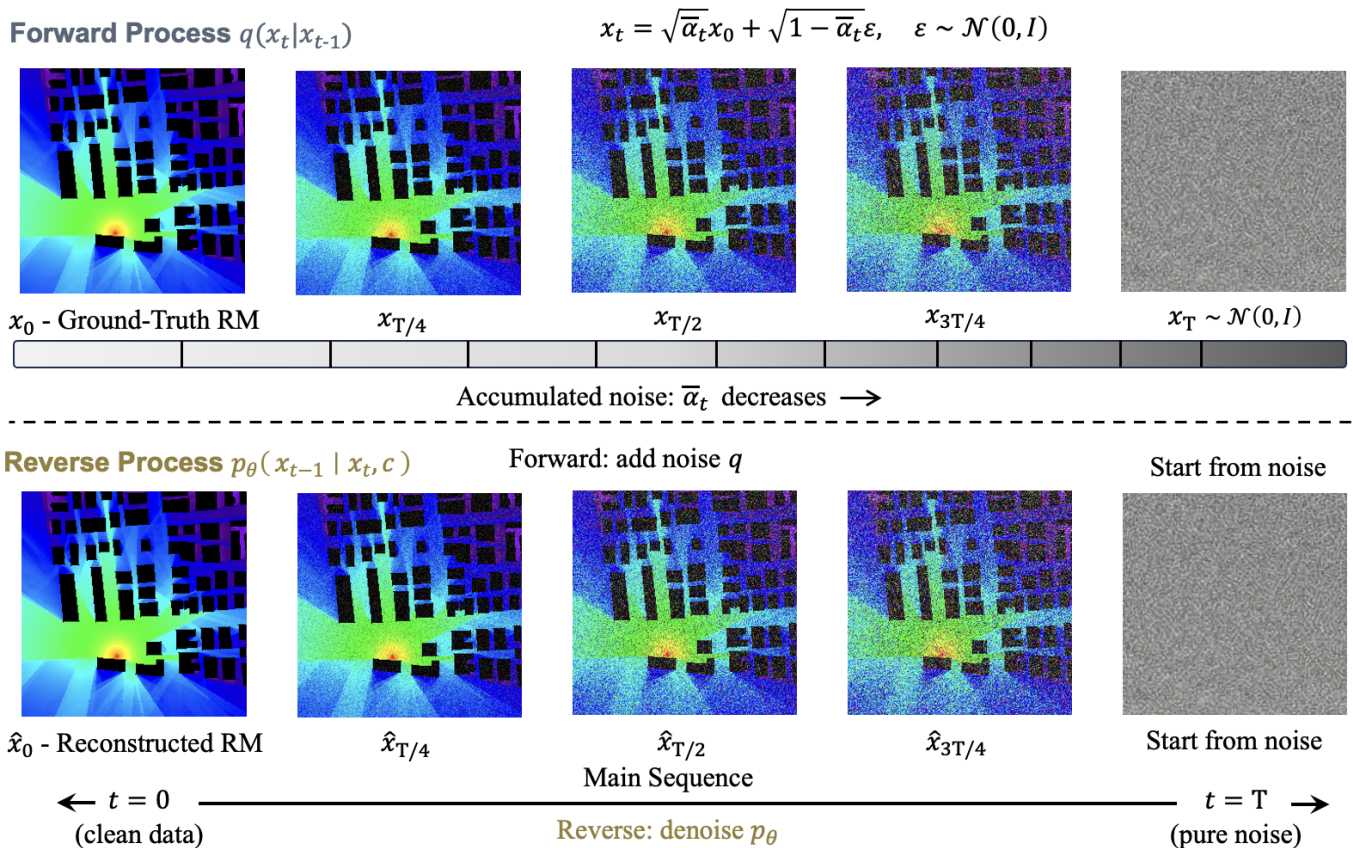


Fig. 5: Illustration of the forward noising process and the reverse denoising process in diffusion-based radio map reconstruction.

multipath recovery [92]. Domain-specific priors trained on wireless data are preferable for such cases.

2) *Architectural Adaptations for Blind Completion*: When environmental priors are absent, the conditional decoupled diffusion model [45] splits the forward process into image attenuation and noise enhancement. High-dimensional pixels are mapped to a condensed latent space via a variational autoencoder. Multi-scale conditions are extracted using a Swin-B Transformer. A dual-branch U-Net simultaneously predicts drift c_θ and noise ϵ_θ :

$$\min_{\theta} \mathbb{E}_{t, x_0, \epsilon, y} [\|c - c_\theta\|^2 + \|\epsilon - \epsilon_\theta\|^2]. \quad (46)$$

The latent-domain plug-and-play framework [143] addresses 3D spatio-spectral generation. It factorizes the dense tensor into spatial loss fields and power spectral density via $\mathcal{X} = \sum_{r=1}^R S_r \circ c_r$. Natural image denoisers are plugged into ADMM optimization within the reduced latent space to accelerate inference.

3) *Handling Extreme Observational Degradations*: For low-bit quantized satellite measurements with model $y = \mathcal{Q}(\mathbf{H}\mathbf{x} + \mathbf{n})$, the step-function quantizer has zero gradient almost everywhere [139]. Standard gradient-based likelihood guidance fails completely. A gradient-free closed-form posterior sampling replaces the quantized likelihood with a truncated Gaussian approximation [139]. Within each quantization bin $[l_i, u_i)$, the conditional distribution is modeled as a Gaussian truncated to that interval. Mean and variance are computed an-

alytically via the error function, yielding a closed-form update $\hat{x}_0^{post} = \hat{x}_0|_t + \frac{\gamma_t^2}{s} \mathbf{H}^T \Delta$ requiring no gradient computation.

4) *Physics-Informed Sensing and Localization*: RadioDiff-Loc [83] addresses NLoS source localization under extreme constraints without power calibration. It combines power-invariant normalization with multi-channel conditioning. A physics-informed sampling strategy inspired by knife-edge diffraction optimizes sensor placement [83]. Fisher information matrix analysis establishes that building vertices maximize mutual information, with $J_{jj} \propto 1/s_j^2$. This reduces the required sampling rate to under one percent while enabling sub-meter localization.

E. Summary and Practitioner Guidance

Table XIV reveals a clear stratification. CNN completion offers the lowest cost for moderate sparsity above 5% [24], [25]. ViT architectures achieve state-of-the-art performance at extreme sparsity by handling irregular point sets and encoding physical symmetries [26], [141]. GAN methods fill the niche of absent paired ground truth via satellite imagery or cycle-consistency [38], [134]. Diffusion models offer the broadest capability profile at the cost of higher latency [45], [92]. Acceleration paradigms from Section V-E are equally applicable here.

A unifying insight is that below the threshold where the inverse problem becomes non-unique, reconstruction must

TABLE XIV: Cross-architecture comparison for source-agnostic RM reconstruction. “Min. Sampling” is the lowest reported rate with reasonable quality.

Capability	CNN Completion	ViT	GAN	Diffusion
Min. sampling rate	~5% [25]	~0.01% [141]	~5%	~1% (trained); 0% (prior transfer) [93]
Unknown Tx handling	✗	Partial [30]	✗	✓ [137]
Probabilistic output	✗	✗	✗	✓ (MC sampling) [92]
Cross-band reconstruction	CF-CGN [95]	✗	✗	Latent PnP [143]
Real-time (<100 ms)	✓	✓	✓	Turbo/Flow only [19], [138]
3D volumetric support	CAED [76]	✗	✗	[43], [143]
Zero-shot (no wireless training)	✗	✗	✗	✓ [93]

transition from deterministic regression to probabilistic generation [92]. This is an information-theoretic necessity: when observations cannot uniquely determine the solution, the model must draw upon a learned prior. Reconstruction quality is then bounded by the fidelity of that prior [45], [60].

VII. OPTICS-INSPIRED ELECTROMAGNETIC MAPPING METHODS

The methods in Sections V and VI treat RM construction as image-level regression. This section reviews an alternative paradigm inspired by neural rendering [51]–[53], [119]. NeRF and 3DGS construct continuous, physics-grounded representations by explicitly modeling the volumetric propagation process. Table XV identifies when optics-inspired methods offer genuine advantages over traditional neural networks.

A. Neural Radiance Fields for RM Construction

Migrating optical NeRF to the RF domain presents significant physical challenges [51], [119]. Unlike visible light, RF signals interact with obstacles through absorption, reflection, diffraction, and scattering. RF signals are complex-valued, with phase governing constructive and destructive interference. RF hardware provides far lower spatial sampling than optical cameras. Table XVI establishes the mathematical mapping between optical and RF rendering domains.

1) *Foundational Voxelized Modeling*: NeRF² [51] discretizes 3D space into micro-voxels based on the Huygens-Fresnel principle. Each voxel is a secondary source characterized by complex attenuation δ and re-emitted signal S . The received signal from direction ω is:

$$R(\omega) = \int_0^D H_{P(r,\omega) \rightarrow P_{RX}} S(P(r,\omega), -\omega) dr, \quad (47)$$

where D is the propagation distance. The cumulative attenuation is $H = \exp(\int_0^r \delta d\hat{r})$, converting the product into a tractable summation in the logarithmic domain [51]. Dual complex-domain MLPs with positional encoding capture high-frequency spatial variations. A turbo-learning mechanism generates synthetic datasets from sparse real-world measurements [119].

2) *Physics-Embedded Neural Channel Synthesis*: Subsequent work embeds physical propagation rules into the rendering equation [151]. A key innovation decouples free-space propagation from object reflection. Reflection points are treated

as virtual transmitters, relieving the network from learning distance-based attenuation. The neural channel synthesis equation is:

$$H(\mathbf{f}) = \sum_{r \in \mathcal{L}} \sum_{p \in \mathcal{P}} w_{rp} A_{rp} e^{j(\psi_{rp} - 2\pi f d_p/c)}, \quad (48)$$

where r indexes multipath trajectories and p indexes sampled voxel points along each ray. w_{rp} is the volumetric density weight, A_{rp} the amplitude attenuation, and ψ_{rp} the phase shift [151].

A critical detail is phase prediction. The complex exponential $e^{j\psi}$ involves a non-differentiable modulo 2π operation. The model instead predicts in-phase and quadrature components: $I = A \cos \psi$ and $Q = A \sin \psi$. Both are smooth, continuous functions with well-defined gradients. Amplitude and phase are recovered post-hoc via $A = \sqrt{I^2 + Q^2}$ and $\psi = \arctan(Q/I)$. This I/Q decomposition is broadly applicable to any neural architecture in the complex RF domain [53], [151].

3) *Generalizable Wireless Radiance Fields*: The preceding frameworks rely on per-scene optimization. The generalizable wireless radiance field (GWRF) [152] addresses this by treating the target spatial spectrum as an interpolation of adjacent transmitters. A multi-head Transformer treats sampled voxels along a ray as tokenized sequences. Cross-attention learns cumulative attenuation weights driven by spatial geometry. Specialized attention heads hardcode low-level physical knowledge [152].

GWRF achieves zero-shot cross-scene generalization. In unseen environments, it achieves 26.9% MSE reduction and 10.2% PSNR improvement over NeRF² without retraining. GWRF-generated spatial spectra reduce AoA estimation errors by 61.6% compared to using only 50% of real data [152].

Tutorial takeaway: NeRF-based methods provide the highest fidelity for complex-valued channel reconstruction in a specific environment [51], [119]. MLP-based ray-marching incurs 200+ ms latency. They are best suited for offline digital twin construction. GWRF partially alleviates per-scene retraining but requires measurements from neighboring transmitters.

B. 3DGS-Based Methods

3DGS overcomes NeRF’s ray-marching latency through explicit anisotropic Gaussian primitives rendered via parallelizable rasterization [53]. Migrating optical 3DGS to the RF domain requires complex-domain representations and hemispherical antenna models rather than planar cameras.

TABLE XV: When to use optics-inspired methods versus traditional neural networks. The trade-off is between physical fidelity per scene and generalization across scenes.

Deployment Condition	Traditional NN	NeRF	3DGS	Rationale
Fixed env., variable Tx locations	✓	✗	✗	NeRF/3DGS require retraining per Tx
Fixed env., fixed Tx, max fidelity	✗	✓	✓	Scene optimization captures fine multipath
Real-time inference (<10 ms)	✓	✗	✓	3DGS: ~5 ms; NeRF: ~200 ms
Angle power spectrum needed	✗	✓	✓	3DGS outputs directional energy via splatting
Complex-valued CSI (amp. + phase)	Limited	✓	✓	Optics methods natively model complex fields
Generalization to unseen envs.	✓	✗*	✗	Per-scene optimization prevents transfer
Large-scale city (>1 km ²)	✓	✗	✗	Per-scene training is intractable at scale
Sparse measurements (<100)	✗	✓	✓	Physics-grounded rendering regularizes
Dynamic Tx and Rx (6D CKM)	✗	✗	✓ [†]	BiWGS supports X2X via bidirectional splatting

*GWRF achieves zero-shot cross-scene generalization; [†]BiWGS supports 6D but requires per-scene training.

TABLE XVI: Mapping of physical formulations: optical NeRF versus RF NeRF.

Attribute	Optical NeRF	RF NeRF [51]
Target domain	Visible light (real-valued intensity)	RF signals (complex-valued: amplitude & phase)
Radiated quantity	Color $\mathbf{c}(\mathbf{r}, \mathbf{d})$	Re-emitted signal $S(P(r, \omega), -\omega)$
Volumetric property	Volume density $\sigma(\mathbf{r})$	Complex attenuation $\delta(P) = \Delta\alpha e^{j\Delta\theta}$
Transmittance	$T(t) = \exp(-\int \sigma(s) ds)$	$H_{P \rightarrow P_{RX}} = \exp(\int \hat{\delta}(P) d\hat{r})$
Rendering integral	$C(\mathbf{r}) = \int T(t)\sigma(t)\mathbf{c}(t) dt$	$R(\omega) = \int_0^D H_{P \rightarrow P_{RX}} S(P, -\omega) dr$
Loss function	MSE on pixel colors	NMSE on complex signals

1) *Complex-Domain Gaussian Splatting*: WRF-GS [52] reinterprets 3D Gaussians as virtual transmitters. Optical color and opacity are replaced with signal strength and environmental attenuation. The multi-path received signal is:

$$y = \sum_{l=0}^{L-1} A \Delta A_l e^{j(\varphi + \Delta\varphi_l)}, \quad (49)$$

where ΔA_l and $\Delta\varphi_l$ are the amplitude and phase of the l -th path. A Mercator projection maps 3D space to a hemispherical sensing plane [52]. The Mercator distortion factor $1/\cos^2(\theta_{el})$ is negligible for terrestrial communications with $\theta_{el} < 30^\circ$. For UAV or satellite links with significant high-elevation energy, elevation-dependent compensation or alternative spherical projections should be used.

Optical alpha-blending is replaced by EM splatting following cascaded wave attenuation. WRF-GS+ introduces deformable Gaussians to decouple static large-scale fading from dynamic small-scale fading [153].

2) *MLP-Free Fourier-Legendre Synthesis*: GSRF [154] treats each 3D Gaussian as a secondary RF source via the Huygens-Fresnel principle. It replaces spherical harmonics with a Fourier-Legendre expansion (FLE):

$$\psi_k(\alpha, \beta) = \sum_{l=0}^L \sum_{m=-l}^l c_{ml}^{(k)} e^{im\alpha} P_l^m(\cos\beta), \quad (50)$$

which decouples azimuth and elevation with complex coefficients $c_{ml}^{(k)}$ encoding amplitude and phase. Combined with orthographic splatting and a frequency-domain consistency loss, GSRF operates entirely without MLPs [154].

3) *Complex Superposition via Inverse Source Formulation*: nGRF [64] formulates the problem as an electromagnetic inverse source problem governed by the Helmholtz equation. It

realizes distance- and direction-dependent attenuation via the Mahalanobis distance of anisotropic Gaussian bases. Crucially, nGRF identifies that optical alpha-blending is physically inadequate for RF [64]. Electromagnetic waves undergo coherent superposition rather than strict occlusion. The aggregate signal is an unordered complex summation:

$$H(p_{rx}, p_{tx}) = \sum_{i=1}^N w_i(p_{rx}) \cdot C_i, \quad (51)$$

where constructive and destructive interference emerge from the phase relations of $C_i = C_i^{re} + jC_i^{im}$. Unlike optical alpha-blending, the spatial weights w_i are deliberately not normalized. Energy conservation is maintained through covariance matrix scaling alongside complex superposition [64]. nGRF achieves 220 \times faster inference than NeRF baselines.

4) *6D Channel Knowledge Maps via Bidirectional Splatting*: BiWGS [65] extends to 6D channel knowledge maps (CKMs) for dynamic transmitter and receiver movement. It introduces bidirectional spherical harmonics (BSH) to fit complex scattering coefficients from multiple virtual projection planes.

BiWGS hard-codes electromagnetic reciprocity into the network structure [65]. Rather than soft loss penalties, it enforces strict symmetry through exact parameter sharing across reciprocal BSH coefficient index pairs. This guarantees $h_{A \rightarrow B} = h_{B \rightarrow A}$ by construction.

To balance optimization across paths spanning vastly different power levels, BiWGS transforms spatial spectra to logarithmic scale during loss computation [65]. In linear domain, LoS gradients exceed NLoS gradients by a factor of $\sqrt{R} \approx 10^5$ for a 100 dB range. After logarithmic transformation, the gradient becomes $\partial\mathcal{L}_{dB}/\partial P \propto 1/P$, inversely weighting by signal strength. This compresses the gradient dynamic range from \sqrt{R} to $\mathcal{O}(\log R)$, amplifying training signals from weak NLoS

paths. This log-domain strategy is broadly applicable to any RM model operating across large dynamic ranges.

C. Discussion

Table XVII summarizes the comparison. In terms of physical fidelity, NeRF and 3DGS demonstrate a substantial advantage [51], [53]. By replacing black-box pixel generation with wave propagation mechanics, 3DGS methods achieve significant SNR improvements in spatial spectrum prediction. 3DGS intrinsically captures angle power spectra through directional splatting, a capability traditional networks lack [53], [154].

The most critical bottleneck is the static environment assumption [64], [119]. Any change in environment or transmitter requires complete retraining. Even with optimization, 3DGS retraining takes tens of minutes and NeRF hours. Traditional networks encode the transmitter as an explicit input and generalize without retraining [21], [41].

Two future directions are promising. First, hybrid representations where a base model extracts environmental priors to dynamically condition Gaussian attributes in real-time. By decoupling static scatterers from dynamic objects, only a minimal Gaussian subset needs updating [153]. Second, amortized inference paradigms where a feed-forward encoder predicts 3D Gaussian parameters from sparse measurements in a single forward pass, reducing construction time from minutes to milliseconds [152].

Tutorial summary: Practitioners should select optics-inspired methods for high-fidelity digital twins of specific known environments, especially when complex-valued CSI or angular spectra are required [51], [53]. Traditional networks are preferred for cross-environment generalization, dynamic transmitter configurations, or real-time city-scale operation [21], [41]. Table XV provides a systematic reference.

VIII. PHYSICS-INFORMED METHODS FOR RM CONSTRUCTION

The methods in Sections V–VII are predominantly data-driven [21], [41], [51]. They learn the mapping from inputs to RMs by minimizing empirical loss on training data. No explicit mechanism enforces compliance with electromagnetic propagation laws. While effective when data is abundant and representative, purely data-driven models can violate physical principles in out-of-distribution regions [54], [55]. This section surveys physics-informed RM construction, which embeds electromagnetic knowledge into the data, loss function, or network architecture [42], [58], [59].

Table XVIII summarizes the three integration levels. Table XIX catalogs plug-and-play physics modules that practitioners can adopt without fundamental redesign.

A. A Taxonomy of Embeddable Physical Knowledge

Not all physical knowledge carries equal computational cost or utility for neural network integration [54]. This tutorial identifies three categories ordered by increasing physical depth.

1) *Geometric and Environmental Knowledge:* The most accessible category comprises knowledge from spatial geometry [21], [73]. This includes binary or height-encoded building maps, LoS/NLoS classification, fractional LoS ratios via 3D Bresenham algorithms, and edge and corner detectors. These features are inexpensive to extract from GIS or CAD data. They can be concatenated as additional input channels to any backbone. Their limitation is that they encode only the location of wave-obstacle interactions, not the electromagnetic response [79].

2) *Electromagnetic Propagation Knowledge:* The second category derives from Maxwell’s equations and their asymptotic approximations [55], [117]. This includes FSPL from the Friis equation, material-dependent reflection and transmission coefficients from Fresnel equations using ITU-R P.2040, diffraction losses from the uniform theory of diffraction (UTD), and projected antenna radiation patterns [79], [112]. These features encode quantitative electromagnetic responses. However, they require frequency-dependent parameters and may need per-pixel computation, incurring substantial preprocessing cost.

3) *Wave Equation and PDE-Level Knowledge:* The deepest category derives from governing partial differential equations (PDEs), principally the Helmholtz equation $\nabla^2 u + k^2 u = -f$ [42], [57]. Embedding this knowledge requires evaluating differential operators on the predicted field. This serves as either preprocessing features or loss-level constraints. This category provides the strongest physical regularization but is the most computationally demanding [55], [155].

Tutorial takeaway: The three categories are not mutually exclusive and can be combined hierarchically. A practical recipe is to begin with geometric features as baseline input channels. Add electromagnetic features such as FSPL and antenna gain for cross-frequency generalization. Incorporate PDE constraints only when strict physical consistency is required and sufficient computational budget is available.

B. Data-Level Integration: Electromagnetic Feature Engineering

Data-level integration transforms electromagnetic laws into physics-informed feature tensors concatenated with the network input [73], [79]. This approach is backbone-agnostic. The resulting tensors can be paired with any architecture without modifying the loss or topology. Since input design choices are discussed in Section III-B, this subsection focuses on the specific engineering techniques and their computational trade-offs.

1) *Material and Antenna Properties:* Multi-band operations require explicit electromagnetic feature fusion [79], [112]. Rather than feeding raw permittivity values, researchers compute physical reflectance and transmittance from ITU standards. Radio depth maps that physically anchor attenuation to building distributions are generated via logarithmic distance path loss and inverse distance weighting [31], [36]. The 3D antenna gain is projected onto the 2D propagation plane using trigonometric decomposition:

$$\text{FSPL} + G_{2D} = 20 \log_{10} \left(\frac{4\pi Df}{c} \right) + G(\Phi_{2D}, \Theta_{2D}). \quad (52)$$

TABLE XVII: Comparison of learning-based methods for RM construction. “Training” refers to per-scene optimization time.

Attribute	Traditional NN	NeRF-Based	3DGS-Based
Environment modeling	Requires explicit 3D geometry as input	Learns geometry from sparse measurements	Learns scatterer geometry; can use LiDAR init.
Response to Tx changes	Zero-shot via Tx input encoding	Retraining required (hours); GWRF partial	Retraining (tens of minutes); no zero-shot
Training time per scene	Seconds to hours	2–8 hours (MLP optimization)	10–60 minutes (explicit params)
Inference latency	CNN: ~5 ms; Diffusion: 60 ms–19 s	~200 ms (ray-marching)	~5 ms (rasterization)
Complex-valued support	Typically real-valued	Native via I/Q decomposition	Native via EM splatting
Spatial resolution	Grid-limited (1–10 m)	Continuous (arbitrary coords)	Continuous (arbitrary coords)
Scalability	City-scale feasible	Single building scale	Single building scale

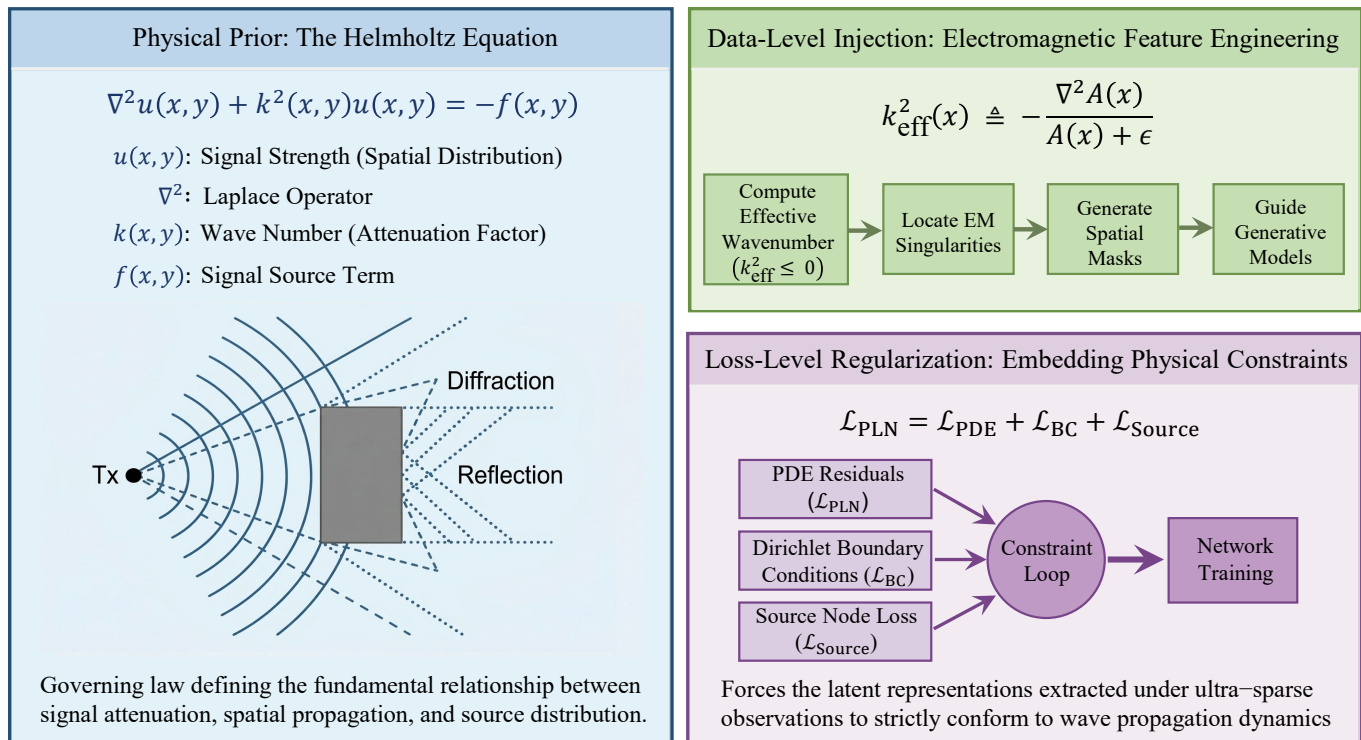


Fig. 6: The paradigm of physics-informed neural networks for radio map construction. The framework is fundamentally grounded in the Helmholtz equation, which governs electromagnetic wave propagation behaviors such as diffraction and reflection (left). Physical priors are integrated through a dual-driven mechanism: (top right) data-level injection via electromagnetic feature engineering, which utilizes the effective wavenumber (k_{eff}^2) to locate spatial singularities and guide generative models; and (bottom right) loss-level regularization, which embeds partial differential equation (PDE) residuals, Dirichlet boundary conditions, and source node losses into a joint constraint loop (\mathcal{L}_{PLN}) to force latent representations to strictly conform to physical wave dynamics.

TABLE XVIII: Comparison of physics-informed integration strategies for RM construction. Each level operates at a different pipeline stage with distinct computational trade-offs.

Integration Level	Core Mechanism	Primary Advantage	Key Bottleneck
Data level	Extraction of EM laws and topological features into input tensors	Cross-frequency and cross-antenna generalization without retraining	Offline preprocessing cost for 3D ray intersection
Loss level	Embedding PDEs and boundary conditions as penalty terms in training	Physical consistency under extreme sparsity	Gradient magnitude mismatch between physical and data losses
Architecture level	Mapping physical algorithms onto network topology via unrolling or routing	Deep structural alignment with wave propagation dynamics	High memory cost; risk of physical hallucinations

This projection is effective for fixed-downtilt antennas where elevation variance is small [112]. In active beamforming scenarios where the beam direction varies in 3D, this approximation discards volumetric radiation characteristics. Full 3D tensor representations become necessary, as discussed in Section III-B. Within its scope, this integration enables cross-frequency generalization without retraining [79].

2) *Geometric Occlusion Features*: For 3D building deployments, 3D Bresenham line generation computes the intersection ratio between transmitter-receiver paths and structures [156]. The resulting fractional LoS maps provide continuous occlusion features. This approach achieves a 13% accuracy improvement

over models without this physical prior [156]. Specialized terrain simulators extract cumulative knife-edge diffraction loss and 3D elevation angles for mountainous environments [157], [158].

3) *PDE-Derived Feature Maps*: In complex multipath environments, applying the Helmholtz equation directly as a loss function is unstable in non-physical latent spaces [42]. RadioDiff- k^2 [42] instead computes the effective wavenumber during preprocessing:

$$k_{\text{eff}}^2(\mathbf{x}) \triangleq -\frac{\nabla^2 A(\mathbf{x})}{A(\mathbf{x}) + \epsilon}, \quad (53)$$

TABLE XIX: Plug-and-play physics-informed modules for RM construction. ‘‘Backbone Agnostic’’ indicates applicability to any architecture without modification.

Module	Level	Physical Knowledge	Integration Method	Agnostic	Representative Method & Gain
FSPL + antenna gain channel	Data	Friis equation + 3D gain slice	Concat as input channel	✓	[79]: cross-freq. generalization
ITU material reflectance/transmittance	Data	Fresnel equations + ITU-R P.2040	Concat as input channel	✓	[73]: cross-material generalization
Fractional LoS map	Data	3D Bresenham ray-obstacle intersection	Concat as input channel	✓	[156]: 13% accuracy improvement
Radio depth map	Data	Distance fading + obstruction ratio	Concat as input channel	✓	TIRE-GAN [36], RadioGAT [31]
k_{eff}^2 singularity mask	Data	Helmholtz-derived amplitude curvature	Spatial mask for diffusion	✓	RadioDiff- k^2 [42]: 45.5% NMSE reduction
LoS path loss anchor	Loss	Free-space propagation law	Additive penalty term	✓	[56]: LoS power consistency
VIE/MoM residual	Loss	Volume integral equation + Green’s func.	Physical loss \mathcal{L}_{PHY}	Partial*	PEFNet [55]: $R^2 > 0.99$
Helmholtz PDE residual	Loss	$\nabla^2 u + k^2 u = -f$ discretized	\mathcal{L}_{PINN} penalty	Partial*	PhyRMDM [57]: 37.2% NMSE gain
ADMM unrolling	Arch.	Iterative optimization structure	Layer-by-layer mapping	✗	DULRTC-RME [143]: 25.81 dB PSNR
Geometric-optics cross-attention	Arch.	Transmission boundaries as prompts	Spatial cross-attention	✓ [†]	iRadioDiff [60]: RMSE 6.36 dB
Reciprocity parameter sharing	Arch.	EM reciprocity $h_{A \rightarrow B} = h_{B \rightarrow A}$	Hard weight symmetry	✗	BiWGS [65]: guaranteed reciprocity
Log-domain loss transform	Loss	Dynamic range compression	$\mathcal{L} = \ 10 \log_{10}(\hat{P}) - 10 \log_{10}(P)\ ^2$	✓	Gradient variance reduction [65]

*Requires precomputation of VIE/PDE matrices; [†]Requires diffusion backbone with cross-attention layers.

where A is the field amplitude from the RM. Physically, $k_{eff}^2 < 0$ localizes electromagnetic singularities such as deep fading dips and sharp shadowing boundaries [42]. These indicators are transformed into spatial masks that guide the diffusion process. This achieves a 45.5% NMSE reduction purely through improved conditioning of the diffusion prior.

4) *Topological Filtering for Dynamic Environments*: Dynamic environments with moving sources introduce multipath artifacts that corrupt the input feature space [100], [120]. Topological data analysis (TDA) distinguishes genuine sources from transient reflections via the concept of persistence. A genuine radiation source produces a broad peak that persists across a wide threshold range. A multipath artifact produces a narrow peak with low persistence. Formally, the 0-th persistent homology group assigns each local maximum a birth and death level. Peaks with persistence below a physical threshold are filtered as artifacts. The computational complexity is $O(n^2)$ to $O(n^3)$, where n is the grid point count. For a 256×256 grid, this can require several seconds on standard hardware.

5) *Reflection on Preprocessing Costs*: Explicit physical feature engineering improves generalization but shifts computation to offline preprocessing [79], [156]. Per-pixel 3D line-of-sight computation operates at $\mathcal{O}(P^3)$ complexity. For scenarios exceeding 256×256 grids, preprocessing can consume $10 \times$ – $100 \times$ the wall-clock time of inference [55]. For example, four-channel physics feature computation on 1024×1024 tensors requires approximately 27 seconds per scenario, compared to sub-second inference. These preprocessing pipelines constitute a bottleneck for real-time reconstruction.

Tutorial takeaway: Data-level integration is the most accessible entry point. It requires no modification to the network or loss. Start with FSPL and fractional LoS maps for low cost and high impact. Add material properties when cross-frequency generalization is needed [79]. Consider PDE-derived features such as k_{eff}^2 only for multipath-sensitive reconstruction [42].

C. Loss-Level Regularization: Embedding Physical Constraints

Loss-level integration translates electromagnetic principles into penalty terms [55], [57]. This constrains predictions to satisfy physical laws even where no measurements exist [54].

1) *Multipath Parameter Consistency*: Under sparse sampling, constraining multipath propagation logic provides essential

regularization [56]. The LoS path power is anchored to the theoretical free-space value:

$$PL(\text{dB}) = 20 \log_{10}(d) + 20 \log_{10}(f_c) + 20 \log_{10}\left(\frac{4\pi}{c}\right). \quad (54)$$

This requires prior knowledge of the transmitter location to compute distance d . In source-agnostic scenarios, this constraint is ill-posed [30]. Frameworks must either include an auxiliary localization module or relax the constraint into a relative spatial consistency loss. Additionally, a ReLU-based unidirectional penalty ensures NLoS path delays remain strictly greater than the theoretical LoS minimum [56].

2) *Numerical Solver Embedding*: PEFNet [55] directly embeds the volume integral equation (VIE) and its method of moments (MoM) discretization:

$$\mathcal{L}_{PHY} = \frac{1}{N} \|(I + W\chi)E^{tot} - E^{inc}\|, \quad (55)$$

where I is the identity matrix, W the Green’s function coefficient matrix, and χ the permittivity contrast matrix. The data loss becomes a residual compensation mechanism:

$$\mathcal{L}_{DAT} = \frac{1}{N} \|p^l - p^{dat}\|. \quad (56)$$

PEFNet achieves $R^2 > 0.99$ on RadioMapSeer with cross-scene generalization [55]. Inference latency is approximately 1.1 seconds, compared to hours for classical numerical solvers.

3) *Gradient Pathologies and Dynamic Balancing*: Combining physical and data losses introduces gradient pathologies [54], [55]. The physical loss \mathcal{L}_{PHY} operates on electric field residuals in V/m. The data loss \mathcal{L}_{DAT} operates on path loss in dB. Gradient norms frequently differ by two to three orders of magnitude. Uncalibrated, data-driven gradients overpower physics-based regularization.

Three balancing strategies have been applied successfully in RM construction. First, dynamic adjustment monitors the relative training rate of each loss component [146]. Components that train too fast are penalized, and those that lag are boosted. Second, homoscedastic uncertainty weighting treats each loss weight $1/(2\sigma_m^2)$ as a learnable parameter that adapts automatically [146]. Third, adaptive annealing gradually increases λ_{PHY} from zero over a warmup period of E_{warmup} epochs [57]. This allows the network to first learn the basic data distribution. Premature enforcement of strong constraints

disrupts early-stage feature learning.

Tutorial takeaway: When combining physical and data losses, never use a fixed weighting ratio without validation. Start with a warmup schedule where $\lambda_{PHY} = 0$ for the first 10–20% of training. Then transition to uncertainty-based weighting. Monitor the gradient norm ratio $\|\nabla \mathcal{L}_{PHY}\|/\|\nabla \mathcal{L}_{DAT}\|$ during training. If this ratio exceeds 100 or falls below 0.01, the balancing mechanism is failing.

4) *Helmholtz Equation Embedding:* PhyRMDM [57] operates a dual-network structure where the initial stage applies physical constraints via the 2D Helmholtz equation:

$$\nabla^2 u(x, y) + k^2(x, y)u(x, y) = -f(x, y), \quad (57)$$

where $u(x, y)$ is the radio signal strength, $k(x, y)$ the wavenumber, and $f(x, y)$ the source term. The continuous Laplacian is discretized using central differences [155]. As illustrated in Fig. 6, the physics-informed loss \mathcal{L}_{PLN} is decomposed into three complementary components that jointly form a constraint loop during network training:

$$\mathcal{L}_{PLN} = \mathcal{L}_{PDE} + \mathcal{L}_{BC} + \mathcal{L}_{Source}. \quad (58)$$

The first component \mathcal{L}_{PDE} penalizes violations of the Helmholtz equation across the entire spatial domain. It evaluates the PDE residual at every grid point by computing the discrete Laplacian of the predicted field \hat{u} and checking consistency with the local wavenumber and source term [54], [57]. This residual-based penalty constrains the predicted field to conform to wave propagation dynamics even in regions lacking measurement samples. The second component \mathcal{L}_{BC} enforces Dirichlet boundary conditions at the interfaces between free space and physical obstacles [57]. At building walls and structural boundaries, the electromagnetic field must satisfy material-dependent boundary constraints. By penalizing deviations from these boundary values, \mathcal{L}_{BC} ensures that the predicted field correctly reflects the attenuation and reflection behavior imposed by the environmental geometry [156]. The third component \mathcal{L}_{Source} constrains the predicted source term at the known transmitter location [57]. It anchors the radiation origin by penalizing discrepancies between the predicted field at the source node and the theoretical emission pattern. This prevents the network from generating physically plausible wave fields that originate from incorrect spatial locations. The three components address complementary physical aspects: \mathcal{L}_{PDE} governs wave propagation in free space, \mathcal{L}_{BC} governs wave-obstacle interaction at boundaries, and \mathcal{L}_{Source} governs the radiation origin. Together, they force the latent representations extracted under ultra-sparse observations to strictly conform to wave propagation dynamics [57]. This discretization introduces a truncation error of $\mathcal{O}(\Delta x^2)$ [159]. At 28 GHz with $\lambda \approx 10.7$ mm and grid resolution $\Delta x = 1$ m, the fourth derivative $\partial^4 u / \partial x^4$ scales as $(2\pi/\lambda)^4 \approx 1.19 \times 10^{11} \text{ m}^{-4}$. The resulting truncation error can exceed the actual path loss variation per cell. In practice, higher-order finite difference schemes or multi-scale refinements are needed [160]. Once properly discretized, the combined regularization \mathcal{L}_{PLN} yields a 37.2% NMSE improvement at 1–10% sampling rates over diffusion-only baselines [57].

D. Architecture-Level Mapping: Structural Isomorphism

Architecture-level integration establishes an isomorphism between network topology and the physical evolution process [59], [143]. This achieves the deepest structural alignment with electromagnetic dynamics.

1) *Algorithm Unrolling:* Algorithm unrolling maps classical iterative optimizers onto deep cascaded networks layer by layer [59], [143]. DULRTC-RME [143] formulates RM estimation as low-rank tensor completion:

$$\min_{\mathcal{X}, \mathcal{E}} \sum_{i=1}^3 \alpha_i \|\mathcal{X}_{(i)}\|_* + \lambda \|\mathcal{E}\|_1 + f(\mathcal{X}) + g(\mathcal{E}), \quad (59)$$

where $\alpha_1, \alpha_2, \alpha_3$ are learnable nuclear norm weights optimized via backpropagation. By unrolling ADMM, each forward propagation follows closed-form derivations with CNNs replacing proximal operators. This achieves 25.81 dB PSNR at 10% sampling [143]. RadioDUN [59] maps an alternating sparse recovery algorithm into a physics-inspired architecture. It achieves stable reconstruction from as few as 9 spatial measurements.

A practical constraint is memory footprint. With K unrolled blocks, DULRTC-RME stores $\mathcal{O}(K \cdot N^2)$ intermediate tensors during backpropagation. Empirically, $K = 6$ blocks on a 256×256 map consume approximately 24 GB of GPU memory [143].

2) *Differentiable Physical Components:* Hard physical occlusion logic disrupts backpropagation due to zero gradients. Non-linear activation functions construct soft indicator functions [109]. The formulation $I = 1 - \tanh(\text{POL})$ creates a continuous occlusion indicator, where $\text{POL} = \sum O_L$ is the cumulative intersection depth. Gradients flow seamlessly for environment reconstruction [109]. Complex diffraction scenarios, traditionally requiring recursive computation as in the Vogler model, have been replaced by multi-head attention with positional encoding [161].

3) *Physics-Informed Generative Architectures:* iRadioDiff [60] extracts transmission boundaries and signal discontinuity priors from geometrical optics. These are injected as physical prompts through spatial cross-attention to control the denoising trajectory. Removing these priors degrades RMSE from 6.36 to 9.62 dB, a 51% increase confirming the critical role of architecture-level physical embedding [60].

DeepRT [162] constructs a wireless environment knowledge pool based on ray-tracing principles. Reflection and diffraction priors are mapped into large model latent spaces through relation-aware modules. It achieves 4 ms inference latency, a speedup of approximately 3×10^5 over classical ray tracing [162]. It is important to note that the connection between language model sequence modeling and electromagnetic propagation remains an open research question. The success likely stems from the high-dimensional representational capacity and structured prior injection, rather than intrinsic alignment between linguistic and electromagnetic sequence structures.

4) *Physical Hallucinations: Definition and Detection:* A critical limitation of architecture-level methods in non-physical latent spaces is the inability to guarantee compliance with Maxwell’s equations [54], [55]. This introduces physical hallucinations, defined as follows.

TABLE XX: Quantitative comparison of representative physics-informed methods. Metrics are from the original publications on their respective benchmarks.

Method	Level	Physical Knowledge	Key Result	Preproc.	Inference	Backbone
[79]	Data	ITU reflectance + FSPL + antenna	Cross-freq. generalization	~27 s	<1 s	Any encoder-decoder
RadioDiff- k^2 [42]	Data	k_{eff}^2 singularity mask	45.5% NMSE reduction	Seconds	0.76 s	Diffusion model
[156]	Data	Fractional LoS map	13% accuracy gain	~14 ms	<14 ms	U-Net
PEFNet [55]	Loss	VIE/MoM residual	$R^2 > 0.99$	$\mathcal{O}(N^2)$	1.1 s	Any differentiable model
PhyRMDM [57]	Loss	Helmholtz PDE + BC + source	37.2% NMSE gain	None (online)	~1 s	Diffusion model
DULRTC-RME [143]	Arch.	ADMM unrolling	PSNR 25.81 dB at 10%	None	<1 s	Dedicated unrolled
DeepRT [162]	Arch.	MoE + RT knowledge pool	3×10^5 speedup vs. RT	Offline pool	4 ms	MoE backbone
iRadioDiff [60]	Arch.	Geometric-optics prompts	RMSE 6.36 dB	Feature extract.	~0.76 s	Diffusion + cross-att.
RadioDUN [59]	Arch.	ADMM + shadow prior	Stable from 9 measurements	None	<1 s	Dedicated unrolled

Definition (Physical Hallucination). A physical hallucination is a generated spatial field that structurally deviates from macroscopic electromagnetic laws. It is characterized by one or more violations: (i) energy conservation violation, where integrated local power exceeds the bound from source radiation and minimum path loss; (ii) reciprocity violation, where $|h_{A \rightarrow B} - h_{B \rightarrow A}|^2 > \epsilon$ exceeds a physical threshold [65]; (iii) boundary condition violation, where the predicted field fails to satisfy Dirichlet or Neumann conditions imposed by the geometry [57].

Detecting hallucinations requires post-generation physics verification, such as evaluating PDE residuals or checking energy conservation via spatial integration [42], [55]. Developing operationally useful detection metrics remains an important open challenge. It would transform physical consistency from an informal aspiration into a verifiable engineering guarantee.

Tutorial takeaway: Practitioners should pair architecture-level methods with lightweight post-hoc consistency checks. At minimum, verify that the total integrated power does not exceed the source power minus minimum path loss. For reciprocity-critical applications such as time-division duplex (TDD) systems, verify that the predicted channel satisfies $h_{A \rightarrow B} \approx h_{B \rightarrow A}$ at symmetric transceiver pairs.

E. Summary and Practitioner Guidance

The three levels represent complementary paradigms with distinct costs and capabilities. Table XX provides a structured quantitative comparison.

1) *Scenario-Specific Recommendations:* For offline network planning where several seconds of latency is acceptable, data-level integration is the pragmatic first choice [79], [156]. Physics-derived feature tensors can be paired with any backbone without modifying the training objective. Cross-frequency and cross-antenna gains are most pronounced when labeled target data is limited.

For sparse measurement reconstruction below 10% sampling rate, loss-level integration is recommended [55], [57]. PDE and multipath constraints confine the solution space to feasible electromagnetic manifolds. This is essential when data alone cannot determine a unique reconstruction. PEFNet requires knowledge of transmitter locations [55]. Source-agnostic settings require joint source position estimation.

For real-time digital twin synchronization below 100 ms latency, architecture-level integration with flow matching or

lightweight diffusion backbones is most appropriate [60], [162]. DeepRT’s MoE-based routing and iRadioDiff’s geometric-optics masks retain physical awareness at real-time latencies. The residual risk of physical hallucinations necessitates post-hoc consistency checks.

For severely data-constrained scenarios with fewer than 1,000 labeled samples, a combination of data-level and loss-level integration offers the best return [59]. RadioDUN achieves competitive reconstruction from 9 measurement points. Physics-derived priors effectively substitute for large labeled datasets.

2) *Open Challenges:* Three challenges define the frontier across all integration levels. First, online computation of data-level features must be made efficient for dynamic environment updates [42], [79]. Current offline preprocessing limits real-time applicability. Second, principled methods for automatic physical-data loss balancing are needed [54], [76]. Meta-learned weighting schedules or second-order gradient alignment could eliminate manual tuning. Third, operationally useful definitions and detection metrics for physical hallucinations are required [55]. The formal definition in Section VIII-D4 provides a starting point. Translating these criteria into lightweight differentiable verification layers remains an unsolved problem that would provide the rigorous foundation for next-generation physics-informed RM construction.

IX. OPEN ISSUES AND FUTURE DIRECTIONS

Learning-based RM construction has achieved significant milestones [5], [13]. However, the transition toward ubiquitous 6G environmental awareness remains constrained by several open challenges. These span two axes: modeling of uncharted propagation scenarios and algorithmic frontiers in inverse problems and physics-data co-design. This section identifies the most pressing issues, drawing upon the architectural insights, physical embedding strategies, and dataset limitations discussed throughout this tutorial. Fig. 7 organizes these challenges along three complementary axes.

A. Modeling Complex and Emerging Propagation Scenarios

1) *Beam-Aware RM Construction:* Current research predominantly addresses spatial field prediction for omnidirectional or fixed-beam antennas [21], [41]. Beam-aware modeling, where the RM is conditioned on a continuous beamforming vector $\mathbf{w} \in \mathbb{C}^{N_t}$, remains largely unexplored beyond BeamCKMDiff [78]. Two bottlenecks impede progress. First, beam-specific

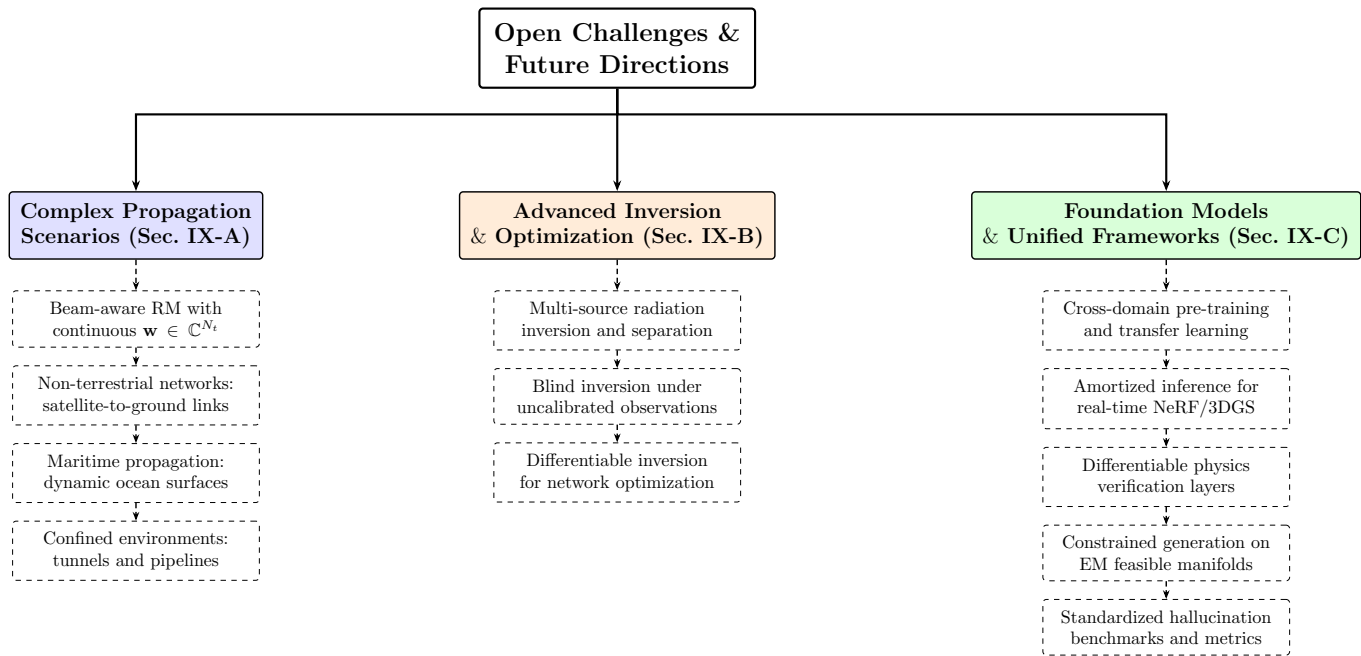


Fig. 7: Open research challenges and future directions for learning-based radio map construction, organized along three axes: complex propagation scenarios, advanced inversion and optimization, and foundation models with unified frameworks.

propagation datasets are scarce. BeamCKM [110] is currently the only public benchmark. Second, integrating continuous beam parameters increases the conditioning dimensionality. Architectures must decouple spatial geometry from high-dimensional beam sweeping [5]. The adaLN-based conditioning in Section III-B3 provides a template. Extending it to joint spatial-beam-frequency conditioning at scale remains open.

2) *Non-Terrestrial and Confined Environments*: Satellite-to-ground propagation is governed primarily by LoS conditions with dynamic atmospheric perturbations [163]–[165]. Models must translate macroscopic atmospheric statistics from satellite remote sensing into electromagnetic attenuation maps [166]. This requires multi-modal feature extraction capabilities with no close analogue in terrestrial RM literature. Maritime propagation presents challenges from ocean surface dynamics that continuously alter scattering geometries [167]. Tunnels and enclosed pipelines introduce extreme multipath from high-reflectivity metallic surfaces [168]. The variable effective propagation range in curved versus straight segments is incompatible with fixed-size tensor architectures. Adaptive-scale mechanisms such as dynamic sequence modeling or variable-resolution graph networks are needed [33].

B. Frontiers in Advanced Inversion and Optimization

1) *Multi-Source Radiation Inversion*: Existing source-agnostic frameworks are generally limited to a single radiation source [92], [141]. Multi-source environments introduce the challenge of disentangling overlapping spectral signatures from unknown emitters [89], [90]. The number of distinct configurations consistent with sparse observations grows exponentially with source count. No existing method provides theoretical identifiability guarantees. The Monte Carlo sampling capability

of diffusion models [45], [92] offers a natural tool to explore the multi-modal posterior distribution. Designing optimal sampling strategies and robust inversion algorithms for multi-source cartography remains a critical unsolved problem.

2) *Blind Parameter Inversion Under Uncalibrated Observations*: Real-world sensor data is corrupted by unknown noise floors, position drift, and device-specific antenna variations [8], [11], [104]. Developing unsupervised blind inversion frameworks that maintain fidelity despite uncalibrated observations is essential for autonomous network operation. The physics-informed loss strategies of Section VIII-C provide a starting point. However, their current formulations assume calibrated measurements [55], [57]. Extending them to jointly estimate noise model parameters alongside the RM remains open.

3) *Differentiable Inversion for Network Optimization*: A trained neural network acts as a differentiable surrogate model [6], [21]. Given a target coverage, gradients can be backpropagated to optimize base station parameters. However, as discussed in Section V-A2, this faces severe optimization pathology. Transmitter locations encoded as binary masks or Gaussian heatmaps produce fragmented gradients under naive descent [41]. Overcoming this requires novel differentiable rendering techniques, hybrid discrete-continuous solvers, or reinforcement learning formulations that bypass gradient pathology [9], [169].

C. Toward Foundation Models and Unified Frameworks

1) *Cross-Domain Pre-Training and Transfer*: The success of DINOv2-ViT [121] and RadioDiff-Inverse [93] in transferring visual priors to the wireless domain suggests cross-domain pre-training is viable [81], [122]. However, natural images differ from RMs in distance-dependent decay, dynamic range, and

multipath patterns [60]. Developing domain-specific foundation models pre-trained on large-scale wireless data is a more principled path [80]. The key question is whether a single model can span indoor offices, urban canyons, and maritime surfaces without catastrophic forgetting.

2) *Amortized Inference for Real-Time Optics-Inspired Methods*: Per-scene optimization in NeRF and 3DGS fundamentally limits applicability to dynamic environments [51], [53], [64]. Amortized inference would reduce RM construction from minutes to milliseconds. The goal is a feed-forward encoder \mathcal{E}_ϕ that directly predicts scene representation parameters from sparse measurements in a single forward pass. Concretely, for 3DGS-based methods, the encoder would map a sparse measurement set $\mathcal{M} = \{(\mathbf{r}_i, \mathbf{s}_i)\}_{i=1}^N$ to the full set of Gaussian parameters:

$$\{\boldsymbol{\mu}_k, \boldsymbol{\Sigma}_k, C_k^{re}, C_k^{im}\}_{k=1}^K = \mathcal{E}_\phi(\mathcal{M}), \quad (60)$$

where $\boldsymbol{\mu}_k$ and $\boldsymbol{\Sigma}_k$ are position and covariance of the k -th Gaussian, and $C_k^{re} + jC_k^{im}$ is its complex scattering coefficient. Training \mathcal{E}_ϕ requires a large dataset of scene-measurement pairs. This paradigm has shown success in optical 3DGS [152] but has not been explored in the RF domain. It represents a high-impact research opportunity for bridging the latency gap between optics-inspired fidelity and real-time deployment requirements.

3) *Closing the Physical Hallucination Gap*: The formal definition of physical hallucinations in Section VIII-D4 establishes a conceptual foundation [54], [55]. Operationally useful detection and mitigation strategies remain absent. Three research directions are identified. First, differentiable physics-verification layers that evaluate PDE residuals, energy conservation, and reciprocity during inference would enable real-time detection [42], [57]. Second, constrained generation mechanisms that project diffusion outputs onto the feasible electromagnetic manifold at each denoising step would provide generation-time guarantees [45], [92]. Third, standardized hallucination benchmarks, analogous to adversarial robustness benchmarks in computer vision, would enable systematic comparison across methods [4].

X. CONCLUDING REMARKS

This tutorial has systematically surveyed the data foundations, neural architectures, and physics-informed strategies for learning-based RM construction. We have established a unified taxonomy organized by the forward-inverse problem dichotomy and a three-level physics integration framework spanning data, loss, and architecture. The overarching lesson is clear: the progression from purely data-driven models toward physics-data dual-driven frameworks is a necessity dictated by the information-theoretic structure of the problem. When observations are sparse and propagation is complex, data alone cannot uniquely determine the RM. The model must draw upon physical priors to resolve ambiguity. The three levels of physics integration surveyed in Section VIII provide progressively deeper embedding of electromagnetic knowledge. Input-level feature engineering offers the lowest entry barrier. Loss-level PDE regularization constrains solutions to feasible

electromagnetic manifolds. Architecture-level structural isomorphism achieves the deepest alignment with wave propagation dynamics. Each level trades computational cost for physical fidelity. These advances collectively strengthen downstream tasks such as resource allocation, interference management, and predictive network planning. Several converging trends point toward the future of the field. Differentiable ray tracing enables joint simulation-optimization. Foundation model pre-training supports cross-environment generalization. Amortized inference can bring real-time rendering to optics-inspired methods. Formal hallucination detection provides deployment assurance. Together, these trends suggest a future where RM construction transitions from an offline, per-scenario engineering task to an always-on, physically rigorous component of the wireless network infrastructure. Achieving this vision requires sustained collaboration between the wireless communications, computational electromagnetics, and machine learning communities. The most powerful RM models will be those that respect the physics they seek to represent.

This tutorial has systematically surveyed the data foundations, neural architectures, and physics-informed strategies for learning-based radio map construction. We have established a unified taxonomy organized by the forward-inverse problem dichotomy and introduced a three-level physics integration framework spanning data, loss, and architecture. These advances collectively strengthen downstream tasks in wireless communication networks, including resource allocation, interference management, and predictive network planning, by enabling accurate and efficient radio environment digitization. The overarching lesson is that the progression from purely data-driven models toward physics-data dual-driven frameworks is a necessity dictated by the information-theoretic structure of the problem. When observations are sparse and propagation is complex, data alone cannot uniquely determine the radio map, and the model must draw upon physical priors to resolve ambiguity. Input-level feature engineering offers the lowest entry barrier, loss-level PDE regularization constrains solutions to feasible electromagnetic manifolds, and architecture-level structural isomorphism achieves the deepest alignment with wave propagation dynamics, where each level trades computational cost for physical fidelity. Looking ahead, several converging trends point toward a future where radio map construction transitions from an offline, per-scenario engineering task to an always-on, physically rigorous component of wireless network infrastructure: differentiable ray tracing enables joint simulation-optimization, foundation model pre-training supports cross-environment generalization, amortized inference brings real-time rendering to optics-inspired methods, and formal hallucination detection provides deployment assurance. Achieving this vision requires sustained collaboration between the wireless communications, computational electromagnetics, and machine learning communities, and the most powerful radio map models will ultimately be those that respect the physics they seek to represent.

REFERENCES

- [1] S. Dang, O. Amin, B. Shihada, and M.-S. Alouini, "What should 6g be?" *Nature Electronics*, vol. 3, no. 1, pp. 20–29, 2020.

- [2] N. Cheng, F. Chen, W. Chen, Z. Cheng, Q. Yang, C. Li, and X. Shen, "6G omni-scenario on-demand services provisioning: vision, technology and prospect(in chinese)," *Sci Sin Inform.*, vol. 54, pp. 1025–1054, 2024.
- [3] J. Chen, X. Yin, X. Cai, and S. Wang, "Measurement-based massive mimo channel modeling for outdoor los and nlos environments," *IEEE access*, vol. 5, pp. 2126–2140, 2017.
- [4] M. Boban and V. Degli-Esposti, "White paper on radio channel modeling and prediction to support future environment-aware wireless communication systems," *arXiv preprint arXiv:2309.17088*, 2023.
- [5] Y. Zeng, J. Chen, J. Xu, D. Wu, X. Xu, S. Jin, X. Gao, D. Gesbert, S. Cui, and R. Zhang, "A tutorial on environment-aware communications via channel knowledge map for 6g," *IEEE communications surveys & tutorials*, vol. 26, no. 3, pp. 1478–1519, 2024.
- [6] S. Jiang, Q. Qu, X. Pan, A. K. Agrawal, R. Newcombe, and A. Alkhatteeb, "Learnable wireless digital twins: Reconstructing electromagnetic field with neural representations," *IEEE Open Journal of the Communications Society*, vol. 6, pp. 1568–1590, 2025.
- [7] X. Shen, J. Gao, M. Li, C. Zhou, S. Hu, M. He, and W. Zhuang, "Toward immersive communications in 6g," *Frontiers in Computer Science*, vol. 4, p. 1068478, 2023.
- [8] Z. Becvar, J. Plachy, P. Mach, A. Nikolov, and D. Gesbert, "Machine learning for channel quality prediction: From concept to experimental validation," *IEEE Transactions on Wireless Communications*, vol. 23, no. 10, pp. 14 605–14 619, 2024.
- [9] Y. Okawa, N. Morita, J. Kakuta, and M. Ogawa, "Optimal base station sleep control via multi-agent reinforcement learning with data-driven radio environment map calibration," in *2024 IEEE 99th Vehicular Technology Conference (VTC2024-Spring)*. IEEE, 2024, pp. 1–6.
- [10] W. Guo and S. Wang, "Mobile crowd-sensing wireless activity with measured interference power," *IEEE wireless communications letters*, vol. 2, no. 5, pp. 539–542, 2013.
- [11] H. Sallouha, S. Sarkar, E. Krijestorac, and D. Cabric, "Rem-u-net: Deep learning based agile rem prediction with energy-efficient cell-free use case," *IEEE open journal of signal processing*, vol. 5, pp. 750–765, 2024.
- [12] H. Li, H. Wang, Z. Shen, and Y. Shi, "Intelligent reconstruction algorithm of electromagnetic map based on propagation model," *Journal of Communications and Networks*, vol. 26, no. 5, pp. 533–544, 2024.
- [13] M. Vasudevan and M. Yuksel, "Machine learning for radio propagation modeling: A comprehensive survey," *IEEE Open Journal of the Communications Society*, vol. 5, pp. 5123–5153, 2024.
- [14] R. Wahl, G. Wölfle, P. Wertz, P. Wildbolz, and F. Landstorfer, "Dominant path prediction model for urban scenarios," in *14th IST mobile and wireless communications summit*, 2005, pp. 1–5.
- [15] T. Rautiainen, G. Wolfle, and R. Hoppe, "Verifying path loss and delay spread predictions of a 3D ray tracing propagation model in urban environment," in *Proceedings IEEE 56th Vehicular Technology Conference*, vol. 4. IEEE, 2002, pp. 2470–2474.
- [16] G. Deschamps, "Ray techniques in electromagnetics," in *IEEE Proceedings*, vol. 60, no. 9, 1972, pp. 1022–1035.
- [17] J. Mladenović, A. Nešković, and N. Nešković, "An overview of propagation models based on deep learning techniques," *International Journal of Electrical Engineering and Computing*, vol. 6, no. 1, pp. 18–25, 2022.
- [18] J. Hoydis, F. Ait Aoudia, S. Cammerer, M. Nimier-David, N. Binder, G. Marcus, and A. Keller, "Sionna rt: Differentiable ray tracing for radio propagation modeling," in *2023 IEEE Globecom Workshops (GC Wkshps)*. IEEE, 2023, pp. 317–321.
- [19] X. Wang, P. Zheng, N. Cheng, R. Sun, J. Chen, K. Tao, Z. Yin, Z. Liu, and Y. Zeng, "Radiodiff-turbo: Lightweight generative large electromagnetic model for wireless digital twin construction," in *IEEE INFOCOM 2025 - IEEE Conference on Computer Communications Workshops (INFOCOM WKSHPS)*, 2025, pp. 1–6.
- [20] N. Sagir and Z. H. Tugcu, "Machine-learning-based path loss prediction for vehicle-to-vehicle communication in highway environments," *Applied Sciences*, vol. 14, no. 17, p. 7545, 2024.
- [21] R. Levie, Ç. Yapar, G. Kutyniok, and G. Caire, "Radiounet: Fast radio map estimation with convolutional neural networks," *IEEE Transactions on Wireless Communications*, vol. 20, no. 6, pp. 4001–4015, 2021.
- [22] J.-H. Lee, O. G. Serbetsci, D. P. Selvam, and A. F. Molisch, "Pmnet: Robust pathloss map prediction via supervised learning," in *GLOBECOM 2023-2023 IEEE Global Communications Conference*. IEEE, 2023, pp. 4601–4606.
- [23] Y. Li, C. Zhang, W. Wang, and Y. Huang, "Rmtransformer: Accurate radio map construction and coverage prediction," in *2025 IEEE 101st Vehicular Technology Conference (VTC2025-Spring)*. IEEE, 2025, pp. 1–5.
- [24] Y. Teganya and D. Romero, "Deep completion autoencoders for radio map estimation," *IEEE Transactions on Wireless Communications*, vol. 21, no. 3, pp. 1710–1724, 2021.
- [25] A. Chaves-Villota and C. A. Viteri-Mera, "Deeprem: Deep-learning-based radio environment map estimation from sparse measurements," *IEEE Access*, vol. 11, pp. 48 697–48 714, 2023.
- [26] Z. Fang, K. Liu, K. Chen, Q. Liu, J. Zhang, L. Song, and Y. Wang, "Radioformer: A multiple-granularity radio map estimation transformer with 1\textpertousand spatial sampling," *arXiv preprint arXiv:2504.19161*, 2025.
- [27] Y. Ansari, N. Tiyal, E. F. Flushing, and S. Razak, "Prediction of indoor wireless coverage from 3d floor plans using deep convolutional neural networks," in *LCN*, 2021, pp. 435–438.
- [28] C. Liao, Y. Zheng, J. Wang, and S. Liu, "Visual transformer based unified framework for radio map estimation and optimized site selection," *IEICE Transactions on Communications*, 2025.
- [29] K. Liu, C. Qiu, K. Chen, Q. Zheng, L. Song, and Y. Wang, "Paying deformable attention to sparse spatial observations for deep radio map estimation," *IEEE Trans. Cogn. Commun. Netw.*, 2025.
- [30] T. M. Hehn, T. Orekondy, O. Shental, A. Behboodi, J. Bucheli, A. Doshi, J. Nangoong, T. Yoo, A. Sampath, and J. B. Soriaga, "Transformer-based neural surrogate for link-level path loss prediction from variable-sized maps," in *GLOBECOM 2023-2023 IEEE Global Communications Conference*. IEEE, 2023, pp. 4804–4809.
- [31] X. Li, S. Zhang, H. Li, X. Li, L. Xu, H. Xu, H. Mei, G. Zhu, N. Qi, and M. Xiao, "Radiogat: A joint model-based and data-driven framework for multi-band radiomap reconstruction via graph attention networks," *IEEE Transactions on Wireless Communications*, vol. 23, no. 11, pp. 17 777–17 792, 2024.
- [32] G. Chen, Y. Liu, T. Zhang, J. Zhang, X. Guo, and J. Yang, "A graph neural network based radio map construction method for urban environment," *IEEE Communications Letters*, vol. 27, no. 5, pp. 1327–1331, 2023.
- [33] J. Perdomo, M. A. Gutierrez-Estevéz, C. Zhou, and J. F. Monserrat, "Wirelessnet: An efficient radio access network model based on heterogeneous graph neural networks," *IEEE Access*, 2025.
- [34] A. Shibli and T. Zanoua, "Data-driven radio environment map estimation using graph neural networks," in *2024 IEEE International Conference on Communications Workshops (ICC Workshops)*. IEEE, 2024, pp. 650–655.
- [35] S. Zhang, A. Wijesinghe, and Z. Ding, "Rme-gan: A learning framework for radio map estimation based on conditional generative adversarial network," *IEEE Internet of Things Journal*, vol. 10, no. 20, pp. 18 016–18 027, 2023.
- [36] Y. Zhou, A. Wijesinghe, Y. Ma, S. Zhang, and Z. Ding, "Tire-gan: Task-incentivized generative learning for radiomap estimation," *IEEE Wireless Communications Letters*, 2025.
- [37] Q. Chen, J. Yang, M. Huang, and Q. Zhou, "Act-gan: Radio map construction based on generative adversarial networks with act blocks," *IET communications*, vol. 18, no. 19, pp. 1541–1550, 2024.
- [38] Z. Pan, Z. Bangning, W. Heng, M. Wenfeng, and G. Daoxing, "Sc-gan: A spectrum cartography with satellite internet based on pix2pix generative adversarial network," *China Communications*, vol. 22, no. 2, pp. 47–61, 2025.
- [39] S. Sarkar, M. H. Manshaei, M. Krunz, and H. Ravaee, "Recugan: A novel generative ai approach for synthesizing rf coverage maps," in *2024 33rd International Conference on Computer Communications and Networks (ICCCN)*. IEEE, 2024, pp. 1–9.
- [40] Y. Ma, C. Zhang, C. He, and X. Li, "Radio map estimation using a cyclegan-based learning framework for 6g wireless communication," *Digital Communications and Networks*, 2025.
- [41] X. Wang, K. Tao, N. Cheng, Z. Yin, Z. Li, Y. Zhang, and X. Shen, "Radiodiff: An effective generative diffusion model for sampling-free dynamic radio map construction," *IEEE Transactions on Cognitive Communications and Networking*, vol. 11, no. 2, pp. 738–750, 2025.
- [42] X. Wang, Q. Zhang, N. Cheng, R. Sun, Z. Li, S. Cui, and X. Shen, "Radiodiff- k^2 : Helmholtz equation informed generative diffusion model for multi-path aware radio map construction," *IEEE Journal on Selected Areas in Communications*, 2025.
- [43] X. Wang, Q. Zhang, N. Cheng, J. Chen, Z. Zhang, Z. Li, S. Cui, and X. Shen, "Radiodiff-3d: A 3d \times 3d radio map dataset and generative diffusion based benchmark for 6g environment-aware communication," *IEEE Transactions on Network Science and Engineering*, 2025.
- [44] X. Luo, L. Zhizhen, Z. Peng, X. Dongkuan, and Y. Liu, "Rm-gen: Conditional diffusion model-based radio map generation for wireless networks," in *2024 IFIP Networking Conference (IFIP Networking)*. IEEE, 2024, pp. 543–548.

- [45] X. Luo, Z. Li, Z. Peng, M. Chen, and Y. Liu, "Denoising diffusion probabilistic model for radio map estimation in generative wireless networks," *IEEE Transactions on Cognitive Communications and Networking*, vol. 11, no. 2, pp. 751–763, 2025.
- [46] Z. Liu, S. Zhang, Q. Liu, H. Zhang, and L. Song, "Wifi-diffusion: Achieving fine-grained wifi radio map estimation with ultra-low sampling rate by diffusion models," *IEEE Journal on Selected Areas in Communications*, 2025.
- [47] S. Fu, Z. Wu, D. Wu, and Y. Zeng, "Generative ckm construction using partially observed data with diffusion model," in *2025 IEEE 101st Vehicular Technology Conference (VTC2025-Spring)*. IEEE, 2025, pp. 1–5.
- [48] L. Zhao, Z. Fei, X. Wang, J. Luo, and Z. Zheng, "3d-radiodiff: An altitude-conditioned diffusion model for 3d radio map construction," *IEEE Wireless Communications Letters*, 2025.
- [49] Z. Dai, D. Wu, Y. Zeng, X. Xu, X. Wang, and Z. Fei, "Bs-1-to-n: Diffusion-based environment-aware cross-bs channel knowledge map generation for cell-free networks," *arXiv preprint arXiv:2507.23236*, 2025.
- [50] J. Ho, A. Jain, and P. Abbeel, "Denoising diffusion probabilistic models," *Advances in neural information processing systems*, vol. 33, pp. 6840–6851, 2020.
- [51] X. Zhao, Z. An, Q. Pan, and L. Yang, "Nerf2: Neural radio-frequency radiance fields," in *Proceedings of the 29th Annual International Conference on Mobile Computing and Networking*, 2023, pp. 1–15.
- [52] C. Wen, J. Tong, Y. Hu, Z. Lin, and J. Zhang, "Wrf-gs: Wireless radiation field reconstruction with 3d gaussian splatting," in *IEEE INFOCOM 2025-IEEE Conference on Computer Communications*. IEEE, 2025, pp. 1–10.
- [53] L. Zhang, H. Sun, S. Berweger, C. Gentile, and R. Q. Hu, "Rf-3dgs: Wireless channel modeling with radio radiance field and 3d gaussian splatting," *IEEE Transactions on Wireless Communications*, vol. 25, pp. 10419–10433, 2026.
- [54] G. E. Karniadakis, I. G. Kevrekidis, L. Lu, P. Perdikaris, S. Wang, and L. Yang, "Physics-informed machine learning," *Nature Reviews Physics*, vol. 3, no. 6, pp. 422–440, 2021.
- [55] F. Jiang, T. Li, X. Lv, H. Rui, and D. Jin, "Physics-informed neural networks for path loss estimation by solving electromagnetic integral equations," *IEEE Transactions on Wireless Communications*, vol. 23, no. 10, pp. 15380–15393, 2024.
- [56] L. Liu, X. Chen, Z. Tang, M. Ma, and W. Zhang, "Pinn and gnn-based rf map construction for wireless communication systems," in *2025 International Conference on Future Communications and Networks (FCN)*. IEEE, 2025, pp. 1–6.
- [57] H. Jia, W. Chen, Z. Huang, H. Xiao, N. Jia, K. Wu, S. Lai, and Y. Yue, "Rndm: Radio map diffusion model with physics informed," in *Proceedings of the 33rd ACM International Conference on Multimedia (MM)'25*. Association for Computing Machinery, 2025.
- [58] X. Feng, J. Xiong, X. Liu, X. Zhang, H. Zhao, and J. Wei, "Physics-guided language model via low-rank adaptation for path loss prediction," *IEEE Transactions on Cognitive Communications and Networking*, 2025.
- [59] T. Chen, Z. Zhou, Z. Fang, W. Zou, K. Liu, K. Chen, Y. Zhang, and Y. Wang, "Radiodun: A physics-inspired deep unfolding network for radio map estimation," *arXiv preprint arXiv:2506.08418*, 2025.
- [60] X. Wang, T. Yuan, Y. Cao, N. Cheng, R. Sun, and W. Zhuang, "iradiodiff: Physics-informed diffusion model for indoor radio map construction and localization," in *ICC 2026 - IEEE International Conference on Communications*, 2026, pp. 1–6.
- [61] S. R. Doha and A. Abdelhadi, "Deep learning in wireless communication receivers: A survey," *Ieee Access*, vol. 13, pp. 113586–113605, 2025.
- [62] B. Feng, M. Zheng, W. Liang, and L. Zhang, "A recent survey on radio map estimation methods for wireless networks," *Electronics*, vol. 14, no. 8, p. 1564, 2025.
- [63] X. Wang, P. Zheng, H. Jia, N. Cheng, R. Sun, C. Zhou, and X. Shen, "Radiodiff-flux: Efficient radio map construction via generative denoise diffusion model trajectory midpoint reuse," *IEEE Transactions on Cognitive Communications and Networking*, vol. 12, pp. 4882–4895, 2025.
- [64] M. Umer, M. A. Mohsin, A. Bilal, and J. M. Cioffi, "Neural gaussian radio fields for channel estimation," *arXiv preprint arXiv:2508.11668*, 2025.
- [65] J. Zhou, C. Hu, G. Wu, Z. Ren, H. Hu, J. Zhang, R. Zhang, and J. Xu, "6d channel knowledge map construction via bidirectional wireless gaussian splatting," *arXiv preprint arXiv:2510.26166*, 2025.
- [66] A. Taflove, S. C. Hagness, and M. Picket-May, "Computational electromagnetics: the finite-difference time-domain method," *The Electrical Engineering Handbook*, vol. 3, no. 629–670, p. 15, 2005.
- [67] C. A. Balanis, *Antenna theory: analysis and design*. John Wiley & sons, 2016.
- [68] P. K. Diederik and W. Max, "An introduction to variational autoencoders," *Foundations and Trends® in Machine Learning*, vol. 12, no. 4, pp. 307–392, 2019.
- [69] Y. Song, J. Sohl-Dickstein, D. P. Kingma, A. Kumar, S. Ermon, and B. Poole, "Score-based generative modeling through stochastic differential equations," *arXiv preprint arXiv:2011.13456*, 2020.
- [70] B. D. Anderson, "Reverse-time diffusion equation models," *Stochastic Processes and their Applications*, vol. 12, no. 3, pp. 313–326, 1982.
- [71] P. Vincent, "A connection between score matching and denoising autoencoders," *Neural computation*, vol. 23, no. 7, pp. 1661–1674, 2011.
- [72] B. Mildenhall, P. P. Srinivasan, M. Tancik, J. T. Barron, R. Ramamoorthi, and R. Ng, "Nerf: Representing scenes as neural radiance fields for view synthesis," *Communications of the ACM*, vol. 65, no. 1, pp. 99–106, 2021.
- [73] W. Lu, Z. Lu, J. Yan, and S. Gao, "Sip2net: Situational-aware indoor pathloss-map prediction network for radio map generation," in *ICASSP 2025-2025 IEEE International Conference on Acoustics, Speech and Signal Processing (ICASSP)*. IEEE, 2025, pp. 1–2.
- [74] C.-W. Pyo, H. Sawada, and T. Matsumura, "Radioresunet: Wireless measurement by deep learning for indoor environments," in *2022 25th International Symposium on Wireless Personal Multimedia Communications (WPMC)*. IEEE, 2022, pp. 104–109.
- [75] C. Pyo, H. Sawada, and T. Matsumura, "A deep learning-based indoor radio estimation method driven by 2.4 ghz ray-tracing data," *IEEE Access*, vol. 11, pp. 138215–138228, 2023.
- [76] A. Ivanov, K. Tonchev, V. Poulkov, and A. Manolova, "Deep learning for reduced sampling spatial 3-d rem reconstruction," *IEEE Open Journal of the Communications Society*, vol. 5, pp. 2287–2301, 2024.
- [77] Z. Jin, L. You, X. Li, Z. Gao, Y. Liu, X.-G. Xia, and X. Gao, "Channel fingerprint construction for massive mimo: A deep conditional generative approach," *IEEE Transactions on Wireless Communications*, 2025.
- [78] L. Zhao, Y. Wang, X. Wang, Z. Fei, and Y. Zeng, "Beamckmdiff: Beam-aware channel knowledge map construction via diffusion transformer," *arXiv preprint arXiv:2601.10207*, 2026.
- [79] W. Chen and J. Chen, "Diffraction and scattering aware radio map and environment reconstruction using geometry model-assisted deep learning," *IEEE Transactions on Wireless Communications*, vol. 23, no. 12, pp. 19804–19819, 2024.
- [80] X. Jiang, T. Li, Z. Xiao, K. Chen, S. Ma, Z. Wang, and K. Li, "Unirm: A universal large model for multiband 3d radio map construction," *IEEE Journal on Selected Areas in Communications*, 2025.
- [81] R. K. Jaiswal, M. Elnourani, S. Deshmukh, and B. Bekerell-Lozano, "A data-driven transfer learning method for indoor radio map estimation," *IEEE Transactions on Vehicular Technology*, 2025.
- [82] B. Kerbl, G. Kopanas, T. Leimkühler, and G. Drettakis, "3d gaussian splatting for real-time radiance field rendering," *ACM Transactions on Graphics*, vol. 42, no. 4, pp. 1–14, 2023.
- [83] X. Wang, Q. Zhang, and N. Cheng, "Radiodiff-loc: Diffusion model enhanced scattering cognition for nlos localization with sparse radio map estimation," *arXiv preprint arXiv:2509.01875*, 2025.
- [84] P. Zhen, D. Guo, J. Hu, and H. Wang, "Radiation source localization using radio maps: A computer vision approach," *IEEE Wireless Communications Letters*, 2025.
- [85] Y. Zheng, C. Liao, J. Wang, and S. Liu, "A transformer-based network for unifying radio map estimation and optimized site selection," in *2024 IEEE International Conference on Acoustics, Speech, and Signal Processing Workshops (ICASSPW)*. IEEE, 2024, pp. 610–614.
- [86] Y. Qiu, X. Chen, K. Mao, X. Ye, H. Li, F. Ali, Y. Huang, and Q. Zhu, "Channel knowledge map construction based on a UAV-assisted channel measurement system," *Drones*, vol. 8, no. 5, p. 191, 2024.
- [87] X. Wang, L. Fu, N. Cheng, R. Sun, T. Luan, W. Quan, and K. Al-dubaikhy, "Joint flying relay location and routing optimization for 6g uav-iot networks: A graph neural network-based approach," *Remote Sensing*, vol. 14, no. 17, p. 4377, 2022.
- [88] S. Oh and N.-H. Myung, "MIMO channel estimation method using ray-tracing propagation model," *Electronics Lett.*, vol. 40, no. 21, p. 1, 2004.
- [89] B. Lim and M. Vu, "Interference analysis for coexistence of terrestrial networks with satellite services," *IEEE Transactions on Wireless Communications*, vol. 23, no. 4, pp. 3146–3161, 2023.

- [90] L. Zhao, Z. Fei, X. Wang, J. Huang, Y. Li, and Y. Zhang, "Imnet: Interference-aware channel knowledge map construction and localization," *IEEE Wireless Communications Letters*, vol. 14, no. 3, pp. 856–860, 2025.
- [91] C. You, B. Zheng, and R. Zhang, "Wireless communication via double irls: Channel estimation and passive beamforming designs," *IEEE Wireless Communications Letters*, vol. 10, no. 2, pp. 431–435, 2020.
- [92] T. N. Ha and D. Romero, "Bayesian radio map estimation: Fundamentals and implementation via diffusion models," *arXiv preprint arXiv:2508.06037*, 2025.
- [93] X. Wang, Z. Fang, N. Cheng, R. Sun, Z. Li *et al.*, "Radiodiff-inverse: Diffusion enhanced bayesian inverse estimation for isac radio map construction," *arXiv preprint arXiv:2504.14298*, 2025.
- [94] A. M. Sayeed, "Deconstructing multiantenna fading channels," *IEEE Transactions on Signal processing*, vol. 50, no. 10, pp. 2563–2579, 2002.
- [95] C. Xie, L. You, Z. Jin, J. Tang, X. Gao, and X.-G. Xia, "Cf-cgn: Channel fingerprints extrapolation for multi-band massive mimo transmission based on cycle-consistent generative networks," *IEEE Journal on Selected Areas in Communications*, 2025.
- [96] J.-H. Lee and A. F. Molisch, "A scalable and generalizable pathloss map prediction," *IEEE Transactions on Wireless Communications*, vol. 23, no. 11, pp. 17 793–17 806, 2024.
- [97] Y. Zheng, J. Wang, X. Li, J. Li, and S. Liu, "Cell-level rsrp estimation with the image-to-image wireless propagation model based on measured data," *IEEE Transactions on Cognitive Communications and Networking*, vol. 9, no. 6, pp. 1412–1423, 2023.
- [98] A. Goldsmith, *Wireless communications*. Cambridge university press, 2005.
- [99] B. Feng, M. Zheng, W. Liang, and L. Zhang, "Ipp-net: A generalizable deep neural network model for indoor pathloss radio map prediction," in *ICASSP 2025-2025 IEEE International Conference on Acoustics, Speech and Signal Processing (ICASSP)*. IEEE, 2025, pp. 1–2.
- [100] Q. Gao, Q. Zhu, Z. Lin, P. T. Mathiopoulos, Y. Zhao, Y. Huang, J. Wang, and Q. Wu, "Time-variant radio map reconstruction with optimized distributed sensors in dynamic spectrum environments," *IEEE Internet of Things Journal*, 2025.
- [101] E. Christopher, H. S. Dhillon, and R. M. Buehrer, "Characterizing the first-arriving multipath component in 5g millimeter wave networks: Toa, aoa, and non-line-of-sight bias," *IEEE Transactions on Wireless Communications*, vol. 21, no. 3, pp. 1602–1620, 2021.
- [102] W. C. Lee, "Estimate of local average power of a mobile radio signal," *IEEE Transactions on vehicular technology*, vol. 34, no. 1, pp. 22–27, 2006.
- [103] E. A. Lee and D. G. Messerschmitt, *Digital communication*. Springer Science & Business Media, 2012.
- [104] C. T. Cisse, V. Guillet, O. Baala, F. Spies, and A. Caminada, "Fine tuning an ai-based indoor radio propagation model with crowd-sourced data," in *2024 18th European Conference on Antennas and Propagation (EuCAP)*. IEEE, 2024, pp. 1–5.
- [105] P. Zeng and J. Chen, "Uav-aided joint radio map and 3d environment reconstruction using deep learning approaches," in *ICC 2022-IEEE International Conference on Communications*. IEEE, 2022, pp. 5341–5346.
- [106] C. E. Rasmussen, "Gaussian processes in machine learning," in *Summer school on machine learning*. Springer, 2003, pp. 63–71.
- [107] S. Bakirtzis, K. Qiu, J. Chen, H. Song, J. Zhang, and I. Wassell, "Rigorous indoor wireless communication system simulations with deep learning-based radio propagation models," *IEEE Journal on Multiscale and Multiphysics Computational Techniques*, vol. 10, pp. 58–68, 2024.
- [108] G. Wolffe and F. M. Landstorfer, "Dominant paths for the field strength prediction," in *VTC'98. 48th IEEE Vehicular Technology Conference. Pathway to Global Wireless Revolution (Cat. No. 98CH36151)*, vol. 1. IEEE, 1998, pp. 552–556.
- [109] S. Bakirtzis, M. Fiore, J. Zhang, and I. Wassell, "Solving maxwell's equations with non-trainable graph neural network message passing," *arXiv preprint arXiv:2405.00814*, 2024.
- [110] H. Wang, X. Shi, H. Zhang, Y. Cao, S. Yang, J. Wang, and K. Huang, "Beamckm: A framework of channel knowledge map construction for multi-antenna systems," *arXiv preprint arXiv:2511.18376*, 2025.
- [111] S. Bakirtzis, Ç. Yapar, K. Qui, I. Wassell, and J. Zhang, "Indoor radio map dataset," *IEEE Dataport*, 2024.
- [112] F. Jaensch, G. Caire, and B. Demir, "Radio map prediction from aerial images and application to coverage optimization," *IEEE Transactions on Wireless Communications*, 2025.
- [113] Ç. Yapar, F. Jaensch, R. Levie, G. Kutyniok, and G. Caire, "Overview of the first pathloss radio map prediction challenge," *IEEE Open Journal of Signal Processing*, vol. 5, pp. 948–963, 2024.
- [114] Y. Huangfu, J. Wang, S. Dai, R. Li, J. Wang, C. Huang, and Z. Zhang, "Wair-d: Wireless ai research dataset," *arXiv preprint arXiv:2212.02159*, 2022.
- [115] A. Alkhateeb, "Deepmimo: A generic deep learning dataset for millimeter wave and massive mimo applications," *arXiv preprint arXiv:1902.06435*, 2019.
- [116] Y. Zhao, Q. Zhu, Z. Lin, L. Guo, Q. Wu, J. Wang, and W. Zhong, "Temporal prediction for spectrum environment maps with moving radiation sources," *IET communications*, vol. 17, no. 5, pp. 538–548, 2023.
- [117] R. G. Kouyoumjian and P. H. Pathak, "A uniform geometrical theory of diffraction for an edge in a perfectly conducting surface," *Proceedings of the IEEE*, vol. 62, no. 11, pp. 1448–1461, 1974.
- [118] S. Bakirtzis, Ç. Yapar, K. Qiu, I. Wassell, and J. Zhang, "The first indoor pathloss radio map prediction challenge," in *ICASSP 2025-2025 IEEE International Conference on Acoustics, Speech and Signal Processing (ICASSP)*. IEEE, 2025, pp. 1–2.
- [119] E. Krijestorac and D. Cabric, "Deep learning based active spatial channel gain prediction using a swarm of unmanned aerial vehicles," *arXiv preprint arXiv:2310.04547*, 2023.
- [120] C. Zhao, R. Zhang, J. Wang, D. Niyato, G. Sun, H. Du, Z. Li, A. Jamalipour, and D. I. Kim, "Temporal spectrum cartography in low-altitude economy networks: A generative ai framework with multi-agent learning," *IEEE Transactions on Mobile Computing*, 2025.
- [121] R. Mkrtchyan, E. Ghukasyan, K. Petrosyan, H. Khachatryan, and T. P. Raptis, "Vision transformers for efficient indoor pathloss radio map prediction," *Electronics*, vol. 14, no. 10, p. 1905, 2025.
- [122] R. K. Jaiswal, M. Elnourani, S. Deshmukh, and B. Beferull-Lozano, "Leveraging transfer learning for radio map estimation via mixture of experts," *IEEE Transactions on Cognitive Communications and Networking*, 2025.
- [123] R. Levie, Ç. Yapar, G. Caire, and G. Kutyniok, "Fast radio propagation prediction with deep learning," in *Compressed Sensing in Information Processing*. Springer, 2022, pp. 301–335.
- [124] K. Qiu, S. Bakirtzis, H. Song, I. Wassell, and J. Zhang, "Deep learning-based path loss prediction for outdoor wireless communication systems," in *ICASSP 2023-2023 IEEE International Conference on Acoustics, Speech and Signal Processing (ICASSP)*. IEEE, 2023, pp. 1–2.
- [125] C. Wang, B. Ai, R. He, M. Yang, S. Zhou, L. Yu, Y. Zhang, Z. Qiu, Z. Zhong, and J. Fan, "Channel path loss prediction using satellite images: A deep learning approach," *IEEE Transactions on Machine Learning in Communications and Networking*, vol. 2, pp. 1357–1368, 2024.
- [126] F.-H. Lin, T.-H. Huang, C.-K. Wen, and T. Q. Duong, "Geo2commap: Deep learning-based mimo throughput prediction using geographic data," *IEEE Wireless Communications Letters*, 2025.
- [127] Z. Jin, L. You, J. Wang, X.-G. Xia, and X. Gao, "An i2i inpainting approach for efficient channel knowledge map construction," *IEEE Transactions on Wireless Communications*, vol. 24, no. 2, pp. 1415–1429, 2024.
- [128] R. Mkrtchyan, A. Manukyan, H. Khachatryan, and T. P. Raptis, "Fusion of pervasive rf data with spatial images via vision transformers for enhanced mapping in smart cities," *arXiv preprint arXiv:2508.03736*, 2025.
- [129] O. Ronneberger, P. Fischer, and T. Brox, "U-net: Convolutional networks for biomedical image segmentation," in *Medical Image Computing and Computer-Assisted Intervention-MICCAI 2015: 18th International Conference, Munich, Germany, October 5-9, 2015, Proceedings, Part III 18*. Springer, 2015, pp. 234–241.
- [130] X. Li, R. Liu, S. Xu, S. G. Razul, and C. Yuen, "Transpathnet: A novel two-stage framework for indoor radio map prediction," in *ICASSP 2025-2025 IEEE International Conference on Acoustics, Speech and Signal Processing (ICASSP)*. IEEE, 2025, pp. 1–2.
- [131] X. Wen, S. Fang, and Y. Fan, "Reconstruction of radio environment map based on multi-source domain adaptive of graph neural network for regression," *Sensors*, vol. 24, no. 8, p. 2523, 2024.
- [132] O. E. Dare, K. Okokpujie, E. Adetiba, O. Idowu-Bismark, A. Abayomi, R. J. Kala, E. Owolabi, and U. C. Ukpogon, "Development of a conditional generative adversarial network model for television spectrum radio environment mapping," *IEEE Access*, vol. 12, pp. 197 632–197 644, 2024.
- [133] Y. Wang, S. Sun, N. Liu, L. Xu, and L. Wang, "Two-stage radio map construction with real environments and sparse measurements," *IEEE Wireless Communications Letters*, vol. 14, no. 4, pp. 969–973, 2025.

- [134] S. Roger, M. Brambilla, B. C. Tedeschini, C. Botella-Mascarell, M. Cobos, and M. Nicoli, "Deep-learning-based radio map reconstruction for v2x communications," *IEEE Transactions on Vehicular Technology*, vol. 73, no. 3, pp. 3863–3871, 2023.
- [135] J.-Y. Zhu, T. Park, P. Isola, and A. A. Efros, "Unpaired image-to-image translation using cycle-consistent adversarial networks," in *Proceedings of the IEEE international conference on computer vision*, 2017, pp. 2223–2232.
- [136] Y. Zhang, H. Yu, T. Zhang, C. She, and F. Zheng, "Rrddm: A residual denoising diffusion-based method for high-precision radio map estimation," in *2025 IEEE 102nd Vehicular Technology Conference (VTC2025-Fall)*. IEEE, 2025, pp. 1–5.
- [137] L. Yang, Q. Li, Z. Cao, and J. Lin, "Radiotrace: Bridging diffusion priors and rss measurements for accurate radio map estimation," in *2025 IEEE 35th International Workshop on Machine Learning for Signal Processing (MLSP)*. IEEE, 2025, pp. 1–6.
- [138] H. Jia, W. Chen, X. Wang, N. Cheng, H. Zhang, K. Yu, S. Lai, N. Jia, B. Tian, H. Xiao *et al.*, "Radioflow: Efficient radio map construction framework with flow matching," *arXiv preprint arXiv:2510.09314*, 2025.
- [139] C. Xu, D. Tang, A. Seretis, and C. Sarris, "A diffusion-based propagation model for path loss prediction in indoor environments," in *2025 19th European Conference on Antennas and Propagation (EuCAP)*. IEEE, 2025, pp. 1–5.
- [140] S. Shao, K. Liu, Q. Liu, S. Zhang, K. Chen, and L. Song, "Robunet: A radio map construction method with a strong generalization capability," in *GLOBECOM 2024-2024 IEEE Global Communications Conference*. IEEE, 2024, pp. 2268–2274.
- [141] P. Q. Viet and D. Romero, "Spatial transformers for radio map estimation," in *ICC 2025-IEEE International Conference on Communications*. IEEE, 2025, pp. 6155–6160.
- [142] F. Zhou, C. Wang, G. Wu, Y. Wu, Q. Wu, and N. Al-Dhahir, "Accurate spectrum map construction for spectrum management through intelligent frequency-spatial reasoning," *IEEE Transactions on Communications*, vol. 71, no. 7, pp. 3932–3945, 2023.
- [143] Y. Wang, X. Wu, L. Xu, N. Liu, and L. Wang, "Dulrct-rme: A deep unrolled low-rank tensor completion network for radio map estimation," in *ICASSP 2025-2025 IEEE International Conference on Acoustics, Speech and Signal Processing (ICASSP)*. IEEE, 2025, pp. 1–5.
- [144] S. Wang, X. Xu, and Y. Zeng, "Deep learning-based ckm construction with image super-resolution," in *2025 IEEE 101st Vehicular Technology Conference (VTC2025-Spring)*. IEEE, 2025, pp. 1–5.
- [145] S. Zhang, T. Yu, B. Choi, F. Ouyang, and Z. Ding, "Radiomap inpainting for restricted areas based on propagation priority and depth map," *IEEE Transactions on Wireless Communications*, vol. 23, no. 8, pp. 9330–9344, 2024.
- [146] X. Wang, K. Guan, D. He, Z. Zhang, H. Zhang, J. Dou, and Z. Zhong, "Super-resolution of wireless channel characteristics: A multitask learning model," *IEEE Transactions on Antennas and Propagation*, vol. 71, no. 10, pp. 8197–8209, 2023.
- [147] Y. He, L. Wang, M. Shen, G. Huang, H. Huang, and H. Zhao, "Radio map reconstruction based on nas enhanced deep regularization completion for uav communications," in *2025 IEEE 101st Vehicular Technology Conference (VTC2025-Spring)*. IEEE, 2025, pp. 1–5.
- [148] S. K. Vankayala, S. Kumar, I. Roy, D. Thirumulanathan, S. Yoon, and I. S. Kanakaraj, "Radio map estimation using a generative adversarial network and related business aspects," in *2021 24th International Symposium on Wireless Personal Multimedia Communications (WPMC)*. IEEE, 2021, pp. 1–6.
- [149] Z. Dai, D. Wu, X. Xu, and Y. Zeng, "Generating ckm using others' data: Cross-ap ckm inference with deep learning," *IEEE Transactions on Vehicular Technology*, 2025.
- [150] Z. Chen, D. Guo, N. Yang, X. Wang, H. Wang, and J. Xie, "Radio map reconstruction based on transformer from sparse measurement," in *2024 IEEE 24th International Conference on Communication Technology (ICCT)*. IEEE, 2024, pp. 917–923.
- [151] E. Krijestorac, H. Sallouha, S. Sarkar, and D. Cabric, "Agile radio map prediction using deep learning," in *ICASSP 2023-2023 IEEE International Conference on Acoustics, Speech and Signal Processing (ICASSP)*. IEEE, 2023, pp. 1–2.
- [152] K. Yang, Y. Chen, and W. Du, "Gwrf: A generalizable wireless radiance field for wireless signal propagation modeling," *arXiv e-prints*, pp. arXiv:2502.2025.
- [153] C. Wen, J. Tong, Y. Hu, Z. Lin, and J. Zhang, "Neural representation for wireless radiation field reconstruction: A 3d gaussian splatting approach," *IEEE Transactions on Wireless Communications*, 2025.
- [154] K. Yang, G. Dong, S. Ji, W. Du, and M. Srivastava, "Gsr: Complex-valued 3d gaussian splatting for efficient radio-frequency data synthesis," *arXiv preprint arXiv:2502.01826*, 2025.
- [155] A. Bayliss, C. I. Goldstein, and E. Turkel, "An iterative method for the helmholtz equation," *Journal of Computational Physics*, vol. 49, no. 3, pp. 443–457, 1983.
- [156] A. Ahmadi, A. Bhattacharya, M. Gratuze, S. G. Cloutier, and R. Al Hadi, "Unet-based deep learning pathloss estimator with boundary condition input," in *2025 IEEE Radio and Wireless Symposium (RWS)*. IEEE, 2025, pp. 9–12.
- [157] K. Suto, S. Bannai, K. Sato, and T. Fujii, "Propagation graph representation learning and its implementation in direct path representation," in *2023 IEEE Wireless Communications and Networking Conference (WCNC)*. IEEE, 2023, pp. 1–6.
- [158] G. Chen, Y. Liu, J. Zhang, T. Zhang, K. Liu, and J. Yang, "Gpr: A gaussian process regression based radio map construction method for rugged terrain," *IEEE Internet of Things Journal*, 2025.
- [159] Y. A. Erlangga, C. Vuik, and C. W. Oosterlee, "On a class of preconditioners for solving the helmholtz equation," *Applied Numerical Mathematics*, vol. 50, no. 3–4, pp. 409–425, 2004.
- [160] J.-W. Shin, Y.-J. Lee, and H.-N. Kim, "Reduced-complexity maximum likelihood direction-of-arrival estimation based on spatial aliasing," *IEEE Transactions on Signal Processing*, vol. 62, no. 24, pp. 6568–6581, 2014.
- [161] W. Chen and J. Chen, "Learning blockage and reflection geometry for mimo beam map construction," in *ICC 2025-IEEE International Conference on Communications*. IEEE, 2025, pp. 2321–2326.
- [162] M. Li, T. Wu, Z. Dong, X. Liu, Y. Lu, S. Zhang, Z. Wu, Y. Zhang, L. Yu, and J. Zhang, "Deeppt: a hybrid framework combining large model architectures and ray tracing principles for 6g digital twin channels," *Electronics*, vol. 14, no. 9, p. 1849, 2025.
- [163] H. Al-Hraishawi, H. Chougrani, S. Kisseleff, E. Lagunas, and S. Chatzinotas, "A survey on nongeostationary satellite systems: The communication perspective," *IEEE Communications Surveys & Tutorials*, vol. 25, no. 1, pp. 101–132, 2022.
- [164] C. Hao, X. Wan, D. Feng, Z. Feng, and X.-G. Xia, "Satellite-based radio spectrum monitoring: Architecture, applications, and challenges," *IEEE Network*, vol. 35, no. 4, pp. 20–27, 2021.
- [165] F. Davarian, "Earth-satellite propagation research," *IEEE Communications Magazine*, vol. 32, no. 4, pp. 74–79, 2002.
- [166] B. Al Homssi, A. Al-Hourani, K. Wang, P. Conder, S. Kandeepan, J. Choi, B. Allen, and B. Moores, "Next generation mega satellite networks for access equality: Opportunities, challenges, and performance," *IEEE Communications Magazine*, vol. 60, no. 4, pp. 18–24, 2022.
- [167] L. Peng, K. Yang, J. Wu, C. Wen, T. Peng, and X. Li, "Machine learning methods comparison for maritime wireless signal strength prediction," *Engineering Applications of Artificial Intelligence*, vol. 158, p. 111357, 2025.
- [168] N. Cheng, F. Lyu, W. Quan, C. Zhou, H. He, W. Shi, and X. Shen, "Space/aerial-assisted computing offloading for iot applications: A learning-based approach," *IEEE Journal on Selected Areas in Communications*, vol. 37, no. 5, pp. 1117–1129, 2019.
- [169] X. Wang, M. Umehira, M. Akimoto, B. Han, and H. Zhou, "Green spectrum sharing framework in b5g era by exploiting crowdsensing," *IEEE Transactions on Green Communications and Networking*, vol. 7, no. 2, pp. 916–927, 2022.